Physical Similitude in Hierarchical Engineered Systems

by

Edward David Blandford

A dissertation submitted in partial satisfaction of the
requirements for the degree of
Doctor of Philosophy

in

Engineering-Nuclear Engineering

in the

Graduate Division
of the
University of California, Berkeley

Committee in charge:

Professor Per F. Peterson, Chair
Professor Ivan Catton
Professor Ralph Greif
Professor William M. Kastenberg

Fall 2010

Physical Similitude in Hierarchical Engineered Systems

Abstract

Physical Similitude in Hierarchical Engineered Systems

by

Edward David Blandford
Doctor of Philosophy in Engineering-Nuclear Engineering

University of California, Berkeley

Professor Per F. Peterson, Chair

Engineers interested in predicting the behavior of complex engineered systems have a strong need to prioritize phenomena by importance due to limitations in simulation and experimentation. The hierarchical nature of reactor systems allows for this organization of complex interactions. By breaking down the system into a series of levels, or stratas, the hierarchical architecture of the system can be established and provide a rational basis for the top-down and bottom-up scaling analyses. From the global response of the reactor using the integral forms of the fundamental transport equations to the atomic interactions such as vacancy creations in reactor materials, the level of acceptability for model fidelity varies enormously and depends strongly on how much of the application domain is encompassed by the validation domain.

In this dissertation, physical similarity criteria are derived at three distinct levels of an advanced reactor: system, subsystem, and component levels. For the purpose of this work, the Advanced High Temperature Reactor (AHTR) is used as a reference reactor. The AHTR is a liquid-salt cooled, high temperature reactor that uses coated-particle high temperature reactor fuel. At the system level, the focus is on developing similarity criteria first at the highest level of the reactor system where the focus is on the dynamic interaction of the components in the system or the global response. Fractional scaling and causative process related scaling methods are introduced where numerical values for each non-dimensional group are determined. At the subsystem level, the concept of a buoyantly-driven shutdown rod system for reactivity control is introduced. The scaling rationale for the shutdown rod system is determined where limitations in subsystem scaling are discussed. Results from a reduced-scale experiment are presented. The shutdown rod performance with respect to system response is also analyzed. At the component level, the efficacy of a fluidic diode concept in high temperature reactors is examined. Similarity criteria and results from a fluidic diode reduced-scale experiment are presented. An empirical approach is used to determine design optimization. The methods developed in this dissertation should be equally applicable to other reactor types and complex engineered systems outside of the nuclear industry.

This thesis is dedicated to my parents who have always taught me through example to do in life what I love. It is also dedicated to my niece and nephew, Eleanor and Edmund, whose youth and exuberance have been a constant reminder of the important things in life.

Contents

List of Figures

List of Tables

Preface

Where is the Life we have lost in living?
Where is the wisdom we have lost in knowledge?
Where is the knowledge we have lost in information?

T.S. Eliot, "The Rock", Faber & Faber 1934.

Following the conclusion of World War II, famed physical scientist and founder of assembly language, Warren Weaver, published a short paper in American Scientist [81] examining the evolving impact science has had on man. Taking a broader perspective, Weaver first examined a range of major scientific breakthroughs that took place during the Industrial Revolution up until the turn of the 20th century. During this period of time, scientists were focused primarily on problems of few variables where close observation and careful generalization resulted in practical solutions demonstrating high societal benefit. The governing mathematical models for these types of problems are deterministic in nature. In other words, the calculated results from these types of models are conditional on the assumption that the numerical values of the input parameters are known and the governing hypothesis of the model is valid [4]. Take for example the development of the turbine where energy is extracted from a moving fluid and converted into useful work. By combining the governing conservation equations, in this case angular momentum and energy, system performance can be quantified by a small set of empirically measureable variables such as fluid enthalpy and flow rate. This first category of problems identified by Weaver, classified as *problems of simplicity*, were the dominant focus of physical scientists prior to the turn of the 20th century.

Weaver then goes on to note that in the late 20th century, famed engineer Josiah Willard Gibbs dramatically changed our fundamental understanding of many scientific disciplines. The development of the powerful techniques of probability theory and of statistical mechanics greatly changed the way scientists dealt with dynamic systems of large populations (e.g. populations of atoms) over an increasingly large range of spatial and temporal scales. The focus on these new types of problems, called *problems of disorganized complexity*, allowed for scientists to manage billions of variables by assuming the governing physical equations hold true across a wide range of temporal and spatial scales. These variables are said to be disorganized because their assumed stochastic nature is what validates the underlying statistical mechanics assumptions. The mathematical models that characterize these types of problems are non-deterministic in nature and range in objectivity. Much science since this period of time has focused on solving problems of this type and has had significant societal impact.

The final class of problems, called *problems of organized complexity*, represents an area of science that has a strong opportunity for growth according to Weaver. These problems are made up of a considerable number of variables but most importantly can be characterized by some level of organization and hierarchy. The mathematical models used to characterize these systems are both deterministic and non-deterministic in nature and require significant engineering judgment. It is precisely this class of problems that are the focus of this dissertation.

The development of advanced nuclear systems is in fact a perfect example of a problem of organized complexity. In his seminal work on scaling methods for nuclear power plants, Zuber [90] laid out the foundation for the development of physical similarity criteria for building scaled experiments representative of prototypical conditions depending on the scale of interest (i.e. system, component, or process).

This concept of 'scale of interest' merits further discussion. Nuclear power plants are systems of organized complexity that can be decomposed into their respective subsystems, components, and processes across a wide range of temporal scales. As Zuber notes [90], the establishment of a hierarchical architecture of the system from the global response down to the local phenomena scale provides the rational foundation for understanding the system by providing levels by which observation can be performed. The importance of these levels of observations cannot be overstated and will be continually revisited throughout this dissertation. These hierarchical levels, or stratas, are truly "windows" into the problem and provide insights for where, in a system, the most valuable empirical observations can be made to validate models for system response.

In Chapter 1, the role of deductive and plausibility reasoning is further examined as they impact the development of advanced nuclear technology. Before we jump into the fundamental mechanical understanding of the reference system studied here, one must briefly dabble in the logical reasoning by which we understand problems. Engineers employ inductive and deductive methods every day to answer challenging questions. While a variety of logical methods are continually used to inform decision-making through physical models, commonly very little attention is paid to the actual impact these methods have on the very nature of explanation. These methods, casually referred to as top-down and bottom-up methods, represent the unique and sometimes anisotropic approaches between understanding the global response of the system all the way to the fundamental process or phenomena that collectively make up the system.

In this chapter, the importance of inductive and deductive reasoning in the development of advanced nuclear technology is discussed in greater detail from the perspectives of logic and probability. For assessing risk in a system, one is interested in the numerical product of results from two unique models answering the questions of how frequently a particular event will occur and what the consequences of the event are if it occurs. The means by which the resultant uncertainties are quantified and safety margins are established share the same overarching logical framework, however oftentimes present unique issues for practical implementation. Since these results can be significant in making informed design changes or modifying operational practice, the focus of the communication of these uncertainties should be on conveying a level of confidence to the decision maker.

It is also shown in this chapter that the factors that drive the uncertainty in a model should be communicated just as effectively as the actual overall result.

The design process for an advanced reactor concept represents the transition from a full set of qualitative functional requirements (“what we want to achieve”) to quantitative design parameters (“how we will achieve it”) that provide a physical basis for analysis or comparison. In Chapter 2, the role of an axiomatic design approach towards advanced reactor technology is discussed. The role of simplicity is analyzed as it pertains to design decisions and the overall facility development process. The initial development of a set of functional requirements for a new technology is done with relatively little *a priori* information and is expected to evolve with learning being performed throughout the system. System functional requirements provide the high level physical basis for demonstrating compliance with safety, environmental protection, physical security, international safeguards, and reliability objectives. While the focus of this dissertation is not on the development of policy, the fact that design objectives have qualitative implications cannot be ignored. As one shifts towards the specification of design parameters, the fundamental characteristics of the design have shifted from high flexibility and illustrative towards detailed and rigid. In this dissertation, practical examples of passive reactivity control and decay heat removal are given as illustrative evidence.

Models used to simulate system performance contain a wide range of uncertainties often characterized differently by each scientific discipline. With respect to advanced nuclear technology, uncertainty is typically thought of as reducible (epistemic) or stochastic (aleatory) and is either associated with the parameters within the model or the ability of the model to capture the problem of interest [19]. The focus of Chapter 3 is on how one deconstucts a complex engineered system where a practical example of a fluoride-salt cooled high temperature reactor is given. The Advanced High Temperature Reactor (AHTR) is a Generation IV reactor concept and provides a useful case study for the remainder of the dissertation. This chapter provides a detailed description of the reactor. The role of top-down and bottom-scaling is also analyzed in detail.

In Chapters 4-6, the role of similarity criteria and phenomenological importance is discussed in detail. Scaled experimental test facilities provide the physical basis for validating computational models that simulate the dominant behavior of the prototypical system under a range of scaled conditions. Testing programs range from investigating fundamental phenomena and processes at the local level (e.g. separate effects tests) to understanding the global integrated response of subsystems, structures, and components that make up the system (e.g. integral effects tests). In this chapter, the role of physical similitude at the global, subsystem, and component levels are explored. The under-appreciated role of the control volume and implications of integral and differential formulations of the transport equations are rigorously reviewed. Historically, much of the thermal-fluid scaling work performed in the nuclear industry has focused on the deconstruction of complex phenomenology for the current generation of water-cooled nuclear reactor technology. As the industry evolves towards innovative nuclear concepts, successful designs will minimize complex phenomenology (i.e. two-phase flow, stored energy, etc.) resulting in a shift, in some cases, towards building experimental facilities focused on system optimization as opposed to understanding underlying processes.

While the traditional engineering fields have undergone significant transformations due to the advancements in science, the fundamental role of an engineer has not deviated from its main objective of improving the overall quality of life. In every engineering discipline, engineers and scientists alike collect tremendous amounts of data through countless measurements or observations. It is at this point that one must distinguish *information* from *knowledge* from *wisdom*. Data that provides some utility or usefulness is classified as information and is obtained through experimentation, computational simulations, application of statistical methods, and the like [27]. Knowledge is then gained by processing and organizing this information and can best be thought of as a deterministic process. The memorization of each definition listed in a dictionary may result in an increase in knowledge however the use of each word in a grammatical or even literary context requires cognitive and analytical ability beyond a descriptive list. Therefore, we must also introduce the concept of wisdom which implies the ability to discern or judge between what is right and what is wrong [27, 3]. In the context of the development of advanced nuclear technology, wisdom can be thought of as making the correct decisions with respect to market-competitive system design and operation resulting in reliable, safe, secure, and clean performance. The important distinction between these three concepts has oftentimes been confused and lost since the first commercial light water reactor was built and operated in 1957. As nuclear technology evolves in the 21st century, it is important that the wisdom gained leads to an improved quality of life [84].

Acknowledgments

Looking back on the past four years at Berkeley has given me an incredible list of people that more than deserve recognition in completing this thesis. I must confess that writing this acknowledgement section was one of the most challenging part of this thesis.

This thesis would not have been possible without the incredible support of Prof. Per Peterson. Ever since I first joined the thermal-hydraulics group early in my graduate career, he has supported me thoughout my thesis with his patience and wisdom. As my teacher and mentor, he has taught me more than I could ever give him credit for here. I would like to particularly thank him for teaching me to pursue what is right and not focus solely on the low hanging fruit. I will very much miss our many long conversations in his office and will look back upon them very fondly. One simply could not ask for a better research advisor.

Prof. Bill Kastenberg is another figure in my life at Berkeley whose influence goes well beyond the material presented in this dissertation. Prof. Kastenberg was very instrumental in challenging me to think about the context by which I perform my research and not just the content. I am very appreciative of his unique insights which help guided me where to best focus my research efforts. I would also like to say a very special thanks to my other committee members, Prof. Ivan Catton and Prof. Ralph Greif. The opportunity to work with Prof. Catton both professionally and during graduate school was truly an invaluable experience and one I hope to continue after Berkeley. I would also like to thank Prof. Greif for being a tremendous teacher and will always remember the various life idioms he enjoyed discussing in class.

Former and current members of the thermal-hydraulics laboratory have given me many fond memories as well as contributions to this thesis. Mike Laufer started up at Berkeley one year after me and has had to put up with my neverending diatribes on what defines meaningful research ever since. Lance Kim started at Berkeley long before I arrived and is someone who I have also enjoyed many interactions. While we have disagreed on many topics, I very much appreciate the valuable insights I have gained through our contentious but always respectful conversations. I would also like to thank Justin Tang and Raymond Wang who were undergraduate researchers that joined shortly after I started in the thermal-hydraulics laboratory. In particular, I would like to thank Justin for all his help in the design and fabrication of my experimental work.

Former colleagues at the Electric Power Research Institute have been instrumental in providing me with the knowledge of practical industry challenges which greatly aided my research. In particular, my former managers David Steininger, Dr. Chris Wood, and Dr. Mohamad Behravesh have been very supportive of my professional growth and encouraging me to pursue a graduate education. Dr. Govinda Srikantiah was an exceptional mentor in the field of thermal-hydraulics and sparked my initial interest in the field. Dr. Edward Fuller and James Benson were both very instrumental in guiding me through the challenges of being succesful in project management.

I could not have finished this dissertation without the support of my family. I wish to thank my mother whose unconditional love and support gave me the strength to complete this work and pursue my vision. Her warmth and incredible spirit never cease to amaze me. I would like to thank my brother and his family, whose love are with me in whatever I pursue. Finally, and certainly not least, I would like to thank my father for his remarkable wisdom, patience, and generous love. Deepening our friendship has been a very special part of this journey. There is no better role model a son and scientist could ask for.

Chapter 1

Logical Reasoning in Development of Advanced Nuclear Technology

1.1 Introduction

Mathematical knowledge gained by engineers is validated through *demonstrative* reasoning while the ability to infer evidence is supported through *plausible* reasoning. This distinction by Polya [60] is vitally important as scientists and engineers dissect the complexity of hierarchical systems of varying intricacy. For example, the derivation of the well known Navier-Stokes equations (NSE) is well grounded in demonstrative reasoning where Newtonian mechanics provides the physical basis and vector calculus provides the mathematical description. However, the complex fluid-structure-interaction in a nuclear power plant between a piping structure and a two-phase coolant flow requires plausible reasoning. While the resultant impact from the mechanical interaction is easy to measure, the fundamental logic used to physically descibe the phenomenology requires inference.

This dissertation focuses on engineered systems, in particular advanced nuclear reactor technology, and their transient response to various initiating events that require a comprehensive understanding of dominant phenomenology across wide ranging temporal and spatial scales. The fact that reactor concepts can be classified as a system of organized complexity means that both demonstrative and plausible reasoning are essential to fully understand the system. The focus of this chapter is on defining both reasoning processes within the context of understanding advanced reactor technology and ultimately from the perspective of experimental validation.

There is a strong need to prioritize phenomena by importance due to limitations in simulation and experimentation. The hierarchical nature of reactor systems allows for this organization of complex interactions. Similarity arguments developed by scaling the governing conservation equations are essential in the reactor safety community due to current limitations in simulation capability. Best-estimate system codes are volume-averaged and must use empirical closure relationships to capture key local phenomenology. By contrast, computational fluid dynamics codes are capable of simulating local effects and component response but system simulation is not reasonable due primarily to algorithmic limitations and simulation cost. This is precisely why one starts with the integral, volume-averaged form of the governing transport equations for designing integral effects tests and the differential form for performing separate effects testing where volume averaging is insufficient. It is important to note that when we apply NSE we are dealing with Newtonian fluids where specific properties of the working fluid can be expressed by a small number of thermophysical properties (i.e. viscosity). Therefore according to Goldenfeld et al. [52], the macroscopic phenomenological description of the working fluid can be characterized by two parts: the universal structure and the phenomenological parameters sensitive to the specific microscopic physics of the system. In the nuclear reactor community, Wulff and Rohatgi [87] classify this universal structure of the model by extrinsic closure relations while the microscale physics can be classified by intrinsic closure relations. Any useful phenomenological system description will possess this structure.

Some phenomena in nuclear reactors, however, evolve over very long periods of time where oftentimes heavy empiricism is warranted. For slowly evolving phenomena, typically one is interested in time averages of system-specific variables such as temperature, neutron flux or fluence, local chemistry, and mechanical loading conditions that can impact material behavior. Unlike the phenomena discussed above, here the main concerns are considerably larger temporal and spatial ranges where identifying dominant microscopic parameters physics of the system for experimental validation is much more complex. The spatial range for this class of phenomenology can span 15 orders of magnitude from the length scales associated with atomic nuclei all the way to the length scales associated with reactor component response. In a similar fashion, relevant temporal scales can span more than 24 orders of magnitude ranging from femtoseconds to decades requiring a multi-scale approach [11]. When evaluating the long-term performance of materials for reactor design, a primary concern is with material degradation at the micron length scales and above (i.e. cracking, swelling, etc.) that can compromise structural integrity. However at the smallest relevant spatial scale, it is radiation induced damage creating primary defects that lead to microstructural change that can ultimately drive these degradations.

For both classes of phenomenology (i.e. slowly or quickly evolving), physical models are established that are valid given the problem definition and a set of assumptions. From there, mathematical models[1] are established that represent as much of the physical model as possible, using constitutive relations where necessary. The model development process is illustrated below in Fig. 1.1.

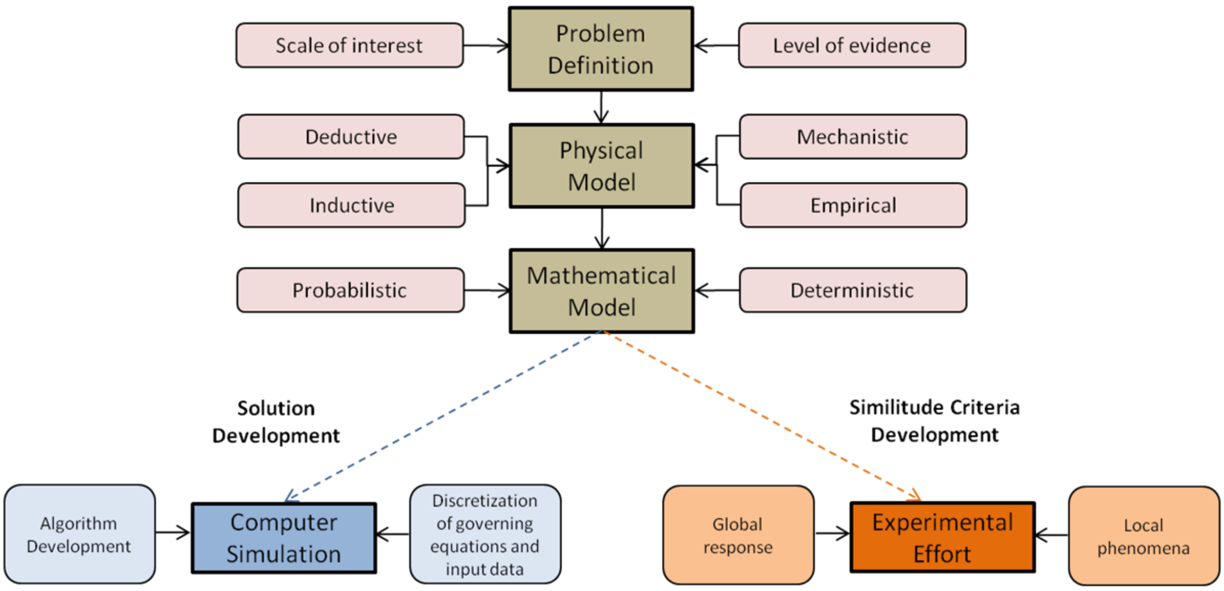

Figure 1.1: Model development process and role of similitude analysis

Take for example the foundations of classical boundary layer theory for aerodynamic

[1]Oftentimes referred to as "model of the world" [4].

flow developed by Prandtl [64] that are predicated on a set of physical arguments dividing the flow over a body into two regions, viscid and inviscid. Dimensional arguments, such as the fact that one can assume the ratio of the length scale associated with the thickness of the boundary layer is negligible with respect to the characteristic length of the body, allows for one to write Prandtl's differential form of momentum laminar boundary layer equations (1.1).

$$\rho u \partial_x u + \rho v \partial_y u = -\partial_x P + \partial_y \left(\mu \partial_y u\right) \tag{1.1}$$

For laminar boundary layers, the reduction of the x-momentum equation from an elliptic partial differential equation (PDE) to a parabolic PDE through the elimination of a second-order term greatly simplifies the solution process. Detailed phenomenology within the boundary layer can be analyzed but the assumptions break down as one approaches the inviscid region.

However, in many engineering applications the details of the flow variables within the boundary layer are of second or third order importance as we may just need to know the displacement thickness and shear stress on the wall in order to assess drag. The transformational work of Von Karman led to the integral formulation[2] of the boundary layer equation (1.2). Starting with the integral approach allows for substantial flexibility in studying higher Reynolds number regimes as detailed information is not required and does not rely on similarity methods and boundary layer shape [45]. Therefore the momentum balance can be recast in its integral formulation (1.2) and the ratio of shear stress and dynamic pressure (1.3),

$$\partial_t \int_0^\infty \rho \left(U - u\right) dz + \partial_x \int_0^\infty \rho \left(Uu - u^2\right) dz + \partial_x U \int_0^\infty \left(U - u\right) dz = \mu \partial_z u|_0 \tag{1.2}$$

$$\frac{\tau_w}{\rho u^2} = \partial_x \theta + \frac{\left(\delta^* + 2\theta\right)}{u} \partial_x u \tag{1.3}$$

The construction of the integral or differential formulations of the governing transport equations requires a definition of a control volume by which processes flow or are stored. The control volume selected in 1.2 extends the entire length of the boundary layer whereas the differential formulation starts with an infinitesimal control volume that is integrated across this length. When understanding reactor thermal-fluids problems, the construction of the control volume, in addition to establishing boundary and initial conditions, are the key moments by which the physical model and mathematical model are bridged (more is discussed in Chapter 3). One of the goals of this dissertation is to better understand these implications with respect to experimental validation but also the resultant impact during the reactor design process.

[2] It is often stated that one can work from the differential form to the integral form using fundamental vector calculus, which is indeed correct. However, the complex nature of similarity criteria and solution development makes this process practically intractable. This will be discussed later in the dissertation.

1.2 Reactor Safety and Risk

1.2.1 Background

Safety issues associated with nuclear technology first arose during the Manhattan Project during the establishment of the U.S. nuclear weapons program. In 1942, DuPont agreed to be the prime contractor responsible for construction of the plutonium production complex starting initially at Oak Ridge and ultimately being completed at the Hanford site. Nuclear technology spanning the fuel cycle from enrichment all the way to chemical separation was just entering its infancy stage at a remarkable pace with large material inventory demands and little margin for error.

In fact, it was DuPont chemical engineers working on the B-Reactor at Hanford who first formally introduced system hierarchy and the concept of 'defense-in-depth' into reactor design and construction [46]. The B-Reactor was the first large scale reactor built following the successful demonstration of the technology at Oak Ridge with the X-10 pilot reactor. Due to the high unfamiliarity of the technology, the DuPont engineers relied upon their fundamental understanding of industrial chemical plants and implemented several layers of independent 'barriers' between the site workers and the radioactive source term. Additionally, the concept of redundancy and diversity in engineered safety systems were first formalized into the reactor design process. The concept of design margin played a fundamentally important role, when upon start up of the B-reactor it was discovered that the accumulation of the xenon fission product caused the reactor to go subcritical. However, the engineers had provided redundant channels for fuel, so minor modifications to add more fuel channels then allowed the reactor to operate continuously at high power.

This mindset towards nuclear safety was pervasive in the commercial nuclear industry and the accompanying regulatory body that emerged after Congress passed the Atomic Energy Act of 1954. The regulatory authority, then known as the Atomic Energy Commission, was chartered with enforcing nuclear regulation which was accomplished through highly deterministic safety assessments and the use of large safety margins. However the AEC under the direction of Milton Shaw had demonstrated a lapse in judgement regarding emergency core cooling system (ECCS) integrity issues. These issues in addition to other technical conflicts put into question the AEC's ability to fairly regulate. Reduced-scale integral effects tests such as Semiscale at the Idaho National Reactor Testing Station demonstrated that emergency core cooling system (ECCS) core bypass flow was the dominant phenomenology of interest which came as a surprise to researchers[3]. These findings brought into question whether Westinghouse PWR's could provide adequate cooling during a loss of coolant accident (LOCA) in order to maintain core integrity and acceptable fuel temperature. In the mid 1970's due to political pressure, the Energy Reorganization

[3] This is one of many historical examples where performing validation experiments have identified new phenomenology providing important insights.

Act of 1974 split the AEC into the U.S. Nuclear Regulatory Commission (NRC) and a research division which ultimately was reorganized into the Department of Energy.

It was not until the late sixties prior to abolishment of the AEC that risks posed by commercial nuclear plants were evaluated using probabilistic means, led by seminal work by Farmer [31] and Starr [72] . This shift in reactor safety quantification mindset allowed engineers to look at problems that had been previously enveloped by conservatively large margins (more on the word 'conservative' is discussed later). Farmer's work showed that by relating fission product release to frequency of release, one could in fact quantitatively assess the relative risk each isotope presents to a commercial nuclear plant during its operation. Farmer was also credited with the 'Farmer curve' (see Figure 1.2) graphically illustrating the risk as a function of frequency versus consequence (also known as frequency-consequence curve). Starr was really the first to make the comparative analyses of the risks and hazards of nuclear technology which provided insights into societal risk perception. The Probabilistic Risk Analysis (PRA) field started to expand in the nuclear industry during this time however the role of the community has been hotly debated both formally and informally ever since. In 1975, a study led by Norm Rasmussen (published as WASH-1400) prompted controversy over the applicability of PRA in reactor safety. See Keller and Modarres [46] for a more comprehensive review of the history and maturation of the field of PRA.

The key differences between slowly and quickly developing phenomenology were discussed in the previous section from a physical model standpoint however the implications, or relevance, of these processes are evaluated through considering risk information. In analyzing risk we are attempting to envision how the future will turn out if we undertake a certain course of action (or inaction). These preferences are what drive risk management in the nuclear industry and can ultimately drive innovation in the reactor design process. Risk was first classically defined in the nuclear industry by Kaplan and Garrick [44] and has evolved many times since [68],[20], and [42]. In their revised classical definition of quantitative risk, Kaplan [43] explains that risk can be thought as three questions: What can happen? How likely is that to happen? If it does happen, what are the consequences? The answer to the first question is called a scenario, and the i-th scenario is denoted by S_i. ϕ_i then denotes the likelihood and X_i the consequences of the i-th scenario (p stands for probability of frequency and is discussed more later).

$$R = \left\{ \left\langle S_i, p_i\left(\phi_i\right), p_i\left(X_i\right) \right\rangle \right\}_c = 1, 2, ..., N+1 \tag{1.4}$$

Perhaps this expression for risk (1.4) is better thought of as an answer to the above set of three questions. Kaplan [43] goes on to note that this definition of risk "... is not a number, nor is it a curve, nor a vector, etc. None of these mathematical concepts is 'big' enough in general to capture the idea of risk. But the set of triplets, we find, is always big enough, and if we start out with that, it always gets us on the right track." Graphically, risk is most commonly depicted on frequency-consequence curves where the vertical axis represents an event sequence mean frequency and the horizontal axis represents the dose at exclusion area boundary (see Figure 1.2). In simpler terms, the vertical axis represents the overall likelihood of an event occurring while the horizontal axis is a measure of the consequence, in this case radiological dose, of that particular event.

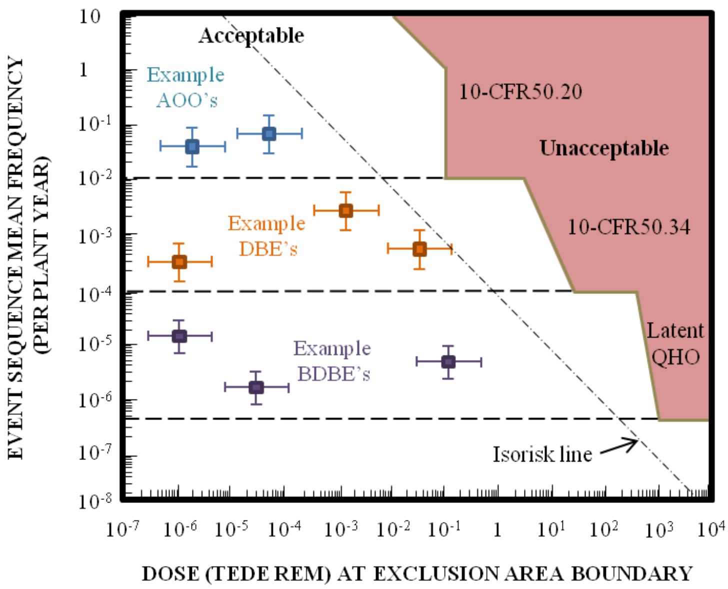

Figure 1.2: Example frequency versus consequence curve depicting anticipated operational occurences (AOO's), design basis events (DBE's), and beyond design basis events (BDBE's) where federal regulation establishes acceptable region.

In fact, one can think of the quickly evolving phenomenology discussed earlier being prominent when quantifying the consequence space whiles the slowly evolving phenomenology dominates the frequency space. Traditional probabilistic risk analysis is based upon logic structures (i.e. event trees and fault trees) grounded in Boolean logic. The purpose of PRA depends strongly on the stage it is being implemented [5] as the quality of data can drive the process. We will discuss in more detail the role of statistical inference in answering the question of likelihood later in this chapter however it is important that we briefly discuss the role of uncertainty. In Figure 1.2, each event has bands depicting the range of uncertainty in both dimensions. In practice, these bands are actually distributions characterized by experience and heurism where bias is included due to the use of conservative assumptions in some parts of the analysis. Oftentimes in the nuclear industry, we characterize uncertainties by type: parameter, model, and completeness [57],[16]. Perhaps the biggest uncertainty associated with new reactor technology is the identification of a complete and conservative licensing basis envelope (the c in Eq. 1.4 represents a 'complete' set).

It is important to note that the word ‘conservative’ is often used incorrectly in reactor safety and can lead to confusion. The Three Mile Island plant was licensed under the seemingly “conservative” Appendix K safety criteria. However, it was the implicit assumption that the design basis was conservative that was driven chiefly by a maximum credible accident (MCA) mindset that originated with the AEC and continued with the US NRC. What had started as a physicists approach to reactor safety had the unintended consequence of the regulatory body ratcheting down rulemaking against an extreme event due to a wide range of reasons. This is exactly what has happened with the implementation of a Design Basis Threat (DBT) approach towards reactor physical protection following the terrorist attacks on September 11, 2001. When a facility can demonstrate it can withstand the DBT, it is considered adequately “secure.” This approach is highly prescriptive and compliance criteria are tightly coupled with the specific threat details of the DBT (i.e. number of assailants, capabilities, etc.). There are concerns in the reactor security community that DBT approach driven by maximum credible incidents just drives up costs requiring more gates, guards, and guns. This misallocation of resources shifts the concern away from more likely scenarios that can potentially compromise reactor security (i.e. insider threat).

1.3 Deductive and Plausible Reasoning

The connection between top-down and bottom-up scaling of reactor systems as products of inductive and deductive logic respectively was first formally made by Zuber [90]. A common question that typically arises is why does one care about this connection between engineering and philosophy of science? The short answer to this question is that for many types of problems the implications are indeed second order. Intuitively, people decouple complexity from their regular everyday decisions from driving to work or buying merchandise at the lowest cost where holisms such as environmental or globalization implications are not factored in. Engineers often design systems that are not realizable in commercial or practical settings with hopes that the environment will ultimately change or because it just is not a primary motivator. This section gives a more thorough answer to this question with respect to advanced reactor development through exploration of the schools of inductive (i.e Jaynesian) and deductive (i.e. Popperian) thinking. It is argued that both methods are integral to the development, construction[4], and operation of advanced reactor technology. The focus is not on the ongoing discussion surrounding the virtues of Bayesian and Fisherian/frequentist methods but rather the fundamental differ-

[4]It is interesting to note that cost estimates for new nuclear technology are done using two methods: top-down methods (inductive) and conventional bottom-up methods (deductive). In the top-down method, detailed cost information about existing reactors are used and scaling arguments are performed to assess costs for new designs. Also known as conventional cost-engineering, the bottom-up approach utilizes detailed engineering information including all construction commodities, plant equipment, and labor hours [78].

ences between the governing logic and role of evidence during the experimental validation process of new reactor technology.

The logic structures that make up PRA are based fundamentally on inductive or deductive logic. Before the logical implications associated with PRA are discussed, one must first briefly dabble in logical reasoning. Here it is better to refer to Jaynes [39] who reproduced Aristotle's deductive logic (*apodeixis*) in two useful syllogisms,

$$\begin{array}{c} if\ A\, is\, true,\ then\ B\, is\, true \\ A\, is\, true \\ \hline therefore\ B\, is\, true \end{array} \tag{1.5}$$

and it's inverse,

$$\begin{array}{c} if\ A\, is\, true,\ then\ B\, is\, true \\ A\, is\, false \\ \hline therefore\ A\, is\, false \end{array} \tag{1.6}$$

Deductive logic is precisely the type of reasoning we would like to use for all technical challenges with new nuclear technology but unfortunately oftentimes we don't have the preqrequisite information or evidence to allow for this approach. In these instances, it is necessary to fall back on a weaker syllogism (*epagoge*),

$$\begin{array}{c} if\ A\, is\, true,\ then\ B\, is\, true \\ B\, is\, true \\ \hline therefore,\ A\, becomes\, more\, plausible \end{array} \tag{1.7}$$

In the final section of this chapter, the role of inductive and deductive reasoning discussed in greater detail with respect to risk quantification. While risk management is not the focus of this chapter, the interpretation of risk-information by regulators, investors and plant management is of great importance where decisionmaking evaluates the tradeoffs between various sources of risk.

1.4 Concerns Surrounding Risk Quantification

PRA is based upon logic structures, that identify the different combinations of more elementary events, called basic or initiating events, that could lead to undesired system end states [57]. In order for PRA to be successful in impacting new design, reactor designers will need to incorporate risk information impacting safety, security, and reliability early in the process. There are countless examples of costly plant retrofits being required that were easily avoidable if this type of information had been considered earlier. It has become increasingly clearer that the traditional model of assessing structural engineering considerations in addition to other disciplines (i.e. physical security, intrumentation and controls, etc...) at the tail end of the design has had a negative impact on reactor builds. Risk-informed optimization of safety and security is necessary during conceptual design and there is a steadily increasing loss of opportunity to install intrinsically safe, reliable, and secure features as the design matures and construction proceeds [56].

1.4.1 Challenges with Scenario Incompleteness

In revisiting the risk triple defined in Eq 1.4, each of three elements are evaluated formally or informally using either of these logical approaches. First, the identification of the event, S_i, was identified using both fault tree analysis (i.e. inductive) where the analysis started with a single fault event as well as event tree analysis (i.e. deductive) where the analysis starts with an intitiating event and 'propagates' this event through the system[5] [12]. The identification of a complete licensing basis envelope for advanced reactors is one of the most challenging issues surrounding the licensing of new reactor technology.

The principal of Defense in Depth (DiD) is applied in safety design to account for the uncertainty in whether all possible initiating events within the licensing basis have been identified, and whether the probability and consequences of the initiating events have been accurately assessed, given the problem of incomplete knowledge [58]. A number of methods are available to provide and assess DiD, including measures to reduce the frequency of initiating events, measures to provide diversity in preventing unacceptable outcomes from event sequences (assuring that all fault tree cut sets have multiple members), and measures to assess plant response to hypothetical severe plant conditions and provide mitigation measures. A “rationalist” approach to DiD (as opposed to a “structuralist” approach) uses PRA methods to quantify and reduce system uncertainties as opposed to relying on potentially overly conservative safety margins [38]. In practice, a hybrid rationalist/structuralist risk-informed approach is warranted [38] and has been advocated by the US NRC [16].

1.4.2 Challenges with Scenario Likelihood Determination

The second element of risk, $p_i\left(\phi_i\right)$, refers to the likelihood of this identified event where the PRA community is faced with the same traditional issues surrounding the use of Bayesian (i.e inductive) and traditional frequentist (i.e. deductive) methods any community employing statistics faces. The debates between objective and subjective probabilities have been contested in a wide range of publications; a good overview of

[5]It is important to note that both event and fault trees are visual representations of a series of events where Boolean logic is employed. Therefore, it is best to think of the approaches for either method as inductive or deductive whereas symbolic logic is used for combining events.

the fundamental disagreements can be found in Efron [24] (in addition to the followup comments in the paper) as well as Kaplan [43]. With respect to nuclear technology, PRA analysts are forced to embrace Bayesian methods as the required scientific foundations may be unestablished and fundamental data unavailable. However, it has been argued that in the case of sparse data both methods will yield numerically similar solutions as where Bayesian interval estimates and frequentist confidence intervals are close to equal [6]. Ultimately it is confidence in these estimates that drives decision making during the development process of advanced nuclear technology. For example, plant engineers use mechanistic and empirical models to predict system response where uncertainties are quantified and safety margins are utilized to account for incomplete information. Private equity investors or utility risk managers also use mechanistic and empirical models where financial risk is assessed and contingencies are put in place for dealing with ‘unknown unknowns’. In both cases, the ability of the individual to infer knowledge hinges strongly on the knowledge utilized and the amount and characteristics of the supporting data.

In addition to the debate on the objective nature of probabilities, the characteristics that differentiate safety-related events versus security threats are worth discussing. Initiating events for safety-related events can be regarded as resulting from random processes and are best treated using probabilistic means. Security initiating events, however, are not random and are the product of strategic actions, learning processes and decisions of adversaries and the defender. Oftentimes, using traditional consequence metrics such as radiological or financial damage may not be useful therefore consequence can be better thought of as 'perceived value'. The attacker and the defender may have different perceived values which can be important in affecting adversary decision making. Assessing the likelihood of adversarial attack must therefore account for the various measures that force the adversary to allocate its resources in the most optimal fashion. DBT does not consider the impact of measures that force the adversary to allocate its resources non-optimally, in particular, the impact of measures that would limit the adversary’s access to information needed to optimize its selection of its attack strategy [63]. The adversary’s payoff for attacking a target can be expressed as the product $C \times AV \times PAS$ (where C, AV, and PAS refer to consequence, adversary valuation factor, and probability of adversary success). The adversary valuation factor takes into account the fact that the adversary might value a consequence differently than the defender (e.g., a certain target might have symbolic value), and it takes into account the fact that the adversary and defender may have different levels of risk tolerance. Figure 1.3 shows how adversary resources AR can be plotted as a function of the adversary payoff. In general, it is expected that adversaries will search for targets and attack strategies that fall to the right of the indifference curve.

1.4.3 Challenges with Scenario Consequence Determination

The third component of risk, $p_i(X_i)$, refers to the likelihood of the consequence of event, S_i. Determining the physical consequence of initiating events is the focus of this

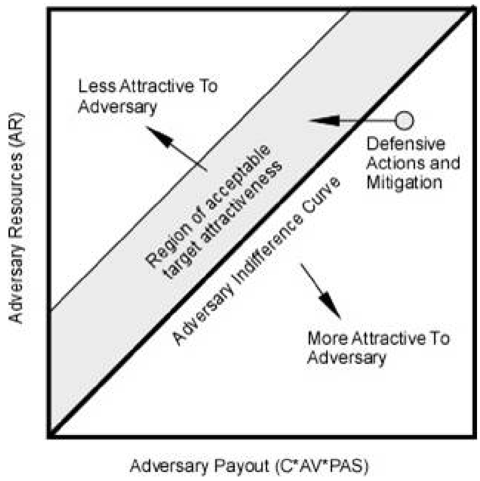

Figure 1.3: Adversary resources versus adversary payout plotted on a linear scale, showing an adversary indifference curve [63].

dissertation where confidence is established through the form of simulation that has undergone rigorous experimental validation. As noted by Kaplan [43] consequences could be defined as a vector or multicomponent quantity, that it could have spatial or temporal dependency, that it could have a range of uncertainty, and if so, this uncertainty in the consequence spaced should be quantified through the use of probability curves.

There is a strong preference in the scientific community towards utilizing the hypothesis-driven scientific method to establish confidence which follows the Popperian pattern quite well. Essentially, new physical and mathematical models are developed or capabilities are increased and these models are taken as far as they can perform. On the simlation side, there is a strong industry movement towards encompassing more physics across a wider temporal range. While it is true that higher fidelity modeling, if correctly verified and validated, can improve accuracy in numerical results, it is the ability of the simulation code to predict outside the validation domain (see next chapter for further discussion) that is of equal, if not greater concern. Therefore it is here that Popper's criterion of falsifiability [62] must be further analyzed.

It is the author's opinion that the current nuclear engineer understands this criterion quite well based on traditional engineering methods where models are compared with evidence and accuracy is assessed. This is done through extensive computational simulation and experimentation where there is an increasing inclination towards the former. When the model breaks down, the engineer ultimately tinkers with the model using available parts and revisits the problem. Sometimes the model requires a radical design but ultimately the engineer will discard the model once they demonstrate it has been falsified. In the author's opinion, one of the key issues surrounding current reactor simulation is the lack of focus on determining a model's falsifiability across the entire design basis spectrum. In the context of Gen IV technology with limited experimental and operational experience, the focus should be shared between assessing falsifiability in the numerical results (i.e. where in the transient is peak clad temperature not matching experimental data?) and assessing the falsifiability of the code's extrapolation ability (i.e. can the code demonstrate phenomenology across a range of transients and where does it break down?). Oftentimes, the modeler of new reactor technology is not interested in what is considered acceptable but rather producing results that look reasonable. In other words, reactor designers should always try to demonstrate falsifiability in the safety of the reactor across a design basis as opposed to just demonstrating particular figure of merit metrics have been met.

However, such deductive methods towards hypothesis development cannot always be employed and reactor designers must rely on inductive logic. When considering both methods, the ability to confidently demonstrate a predictive capability is an imperative. There are many situations with high-consequence systems such as nuclear reactors where the analyst must deal with problems where limited to no experience exists. When relying upon inductive methods such as Bayesian methods, experience in the form of prior distributions must be interpreted as part of a hypothesized model that is posited as potentially useful until possibly modified or abandoned. Therefore a governing philosophy of deductive and inductive reasoning where falsifiability is the main driver must be utilized in demonstrating scenario consequences across the design basis. Therefore one does not need to be concerned with having "perfect" information where prior distributions must match subjective kowledge. Rather assumptions are stated clearly upfront and the focus is on falsifying the model through performing posterior predictive checks and validating the model [34]. The role of model validation is the focus of the next chapter.

Chapter 2

Experimental Validation in Reactor Design

2.1 Validation Focus

A physical understanding of the dominant phenomenology in a nuclear plant is a fundamentally imprecise and inexact thing, but an absolute imperative for a reactor designer to have. The ultimate test of all knowledge comes through experiments. As noted by Kline [47], the scientific method is based directly on the idea that nature and not man is the ultimate arbiter where experiment is the sole judge of scientific "truth”. Scaled experimental test facilities provide this physical basis in the reactor community for validating computational models that simulate the dominant behavior of reactor systems under a range of prototypical conditions. High-performance computing is evolving more rapidly than ever with the petaflop speed barrier (performing 10^{15} floating point operations per second) being recently breached at Los Alamos. Scientists and engineers are well poised to make significant advancements in multi-physics and multi-scale computational modeling with some even claiming the scientific method as we know it is becoming “obsolete”[1]! In this section, the future of reduced-scaled experiments and methods for reducing complexity in reactor design are discussed.

Before the rationale for similarity criteria is developed, it is important that the dominant phenomenology in this dissertation is initially classified. Predicting how a reactor performs during normal and off-normal operational modes is very much a multi-physics and multi-scale problem. Each individual ‘physics’ (i.e. neutronics, convective heat transfer, etc...) has its own physical length and time scales, however these scales can change significantly during the course of a transient. As a quick example of a reason to be cautious, take the multi-physics computer simulation of an instantaneous control rod ejection transient from Pope and Mousseau [61]. This transient results in a large power excursion reproduced in Figure 2.1. As expected, earlier in the transient the shortest time scales are associated with the neutronics physics (green) as the reactivity in the core immediately increases. However as the reactivity slows down due to Doppler feedback, the large amount of energy that was dumped into the fuel now conducts through fuel and cladding surface making conduction (red) the physics with the fastest time scales. As the heat hits the surface of the cladding, the coolant in the core starts to boil thus making two-phase convective heat transfer (blue) the physics with quickest time scales. Oftentimes, code developers will decouple these physics using operator splitting methods on the basis of time scale or characteristic frequency arguments[2] (i.e. neutronics is fast and conduction is slow) however great care must be given to identifying when and where these scales change throughout the course of a transient.

[1] This comment was made by the editor in chief, Chris Anderson, of Wired Magazine in an article titled, “The End of Theory: The Data Deluge Makes the Scientific Method Obsolete”.

[2] A good discussion on identifying decoupling boundaries in complex transport systems can be found in Gamble [33]. While such reductionistic methods are very useful in taking a complex problem and breaking them up into subsets, one must be careful in ensuring the underlying assumptions are valid throughout the entire problem.

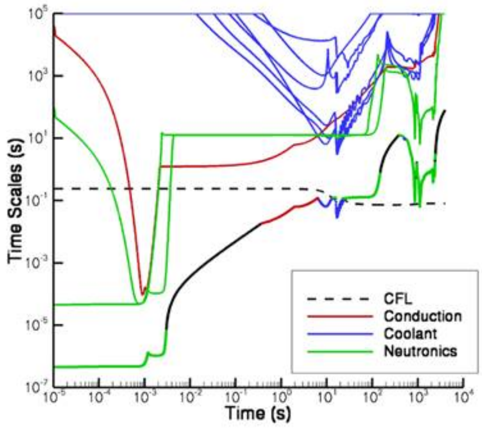

Figure 2.1: Dynamical timescales of state variables following an instantaneous rod ejection event [61]

This dissertation focuses primarily on phenomena, or physical processes, in advanced reactors that can be captured using the governing mass, energy, and momentum conservation equations, the thermal and caloric equations of state, and a host of constitutive relations where necessary. In other words, the focus is on thermal-fluid problems while clearly defining the governing assumptions about additional relevant physics. As discussed in the first chapter, this phenomenology can be characterized as rapidly evolving (i.e. seconds, minutes) as opposed to slowly developing phenomenology (i.e. months, years) that impact plant reliability. This distinction is important because the former class of phenomenology lends itself well to reduced-scale experimental validation as compared to the latter class which requires long-term prototypical testing or accelerated aging.

2.2 Role of Experimental Testing Programs in Reactor Development

2.2.1 Background

Testing programs range from investigating fundamental phenomena and processes at the local level (e.g. separate effects tests, SET's) to understanding the global integrated response of subsystems, structures, and components that make up the reactor system (e.g. integral effects tests, IET's). The Hierarchichal Two-Tiered Scaling (H2TS) methodology was initially developed by Zuber [90] and most recently been implemented successfully for design certification of Westinghouse's AP-1000 where passive decay heat removal plays a significant role [41]. Ultimately, this work focuses on the scaling rationale in building properly scaled experimental facilities to validate best-estimate computer simulation.

The Code, Scaling, Applicability and Uncertainty (CSAU) methodology [25] developed in the late 1980s has been the industry standard for validating transient analysis codes for use in the licensing process for design certification, but has only been applied in its entirety to advanced light water reactors (ALWR). A critical element of the CSAU approach to the modeler and experimenter alike is the development of Phenomena Identification and Ranking Tables (PIRTs). The PIRT process was developed to identify the dominant phenomena governing a specific system and transient and ensure both the code and experimental program capture the important physical processes in that transient. Commonly the ranking process relies heavily on expert elicitation where the effectiveness of the PIRT is a strong function of the quality of analysts involved and overall experience base in the qualification domain (i.e. experimental and operational data). The role of PIRT during the reactor licensing process has been discussed in a wide variety of publications [25, 82, 48].

A quick review of the advanced reactor technologies considered by the Gen IV International Forum [17] shows 6 reactor types utilizing a variety of working fluids operating under a range of prototypical conditions each achieving a different performance with respect to the Forum's goals. Each of these technologies has evolved greatly since their original inception. Previous operational experience (mostly at the test reactor scale), which was already very limited, may no longer be applicable. One critical issue affecting the Gen IV designer interested in obtaining US NRC design certification is the determination of a level of acceptability for the desired evaluation model in an uncertain regulatory climate. The majority of reactors licensed by the USNRC are light water reactors where the safety codes used by the regulator have undergone extensive verification and validation (estimates have put the total cost of all LWR confirmatory testing programs between 1-2 billion inflation adjusted dollars [36]). While there exist important verification issues surrounding Gen IV best-estimate code development, the focus of this dissertation is on the validation process and the role of scaled experiments for the Advanced High Temperature Reactor (AHTR) which is the reference reactor for this work (more on the details of the AHTR can be found in the following chapter).

2.2.2 Validation Domain for Advanced Reactors

With computing costs dropping rapidly, high-fidelity computer simulation and modeling is expected to play a much more dominant role in the future. Not only is the accuracy of these codes important but it is their predictive accuracy that is essential in designing and licensing next generation nuclear technology. As defined by Oberkampf and Trucano (2008), a validation experiment is conducted for the sole purpose of determining the "predictive accuracy of a computational model or group of models". In other words, a validation experiment is designed, performed, and analyzed for the purpose of quantitatively determining the ability of a mathematical model within a computer code to simulate a well-characterized physical model[3] (see Figure 1.1).

The distinction between *exploratory* and *confirmatory* validation experiments with safety-related implications is an important one and requires a quick clarification. Exploratory research is exactly what it implies and is the focus of validating interesting *a posteriori* hypotheses or design concepts of potential value. From an experimental perspective, this translates to executing experiments that demonstrate 'proof-of-principle' under reasonable quality standards where necessary uncertainty reduction is expected to occur with further investigation. Confirmatory research focuses solely on confirming *a priori* hypotheses or design concepts. Confirmatory experimental work is performed after sufficient exploratory research has been performed and must be executed under the most stringent nuclear quality assurance (NQA) standards typically requiring significant resources. Due to infancy of the AHTR design, the work discussed throughout this chapter is of the exploratory nature and should be treated as such.

According to Oberkampf and Trucano [55], an effective code validation program incorporates the following three elements: (1) quantification of the accuracy of the computational model by experimental comparison, (2) interpolation or extrapolation of the computational model to prototypical conditions, and (3) determination if the estimated accuracy of the computational model, for the conditions of the intended use, satisfies the accuracy requirements specified. The second element can pose significant challenges to advanced reactor designers where desired prototypical conditions can be costly to achieve and can effectively limit the validation domain (see Figure 2.2). The other two elements can pose unique challenges for new technology development, however this work focuses on the role of physical similarity in reduced-scale experimental test design that is central to correct modeling.

[3]Oberkampf and Trucano go on to note that that the code or the computational scientist can now be thought of as the "customer". This mindset represents a significant departure from the LWR validation process of the 60's and 70's where computational cost was high and the experiment or experimentalist was thought of as the "customer".

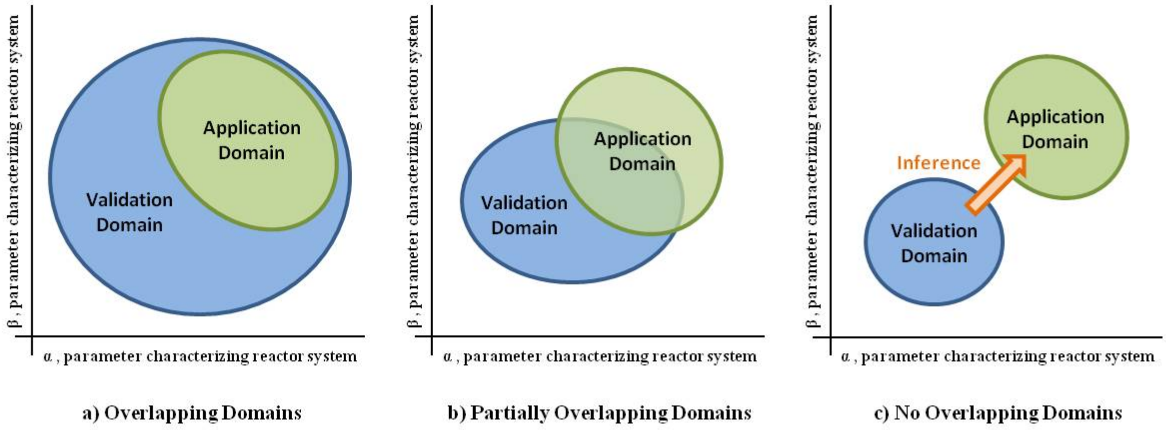

Figure 2.2: Potential relationships of the validation domain and the application domain.

Ideally, one would like for the application domain to be encompassed entirely by the validation domain (Fig. 2.2a) which is the prevailing case in most engineering applications. In some engineering applications, there is absolutely no overlap between the validation and application domains (Fig. 2.2c) and inference is required. Many high-consequence engineered systems such as nuclear weapons testing and scientific exploratory research (i.e. astrophysical observations, high-energy physics, etc. . .) fall into this category and can only be made using a combination of physics-based models and statistical methods [23, 79]. Advanced reactor concepts such as the AHTR with limited or no relevant operational experience fall in between where there exists a partial overlap between the validation and application domain (Fig. 2.2b).

To overcome this limitation, validation benchmarks in the AHTR must be used in order to ensure the accuracy and reliability of the code. A validation benchmark is defined as a selection of information that is believed to be accurate or true for use in experimental validation or calibration, one or more methods of comparing this information with computational results, and logical procedures for reaching conclusions from these comparisons [75]. As discussed previously in Chapter 1 regarding the role of future simulation and experimentation, the reactor safety case must be demonstrated across a wide spectrum of design basis events of various likelihoods making up the licensing basis envelope. It is simply impossible to perform an experiment for each of these events due to cost limitations. Therefore, the role of validation benchmarks for licensing advanced reactor such as the AHTR is in fact open to much interpretation and has non-trivial implications. Oberkampf [55] talks of strong sensed benchmarks (SSB) that can be viewed as engineering standards where the purpose of the benchmark experiment is clearly defined and acceptance criteria for comparison with the benchmark are established. The AHTR experimental validation program will need to incorporate such types of benchmarks in order to improve code predictive accuracy and minimize required calibration. Some examples of the types of required validation benchmarks include buoyantly-driven flow in a heated packed bed and outlet plena mixing where primary and secondary physics are decided upon using the PIRT process and analytical scaling methods.

2.2.3 Use of Simulant Fluids in Reduced-Scale Experiments

Simulant fluids in reduced-scale experiments have been used in a wide variety of disciplines where challenging conditions (i.e. toxicity, adverse operating conditions, etc...) and oftentimes cost prevent the use of the actual working fluid at prototypical conditions. The principle behind using simulant fluids is rooted strongly in fundamental fluid mechanic pedagogy where the universal structure of the model (i.e. governing PDE's) is held equivalent while the combination of microscopic phenomenological parameters of the working fluid (i.e. intrinsic thermophysical properties) must be mathematically equivalent. To put this slightly different, phenomena are considered physically similar "if they differ only in numerical values of the dimensional governing parameters; the values of the corresponding dimensionless parameters $\Pi_1, \ldots, \Pi_m$ being identical"[8]. Properly scaled experiments maintain geometric, kinematic, and dynamic similarity between the model and the prototype (subscripts p and m refer to prototype and model respectively).

Bardet and Peterson [7] demonstrated for high-temperature liquid salt reactors that by adjusting the length, velocity, average temperature, and temperature difference scales of the experiment, it is possible to simultaneously match the Reynolds (Re), Froude (Fr), Prandtl (Pr) and Grashof (Gr) numbers for heat transfer experiments. The light mineral oil, Dowtherm A, can be used to simulate flibe with reduced heat input and pumping power. At 110°C, the oil Pr matches 600°C flibe, and at 165°C, the oil Pr matches 900°C flibe. Re, Fr, and Gr can then be matched with length scale reduced to 40%, velocity scale to 63% and temperature difference scale to 40%. Mechanical pumping power and heat input for heat transfer experiments are then reduced to about 1% of the prototype power inputs. In addition to the above dimensionless parameters, it is also worth noting that both Richardson (Ri) and Rayleigh (Ra) numbers, which are important for buoyancy-driven flow, are also matched using Dowtherm A by virtue of the fact that Re, Gr, and Pr numbers are preserved (more on the Ri number is discussed in the following section),

$$\Pi_{Ri} = \frac{g\beta\left(T_H - T_C\right)L}{u^2} = \frac{\left(\frac{g\beta(T_H - T_C)L^3}{\nu^2}\right)}{\left(\frac{uL}{\nu}\right)} = \frac{\Pi_{Gr}}{\Pi_{Re}^2} \tag{2.1}$$

$$\Pi_{Ra} = \frac{g\beta\left(T_H - T_C\right)L^3}{\nu\alpha} = \left(\frac{g\beta\left(T_H - T_C\right)L^3}{\nu^2}\right)\cdot\left(\frac{\nu}{\alpha}\right) = \Pi_{Gr}\cdot\Pi_{Pr} \tag{2.2}$$

While it is true that simulant fluids were not dominantly used during the validation of LWR simulation codes, alternative working fluids have been used extensively during the validation process and deemed acceptable by the NRC. Historically, two-phase flow models have been validated for a range of phenomena using simulant fluids building on the experimental experience with water under prototypical conditions. For example, refrigerants such as freon R-12 with relatively low latent heat of evaporation has been used as a means of validating two-phase flow stability models at reduced power [22, 37] while bubbly flow phenomenology has been investigated using air and water mixtures [88] just to name a few. Additionally in the case of severe accidents, bismuth alloys have been used to simulate corium [51] where prototypical melts are substantially more expensive to generate. Good overviews of simulant experiments investigating severe accident phenomenology are given by Corradini [18] and Berthoud [13].

The challenge for reactor designers working on innovative technologies is systematically increasing the validation domain while minimizing upfront financial risk (more in reducing complexity is found in the next section). The experimental validation program proposed for the AHTR (Figure 2.3) is structured to follow the phased approach recommended by the Generation IV Roadmap [17], consisting of Viability, Performance, and Demonstration phases. This phased validation approach targets research investments to address key viability questions surrounding experimental validation early and to support subsequent decisions to proceed with subsequent phases involving detailed design, licensing and construction of a 16-MWth Test Reactor [29].

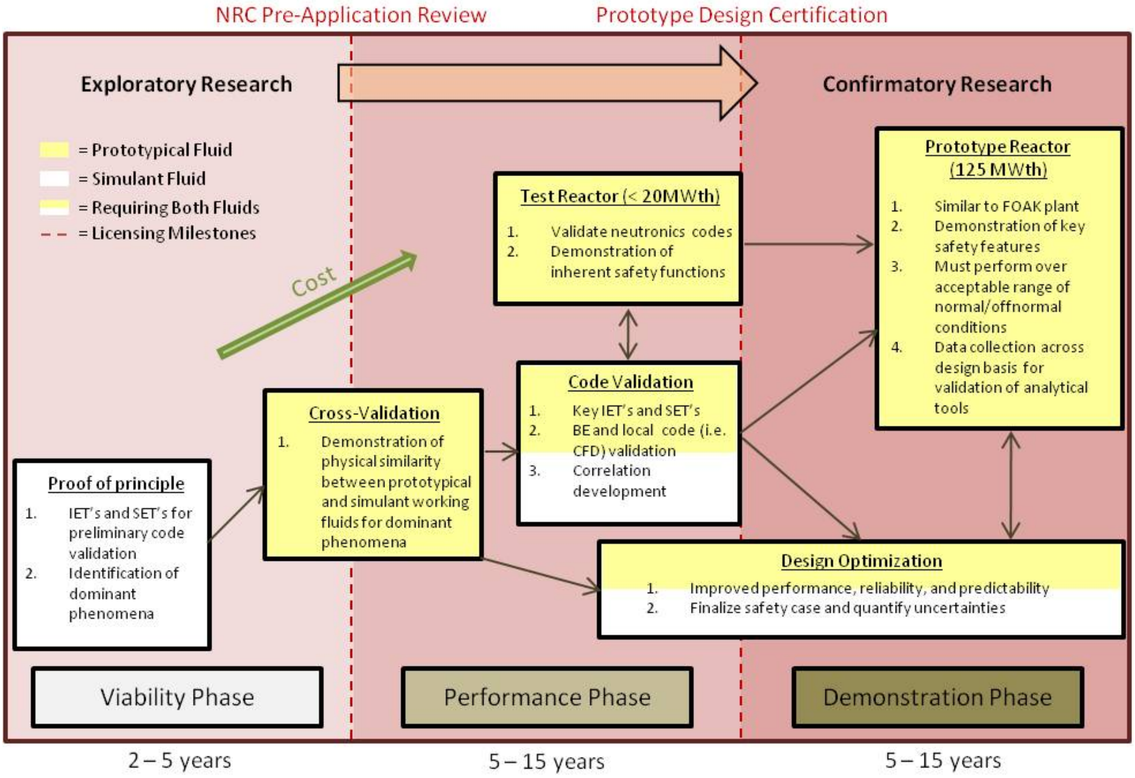

Figure 2.3: Phased Experimental Validation Program Using Both Simulant and Prototypical Working Fluids from Viability to Demonstration of AHTR Technology

The phased experimental validation program discussed above does not include the necessary validation experiments for system and component reliability such as a Component Test Facility (CTF), as it is not the focus of this dissertation. However, it is expected that these reliability-related tests must be performed using prototypical fluids under expected operating conditions due to the nature of the phenomenology as discussed at the beginning of this chapter[4]. The cross-validation process shown in Figure 2.3 is an integral component of the experimental validation program as it establishes the level of acceptable use of simulant fluids early in the licensing process. Due to the wide range of phenomenology occurring over the design basis envelope, the judicious selection of cross-validation experiments will be an integral component of the AHTR experimental validation program.

[4]A quick caveat to this statement is the role of reliability of passive safety systems where functional failure (as opposed to hardware failure) can play a significant role in reliability making the use of simulant fluids acceptable. More on functional failure can be found in Burgazzi [15], Delaney et al. [49], and Mackay et al. [30].

2.2.4 Reducing Complexity in Reactor Design

There are two fundamental strategies in reducing complexity in advanced reactor concepts that can be generally classified as parsimonious design and uncertainty reduction-driven design. These strategies are diametrically opposite but are both, in fact, used in concert during the development of Gen-IV reactor technology. Parsimonious design focuses on the identification and selection of materials and/or design configurations where significant overlap between validation and application domains already exist or require minimal resources to achieve. A good practical example includes recently proposed small, modular LWRs where the current suite of regulatory-approved computational tools is applicable and licensing regulations already exist. Uncertainty reduction-driven design focuses on increasing the validation domain through experiment and simulation thus reducing the region of the application domain not encompassed by the validation domain. Much of current academic and DOE laboratory R&D development falls directly in this category and typically requires significant resources to achieve. While both strategies are employed early in the AHTR development and the tradeoffs between both have been hotly contested, the focus of this section is on the role of parsimonious design in advanced reactor concepts.

In order to ensure the safety and reliable performance of nuclear reactors, a set of functional requirements must first be identified by which the reactor can be evaluated. Current LWR technology safety is evaluated by a set of high level functional requirements codified in 10CFR50 Appendix A as General Design Criteria (GDC). New innovative reactor technology will have to meet a similar set of design criteria that is technology-neutral in nature but maintains the same level of safety standards[5]. Therefore using Suh's [73, 74]axiomatic approach to design theory, complexity in reactor design can be defined as a measure of uncertainty in achieving a desired set of functional requirements and represents a series of tradeoffs and varying risks. The hypothesis of Suh's axiomatic design theory is that good design practice is governed by underlying principles, namely two key design axioms:

- Axiom 1: Maintain the independence of the Functional Requirements (FR).
- Axiom 2: Minimize the information content of the design.

The first axiom is known as the independence axiom and helps avoid unnecessary redundancy and economic impact in the design. By mandating that each FR must be independent of one another, the designer can ensure that each FR can be met without affecting each other. The focus of this section is on the second axiom that is known colloquially as Ockham's razor principle. This principle serves as the governing heuristic by which parsimonious design is based. Parsimony, or in philosophical circles, ontological

[5] A good discussion on the challenges surrounding the development of Gen IV regulatory design criteria can be found in Fleming and Silady [32] and a white paper for the PBMR approach to PRA [59]. A set of regulatory design criteria for the AHTR has been identified in Peterson et al. [29].

simplicity, has historically played a prominent role in physics guiding the development of a wide range of breakthroughs from quantum mechanics [66] to Einstein's special relativity [54] prompting him to say later in life, "Any intelligent fool can make things bigger and more complex... It takes a touch of genius — and a lot of courage — to move in the opposite direction." In the nuclear thermal-hydraulics community, this axiom has been advocated vociferously by Zuber [91] and others [80, 36]as guiding the development of what is now considered the Fractional Scaling Analysis (FSA) method. Zuber notes [91] simplicity, parsimony, synthesis, efficiency and versatility are all features of FSA used to scale all transfer processes associated with particles, waves, diffusion and vorticity (synthesis) across hierarchical levels[6].

The focus of this section, however, is parsimony in the design of engineered systems and not the guiding principles behind theory choice and development. By taking advantage of the inherent characteristics of the systems, structures, and components (SSC's) and constituents making up the reactor, simplicity can be introduced into the design through intelligent design and natural forces. Some examples in parsimonious design include the selection of single-phase working fluids[7] (i.e. liquid salt, sodium, etc...), highly refractory materials with large thermal inertia, and passive safety systems. From an experimental standpoint, this greatly reduces the amount of phenomenology that needs to be validated and physical similarity criteria needed to be maintained. For example, Wulff and Rohatgi [87] identified a total of 127 phenomena for the five main time phases for a cold-leg break LOCA in an AP-600. Of the 127 phenomena, 75 were found to be of first-order importance and 39 to have top priority importance, respectively, based on quantitative scaling ranking methods discussed later in this chapter. From a simulation standpoint, a reduction in important phenomenology can result in allowing the modeler to put more physics in the governing PDE's and reducing the number of required empirical closure relations. Sub-grid physics in LWR system codes such as RELAP require a large amount of calibration or tuning to fit experimental data, oftentimes resulting in compensating for multiple errors. Additionally, reducing the amount of physics needing to be captured allows for simpler and more efficient algorithms resulting in less truncation physics and numerical error.

The final component to utilizing parsimonious design in advanced reactor development is designing systems that are capable of achieving multiple FR's synergistically. The most effective way to achieve safety in new reactor technology is to use approaches that maximize the common objectives of safety, security, reliability, and economics. However, it must also be recognized that there are some areas where safety, security, reliability and economics requirements will not all align. The best design approach involves solutions that minimize these competing conflicts. For example, both air and water-cooled passive decay heat removal systems in next generation reactor technology require large volumes of space in the overall physical arrangement in the plant. However, these structures require

[6] Ranging from the Kolmogorov's micro scale to plant-wide response.

[7] Operating at or near atmospheric pressure thus eliminating the possibility of any stored energy source.

little operational maintenance and provide large physical barriers between the reactor core and maintenance access points that require physical protection (i.e. external events or radiological sabotage). Additionally, the lack of required frequent surveillance and maintenance (as with active safety systems) reduces the likelihood of introducing foreign material into the system during routine inspection as well as minimizing potential worker dose issues. The identification of these synergistic objectives early in the design process and subsequently evaluating their tradeoffs can result in better designed systems.

Chapter 3

Hierarchical Organization of Engineered Systems

3.1 Hierarchy in Reactor Systems

3.1.1 Characteristics of Hierarchical Systems

In his seminal work, Zuber [90] developed a two-tiered approach that examines the reactor system from the top down (inductive) and from the bottom up (reductionistic) in order to identify dominant phenomena affecting the response of the system. Also known as a holistic approach to system scaling, inductive methods place a strong emphasis on the system performance as a whole and attempt to find the simplest explanation for the underlying phenomena (i.e. inductive inference). Reductionism involves decomposing the system into isolated processes that can be studied independently. The reductionist approach starts at the smallest level such as the structure of the atom in order to deduce the behavior of the whole system through causal relations. Also known as deductive logic, the reductionist approach is ontologically mechanistic at heart and is most valuable when system synergism is of lesser importance. The various characteristics and traits of both approaches are illustrated below in Figure 3.1.

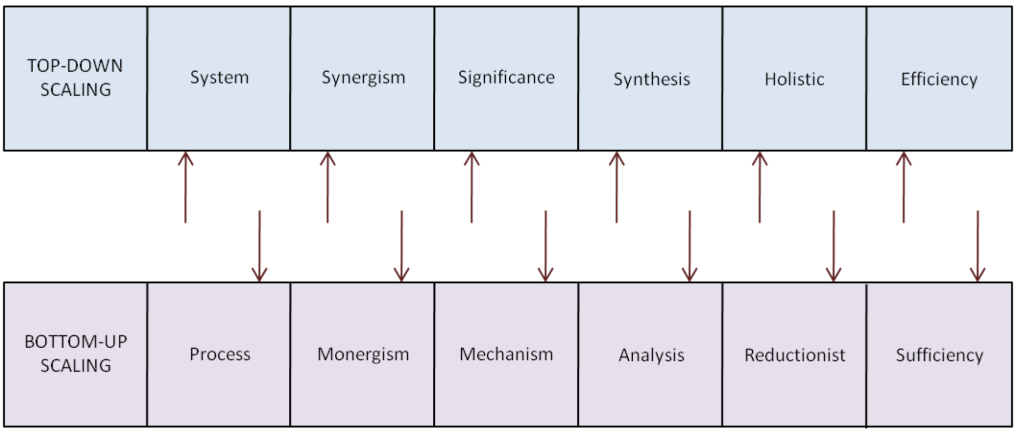

Figure 3.1: Contents and characteristics of top-down and bottom-up scaling

In the case of advanced reactor technologies, the sum of the responses of each individual part often do not equate to the overall system response as many of these dynamic component interaction processes are nonlinear. Complex systems are thus characterized by an emergent property (or emergent quality) that cannot be exhibited by the parts alone [40]. As famed evolutionary biologist, Sir Julian Huxley, noted in his Romanes lecture of 1943 [35], "increase in organization is for the most part gradual, but now and again there is a sudden rapid passage to a totally new and more comprehensive type or order of organization, with quite new emergent properties, and involving quite new methods of further evolution". In this chapter, the role of hierarchy and asymptotic analysis are further discussed within the context of experimental validation of new reactor technology.

3.1.2 Reactor System Hierarchy

Nuclear power plants are systems of organized complexity that can be decomposed into their respective subsystems that are in turn made up of a set of interacting modules, or components. Each module is made up of constituents, or materials, that can in turn be divided into associated interacting phases (i.e. gas, liquid, solid). Finally, a geometrical configuration characterizes each phase which can be described by the governing equations for mass, energy, momentum. By breaking down the system into a series of levels, or stratas, the hierarchical architecture of the system can be established and provide a rational basis for the top-down and bottom-up scaling analyses. It is also important that concept of the observer is introduced where the "system" under consideration is defined by a control volume, or "window" [90], at the appropriate hierarchichal level of observation. Therefore by decomposing the system into hierarchical levels, one can associate three independent measures for each transfer process at each level: an overall available transfer area characterized by a spatial scale (L), a volume fraction (α) indicating the volume occupied by a given constituent or phase, and a temporal scale (τ).

Take for example the highly simplistic reactor configuration as illustrated below on the far right side of Figure 3.2. The working fluid is considered to be a single-phase fluid circulated actively using a pump where heat is transferred to the fluid in the core region and subsequently removed via the heat exchanger for a wide variety of applications (i.e. generate electricity, process heat, etc. . .).

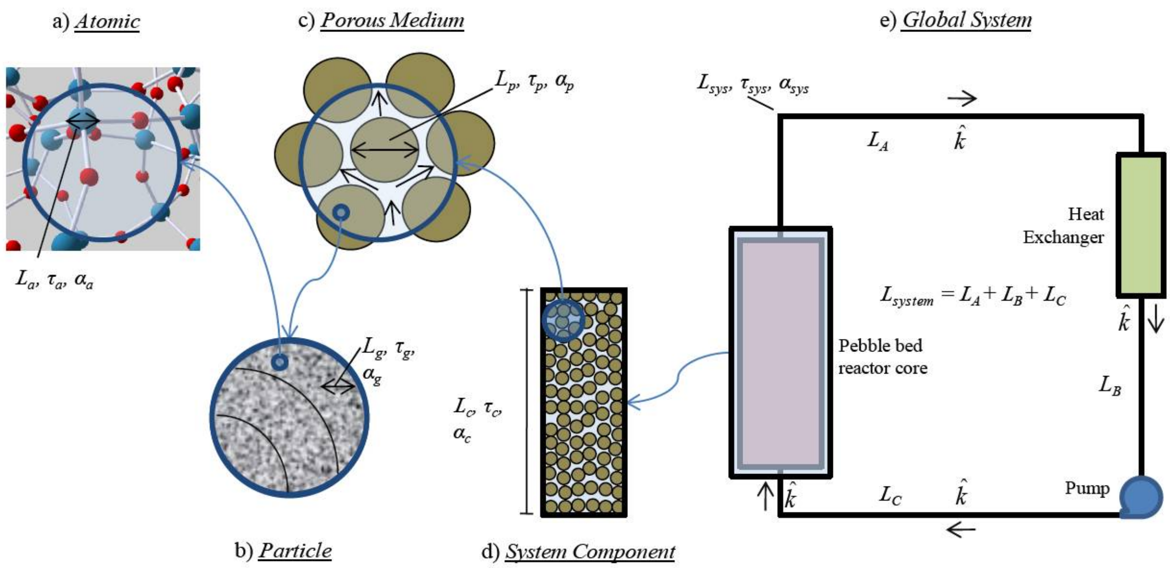

Figure 3.2: Sample flow diagram illustrating system hierarchy across many spatial and temporal scales for a simplistic reactor loop

Starting from the right side the global system level, the characteristic time and length scales are very large and represent the average total system length, L_{sys}, and transit time of a fluid particle, τ_{sys}, (typically on the order of magnitude of 10's of meters and 10's of seconds respectively). Moving left in the figure, the next level of interest is at the system component level where the primary interest is in the integral response of the component of interest. Take for example the core region where we are interested in the total heat transfer to the working fluid as well as the pressure drop across the pebble bed due to form and friction losses where one is concerned with component length scales, L_c, and component time scales, τ_c (typically on the order of magnitude of meters and seconds respectively).

Going to even smaller temporal scales, the local characteristics of the pebble bed (Figure 3.2c) can be further investigated by invoking a porous media approach where volume averaged transport equations, suggested by Darcy, are used to determine the local flow conditions. In the case of porous media, the engineer is concerned with component length scales, L_p, and component time scales, τ_p (typically on the order of magnitude of centimeters and milliseconds respectively). The global performance of each fuel pebble depends on the integrity of the fuel particle (made of UO_x or some other fissile or fertile seed fuel) and the subsequent thermal and mechanical stresses affecting the layers surrounding the fuel. Here the concern is primarily around failure degradations at the grain level where the length scales are on the order of a nanometer and the corresponding time scales can vary depending on the physical process under consideration (Figure 3.2b).

Finally, one must of course go to the atomic level where the primary concerns are with the nuclear interactions of the fuel where nuclear reactions are of ultimate importance. Additionally, materials in high-flux regions can be affected by several irradiation degradation mechanisms (i.e. displacements) that occur at the atomic level. For atomic interactions, the length scale of interest is between angstroms and femtometers depending on the interaction of interest. A typical value for the mean lifetime of a thermal neutron in a reactor is on the order of microseconds.

This dissertation focuses roughly on the first two levels on the right side of Figure 3.2 which are broadly classified as the system, subsystem (more is discussed in Section 3.3), and component level. In the next section, an analogy is drawn between the use of intermediate asymptotics and establishing hierarchical levels by which physical similarity criteria are derived.

3.2 Analogy with Intermediate Asymptotics

In order to better understand the relationships within the hierarchical system, the concept of intermediate asymptotics [1] must first be introduced. Intermediate asymptotics were first formally introduced by Zeldovich and Barenblatt in the early 1970's

[1] Sometimes referred to as asymptotic analysis.

[10, 8](although as noted by the author the concept was used implicitly before this). As discussed by Barenblatt [8], self-similar solutions are not just elegant solutions to classical problems but can characterize the "intermediate-asymptotic behavior" of the system that are insensitive to initial and boundary conditions.

3.2.1 Example 1: Spherical Shockwaves in Air

In order to better understand the concept of intermediate asymptotics, it is important to review a few insightful examples starting with the classical example of the mechanical action of a spherical blast following the initial stages of a nuclear explosion (phenomenology of the thermal and gas-dynamic nature) solved independently by Sedov [69] and Taylor [76][2] where the latter work is discussed here. Taylor realized very early on that an analytical solution to the governing PDEs of motion inside the shock wave (mass, momentum and energy) was completely impractical and he would have to replace the problem by an 'ideal' one [9].

The first assumption he made was that a finite amount of energy was suddenly released in an infinitely concentrated form. This physical assumption led him to argue that the initial radius of the shockwave, r_0, could be ignored if one was interesed only in the mechanical action occuring at a much larger shock front radius, r_f, leading to his initial assumption that $r_f \gg r$. The consequence of this assumption is that all the initial conditions with respect to density, presure, and velocity distributions inside the initial shock wave are no longer necessary resulting in a great simplification.

Taylor's second major assumption was that the pressure of the moving gas is at a maximum (i.e. shock-wave front) and is much larger than the ambient pressure in the ambient air, p_0, thus leading to $p_f \gg p_0$. The result of this assumption is that detailed information surrounding p_0 is neglected in the shock-wave front and in initial conditions [9]. Using these two key assumptions, Taylor realized the important governing parameters in the problem could be reduced to the energy of the blast, E, the density of the air, ρ, the radius of the blast wave, r, the time elapsed, t, and a non-dimensional constant, γ, known as the adiabatic index. Taylor subsequently used dimensional analysis to form the famous scaling law for strong spherical shock waves using the following dimensionless variables,

$$\frac{p}{\rho_0 r^2/t^2}, \; \frac{\rho}{\rho_0}, \; \frac{v}{r/t} \tag{3.1}$$

Where the only dimensionless combinations of these variables results in the following relationship,

[2] J. von Neumann is oftentimes also associated with the original development of the blast scaling law.

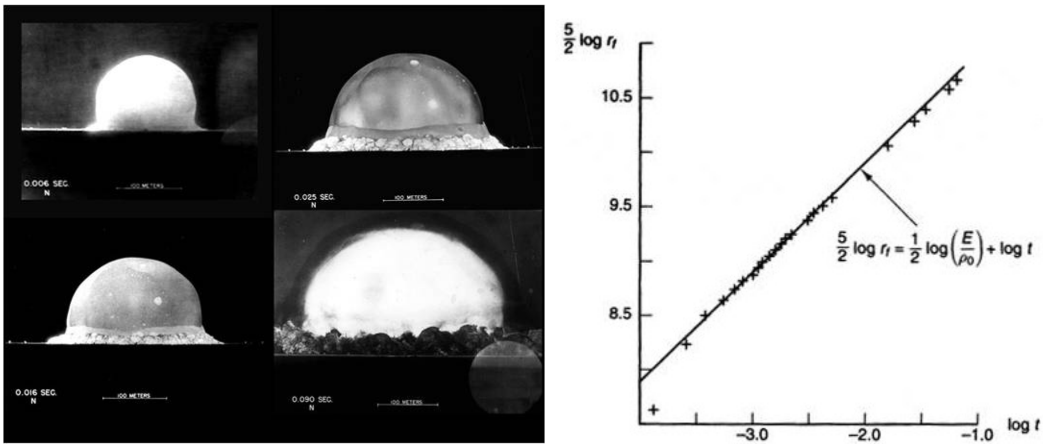

Figure 3.3: Series of photogaphs taken from J. E. Mack of the first atomic explosion, *Trinity*, in New Mexico (left) and Taylor's blast scaling law on a log-log plot [76] (right)

$$\xi = \frac{r}{(Et^2/\rho_0)^{1/5}}\,,\ \gamma \tag{3.2}$$

Using the scaling relationship (3.2), Taylor was able to compare publicly available photographs of the Trinity blast and compared them to his derived relationship where he was able to back out the adiabatic constant for air (he determined it was 1.033 which was very close). Using this relationship, Taylor was able to determine the yield of Trinity which was previously highly confidential leading to much consternation in the United States military. The relationship in Figure 3.3 is one of the best illustrations of intermediate asymptotics as it shows how the scaling law breaks down at very small time scales where the first assumption about the radius of the shock-wave front ($r_f \gg r_0$) no longer holds true as well as at larger time scales where the second assumption ($p_f \gg p_0$) also no longer holds true.

3.2.2 Example 2: Aerodynamic Boundary Layer

Revisiting the classical aerodynamical boundary layer problem discussed in the first chapter, Prandtl and others used a similar rationale by noting that approximations are only valid in certain spatial regions thus the flow over a wing is divided into two regions where the flow is treated as viscid in the boundary layer that forms on the wing surface and inviscid in the mean stream. If one ignores the entrance conditions at the front of the wing and the trailing edge region where vortices are created (another case of intermediate asymptotics where the characteristic lengths of each region is much smaller than the remainder of the wing section), the classical non-dimensional form of NSE (x-direction) can be written as,

$$u^*\partial_x u^* + v^*\partial_y u^* = -\partial_x p + \left(\frac{1}{Re_L}\right)\partial_{xx}u^* + \left(\frac{L^2}{Re_L\delta^2}\right)\partial_{yy}u^* \tag{3.3}$$

where $y^* = y/\delta$ and δ is assumed to be a very small distance with respect to the characteristic length of the wing, L. Assuming a high Reynolds number, the first viscous term on the RHS can be assumed to be negligible whereas by inspection the two advective terms on the LHS can be assumed to be on the order of unity. Assuming the static pressure does not vary in the flow direction, the boundary layer thickness over a flat plate can be approximated as,

$$\delta \sim \left(\frac{1}{Re_L}\right)^{1/2} \tag{3.4}$$

However what if the focus is now at much smaller spatial scales such as the behavior of nanoparticles near the wall. The problem statement has thus changed and the assumption in Eq. 3.3 that there is no slip at the wall becomes invalid. This is due to the fact that the length and time scales associated with the flow are comparable with the corresponding molecular mean free path in the fluid. This ratio, known as the Knudsen number, gives an indication of the validity of invoking a statistical approach (i.e. statistical mechanics) or a deterministic approach (i.e. continuum approximation).

3.2.3 Summary

The asymptotic nature of these physical assumptions can be best thought of qualitatively as a microscope or telescope coming into focus. In the case of the boundary layer problem, the resultant solutions are only valid where the viscous forces dominate and start breaking down as we move further away from the wall into the inviscid region. This asymptotic region is a function of the spatial and temporal scales of the control volume assigned to the problem of interest. If one magnifies too far or not far enough, the governing physical assumptions break down. In other words, when we speak of multi-physics simulation as illustrated in Figure 3.2, we are referring to a multi-level approach where we rely on physical models that cover several disciplines within the field. Phenomenology that evolves slowly also demonstrates these same hierarchical characteristics however statistical methods are required as we move to physics where the continuum assumption breaks down. Information from faster and more local processes is transferred upwards towards global processes characterizing the larger-scale evolutions occurring in the plant determining overall materials performance. It is also important to point out that usually the time-averaged integral of information and associated consititutive relationships can have good predictive power. Much like the analogy with the boundary layer, the direction by which the system hierarchy is analyzed is non-conservative and yields different insights. In the following section, the reference reactor for the dissertation is described in detail while establishing a rational for the hierarchy architecture.

3.3 Advanced High Temperature Reactor

It was not until the early 2000's with the introduction of the Liquid Salt Very High Temperature Reactor (LS-VHTR), that research in molten salts as reactor primary fluids was renewed in the United States from the work done at ORNL during the 1960's and 1970's. The LS-VHTR was essentially a modified helium-cooled VHTR using liquid salt as the primary coolant, which operates at near atmospheric pressure and substantially greater power density. This reactor configuration with the fuel being separated from the coolant represented a significant departure from the liquid fuel MSR technology being developed in the 1960's. Most recently in the Gen IV roadmap, [17], the term AHTR has been used to describe fluoride salt cooled, high temperature reactor technology that uses solid fuel.

The PB-AHTR, developed at UC Berkeley in collaboration with Oak Ridge National Laboratory, is the latest design based on the original AHTR concept to use liquid fluoride salt to cool coated-particle high temperature reactor fuel. In the following two chapters, practical examples are given using the AHTR as the reference reactor. The AHTR takes advantage of technologies developed for gas-cooled high temperature thermal and fast reactors, sodium fast reactors, and molten salt reactors. Coated particle fuel has recently undergone rapid design evolution and is currently undergoing extensive irradiation testing. The modular 900-MWth PB-AHTR is the reference design for this chapter but it is expected the core and system configuration will evolve with time. Therefore, AHTR and PB-AHTR will be used interchangeably however when referring to specifics surrounding the core where PB-AHTR will be specified.

3.3.1 PB-AHTR System Description

In Figure 3.4, the primary loop of the most recent design of PB-AHTR is represented by the blue line connecting the core and the intermediate heat exchanger (IHX) modules. During a loss of forced circulation (LOFC) transient (i.e. after a primary pump trip), a natural circulation flow loop is formed between the core and a set of Direct Reactor Auxiliary Cooling System (DRACS) heat exchangers (DHX modules). The DRACS heat exchangers transfer heat by natural circulation flow of a DRACS salt from the DHX modules to natural draft heat exchangers (NDHXs) cooled by outside ambient air, as indicated by the purple flow path. Under forced circulation the reverse bypass flow through the DHX is minimized by a fluidic diode. It should be noted that the PB-AHTR, like all liquid salt technologies, is susceptible to overcooling transients where after a substantial time period the salt can freeze in the primary loop.

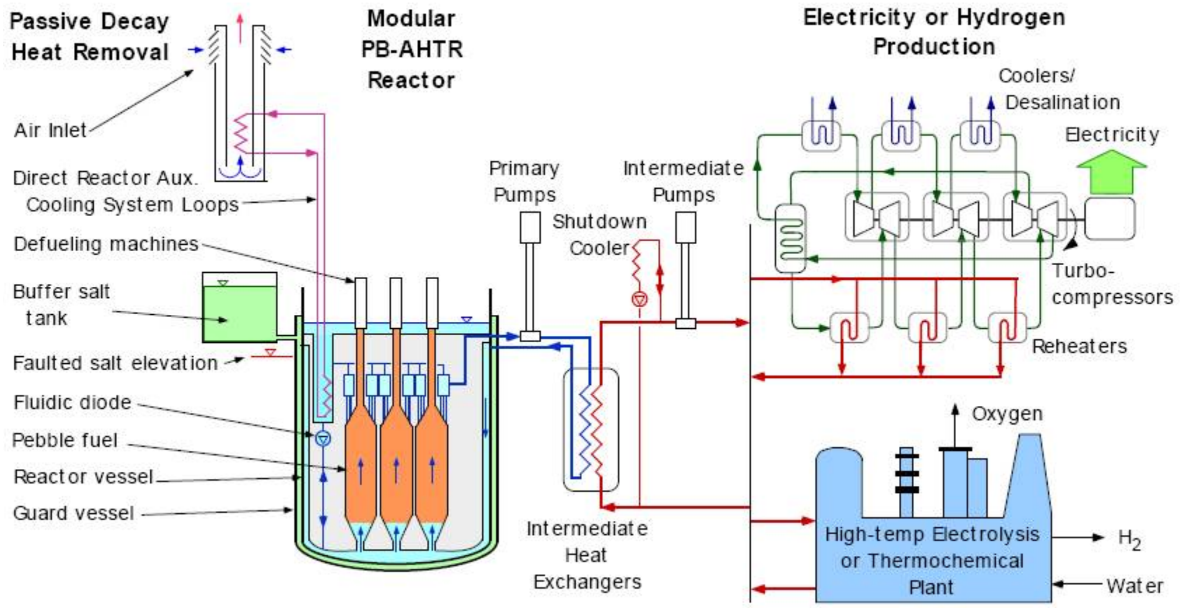

Figure 3.4: Simplified schematic of modular PB-AHTR system and possible applications.

The annular space between the reactor vessel and the guard vessel is filled with a low-cost buffer salt, a mixture of sodium and potassium fluoroborate, which minimizes primary salt inventory loss if the reactor vessel is faulted. The red flow path represents the IHX's intermediate loop which can be used to deliver thermal power to a variety of applications such as process heat for hydrogen generation or electricity generation.

The core is made up of graphite Pebble Channel Assemblies (PCA's) with channels for pebble fuel, coolant, and shutdown rods running axially up the core (see Figure 3.5 and Figure 3.6). Fuel is inserted into the bottom of the core and removed through the top of dedicated channels using defueling machines. In the current modular PB-AHTR design, the pebbles are selected to have 3-cm diameter, with a 2.5-mm thick graphite shell and a low-density inert graphite kernel at the center of the pebble, creating an annular fuel region in the pebble. Reducing the pebble diameter by a factor of two compared to the typical 6-cm diameter of helium-cooled reactor pebbles doubles the pebble surface area per unit of core volume, and halves the thermal conduction length scale in the pebble. The annular fuel configuration reduces the temperature difference by another factor of approximately two, allowing the power density to be increased by a factor of 8 while maintaining the same temperature difference from the surface to the center of the pebble. The pebble density has been selected so they are positively buoyant during design basis conditions. Flow enters the bottom of the active core at 600ºC and exits the core at 704ºC resulting in the same thermodynamic efficiency (core-averaged temperature) as a MHR.

The PB-AHTR also implements a novel buoyant shutdown rod design for passive reactivity control (see Figure 3.6 for channel locations). The insertion of its shutdown rod

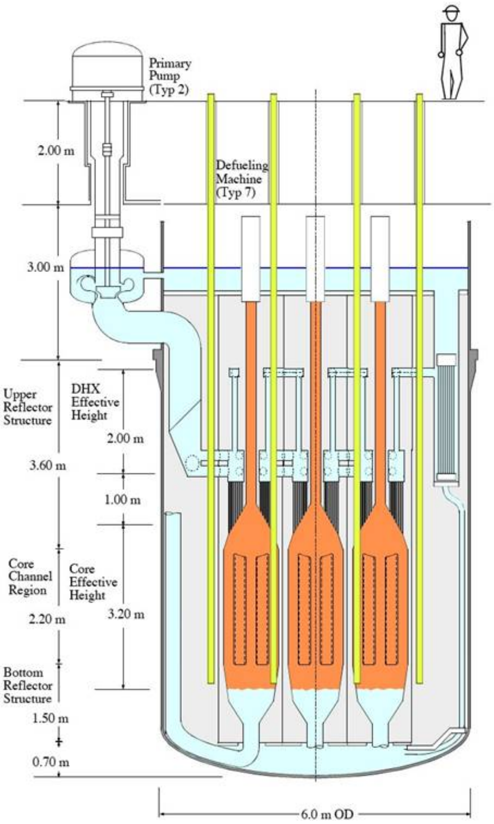

Figure 3.5: Elevation view of the modular PB-AHTR. The orange region indicates where the pebble fuel is recirculated through a series of channels consisting of graphite pebble channel assemblies.

elements provide negative temperature feedback in order to augment the negative feedback already provided by the negative coolant and fuel temperature reactivity coefficients [14]. Insertion of the shutdown rods occurs due to buoyancy forces generated by the difference between the density of the control element and the reactor coolant during an unexpected reactor transient, where forced insertion of the shutdown rods does not occur (e.g., anticipated transient without scram, ATWS). A heavy metallic driver element is suspended by a magnetic latch system above each shutdown rod but is not physically connected to the shutdown rod. In the event of a reactor scram signal, the electromagnetic coupling holding the drive elements are de-energized thus causing the elements to drive the shutdown rods into the active core region via gravity. If this active insertion mechanism does fail to operate, buoyancy forces cause the shutdown rods to insert anyhow.

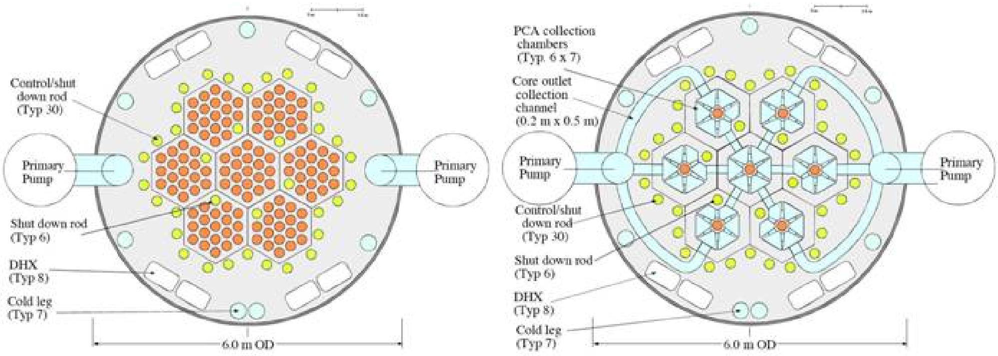

Figure 3.6: Plan view of the modular PB-AHTR at the pebble channels elevation (left) and at the core outlet plenum elevation (right) where shutdown and control rod channels are indicated.

3.3.2 PB-AHTR System Decomposition

The reference AHTR primary system is comprised of a reactor vessel surrounding a core region, two primary salt pumps, four intermediate heat exchangers, intermediate loop isolation valves, and associated inter-connecting piping. The hydraulic piping and component locations in the primary system and overall location in the reactor building are illustrated in Figure 3. A conceptual design for the core internals has been assembled where the core, inlet and outlet plena, and shutdown rod channel are depicted. Since initially the primary interest is deriving the similarity criteria at a global level early on in the design process, the detailed design of the core region is of secondary importance. For more information on the current PB-AHTR core design and past designs, the interested reader should refer to Peterson et al. [29].

The first step of the H2TS method [90] involves the decomposition of the system into its associated hierarchical levels. This process has been illustrated for many reactor concepts [41, 48, 87] and was performed for the PB-AHTR (see Figure 3.8). At the lowest level (process), the overall phenomena or transfer process importance is determined by the both the rate of transfer and the available transfer area. By breaking down the primary system into its associated subsystems and components, one is able to establish an overall hierarchical architecture with respect to spatial, temporal and energetic scales [90]. It is important to note the relative simplicity of the resultant transfer processes for the PB-AHTR due to a lack of any large stored energy source or two-phase flow.

In the next chapter, a system loop momentum balance is constructed where each closed loop in the system is modeled for the time phase of interest. The importance of dividing the system into a set of branches and loops is analogous to the treatment of multi-loop circuits where both of Kirchhoff's laws must be utilized and is discussed in detail in Chapter 4. The flow paths during forced and natural circulation for the primary system are depicted in Figure 3.10. As mentioned earlier, during the LOFC transient

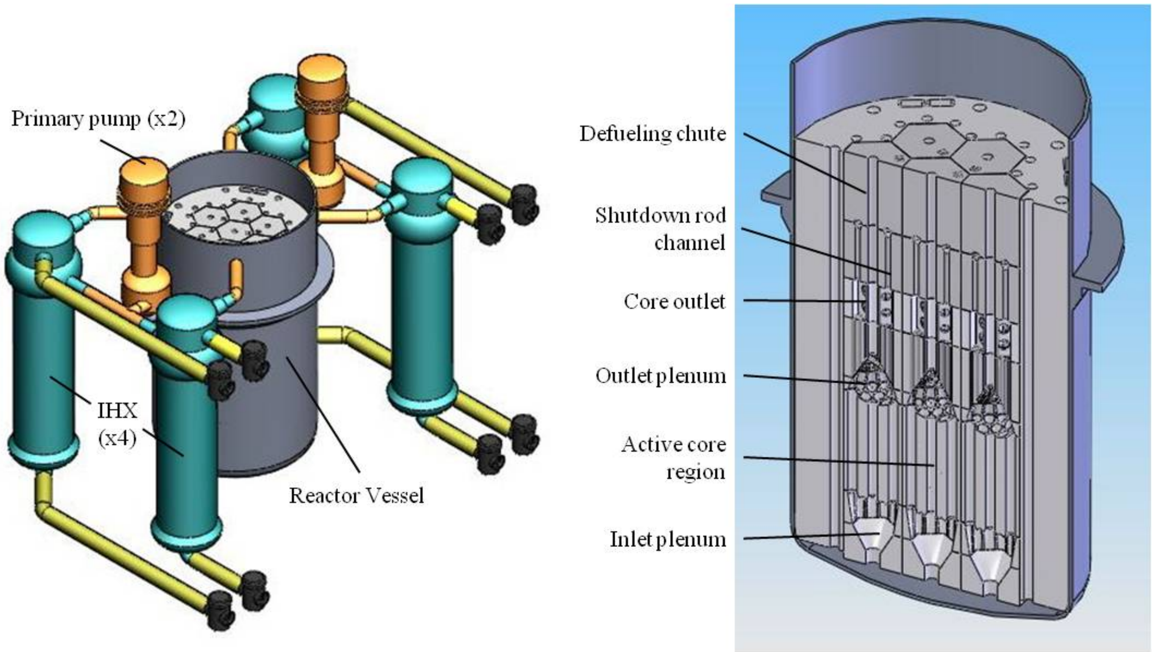

Figure 3.7: Isometric view of the (left) primary loop [active shutdown cooling system not shown] and (right) the reactor vessel.

the flow in the primary loop transitions from the forced circulation path (red) to the natural circulation path (blue) where the loops share the same region through the core (segment ab) as well as the core bypass loop segment which makes up the Shutdown Rod Loop (SRL). For the LOFC transient, we are interested in the dynamic response of the system to a simultaneous pump trip. The hydraulic system under consideration consists of a large reactor vessel, 4 intermediate heat exchangers and the flow channels that interconnect these volumes. Because the PB-AHTR operates at near atmospheric conditions, these volumes are assumed to be thermally compliant volumes as opposed to the large pressurized volumes of LWRs that are also mechanically compliant where system depressurization is the dominant phenomena.

In the first phase of the transient (a detailed description of the LOFC transient can be found in Appendix A), the primary interest is in the transition from the forced circulation flowpath to the natural circulation flowpath. The forced circulation flowpath starts at point a where cold salt enters the inlet plenum and travels up through the core and exits the core at core outlet plenum. Point b indicates the branch point between the core outlet plenum and the DHX distribution plenum (Figures 3.10 and 3.9 below). A small fraction of the flow is metered into the six shutdown rod channels at point c and travels up the core bypass (CB) region and is reintroduced into core outlet plenum at point j. It is expected that there will be leakage bypass flow through the structure of the graphite reflector blocks which is ignored for this preliminary analysis. The flow then collects into

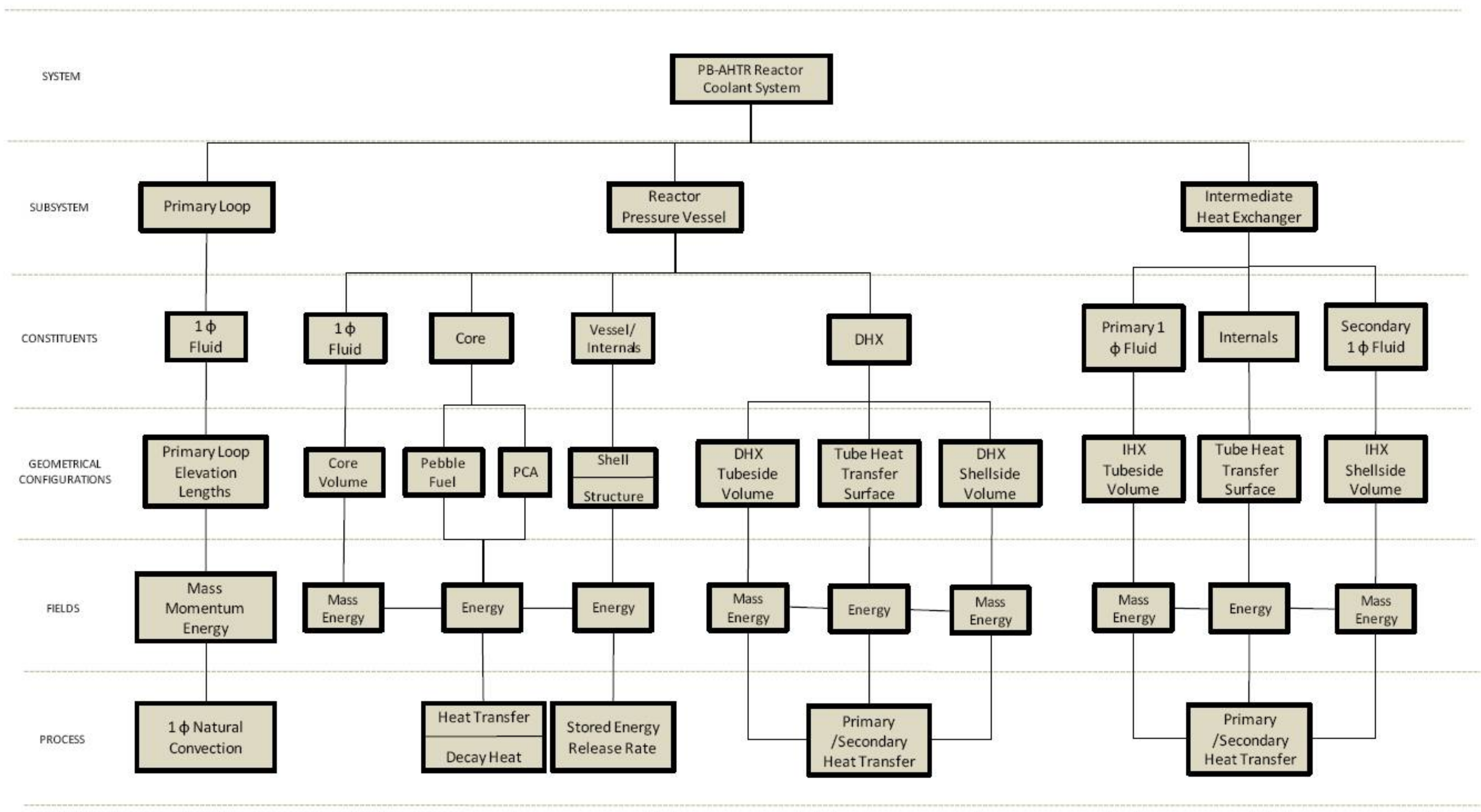

Figure 3.8: PB-AHTR reactor coolant system subdivision and hierarchy process.

the hot leg piping (HL 1 and 2) and enters pumps A and B respectively. Points d and e represent the branch points where the hot legs are split into two (HL1a, HL1b, HL2a, HL2b) ito drive all four intermediate heat exchangers. Flow then exits each of the IHX's into the 4 respective cold leg segments (CL1a, CL1b, CL2a, CL2b) and is redirected to the reactor vessel where it enters the downcomer region (point f represents the region in the downcomer where all cold leg flows collect). The primary flow then enters the core inlet plenum (point a) and the cycle repeats itself. The flowpath for the intermediate salt of the IHX's is designated by green arrows.

Under natural circulation the flow that normally collects in the core outlet plenum (point b) can also continue to travel up the riser region to the DHX distribution plena (point h) where flow is circulated to the eight DHX's located around the core via the DHX bypass loops. The salt that enters the DHX region makes up the secondary side of the DHX shell-and-tube design heat exchanger and exits through the bottom of the component where it enters into a fluidic diode that provides minimal flow resistance in this direction. The cooler fluid collects at the bottom of the core from all eight of the DHX's (point a) and continues the cycle. It is important to note that during normal operation the DHX's are in constant operation where a small amount of heat is being rejected ultimately to a DRACS natural draft heat exchanger (secondary salt flowpath denoted in purple), however in the exact opposite direction of the DBL. The fluidic diode restricts flow in the opposite direction during forced circulation where the colder fluid ultimately mixes with the hotter fluid exiting the core region in the core outlet plenum.

3.3.3 AHTR Test Reactor System Description

As discussed in Chapter 2, a commercial AHTR design will have ultimately first demonstrated at the test reactor size (<20 MWth) and/or the prototype reactor size (100-500 MWth) where capital is incrementally spent in order to demonstrate predictive capability of simulation tools. The system scaling performed for the AHTR is therefore focused on the dynamic response of a 16 MWth AHTR Test Reactor (ATR) concept that is the focus of this section. The purpose of the ATR is to validate and benchmark system codes in addition to demonstrating the overall efficacy of the primary safety systems. A reduced-scale Compact IET (CIET) is being designed to be capable of demonstrating the ATR system response due to a loss of forced circulation transient, and other transients and accidents, with minimal distortion for the dominant phenomena. Therefore, the resultant system similarity criteria will allow for comparison of numerical distortion for dominant phenomenology between CIET and ATR.

The ATR will have the ability to demonstrate the major features of the AHTR reactor class and would draw heavily on technologies already demonstrated by the 8-MWth ORNL Molten Salt Reactor Experiment with the significant difference being the use of solid, pebble fuel as opposed to liquid fuel. In addition to validating important neutronics phenomenology and core response, the ATR will be required to demonstrate system

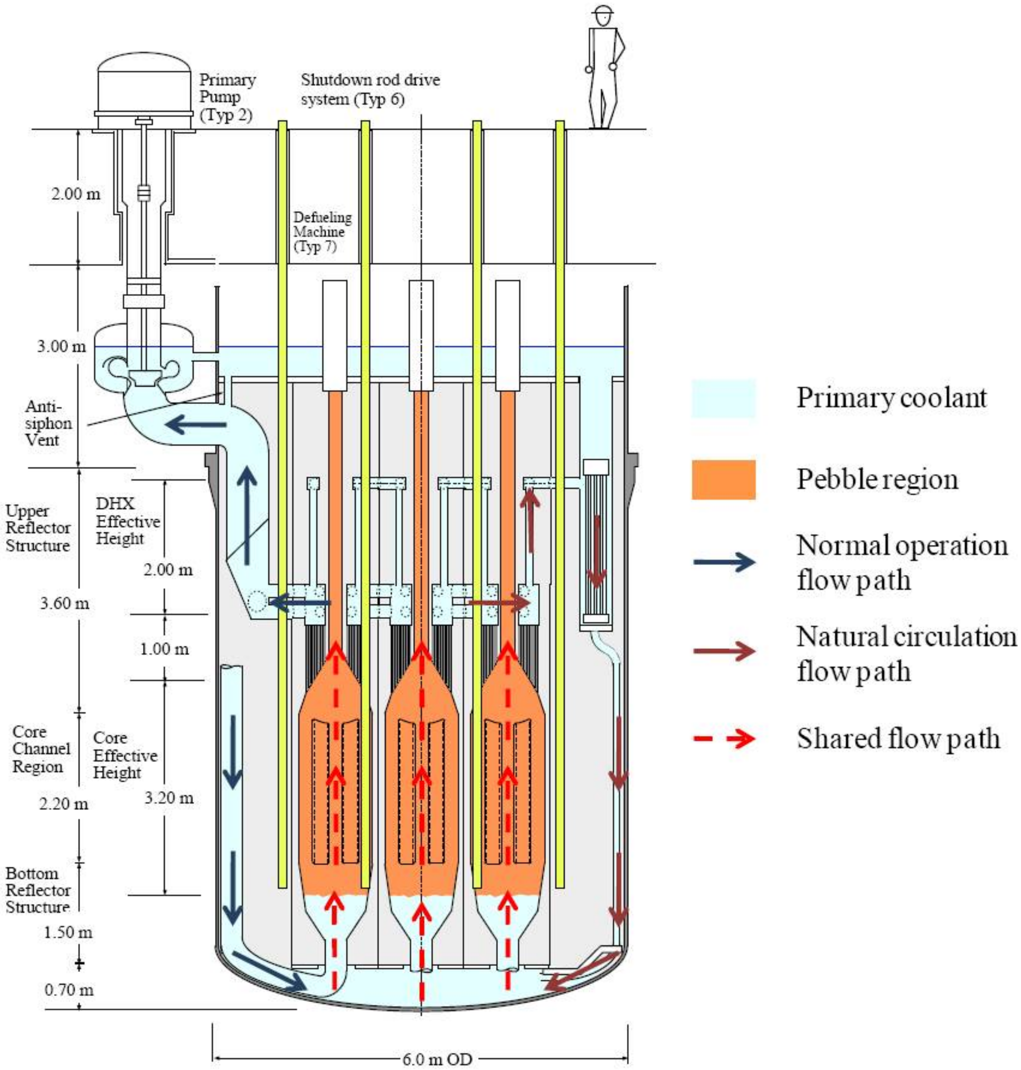

Figure 3.9: Front view of the the reactor vessel showing the two flow path directions during normal and natural circulation operation (for normal operation the natural circulation flow path is reversed due to pump driving head while the normal operation flow path is reversed when the pumps are tripped).

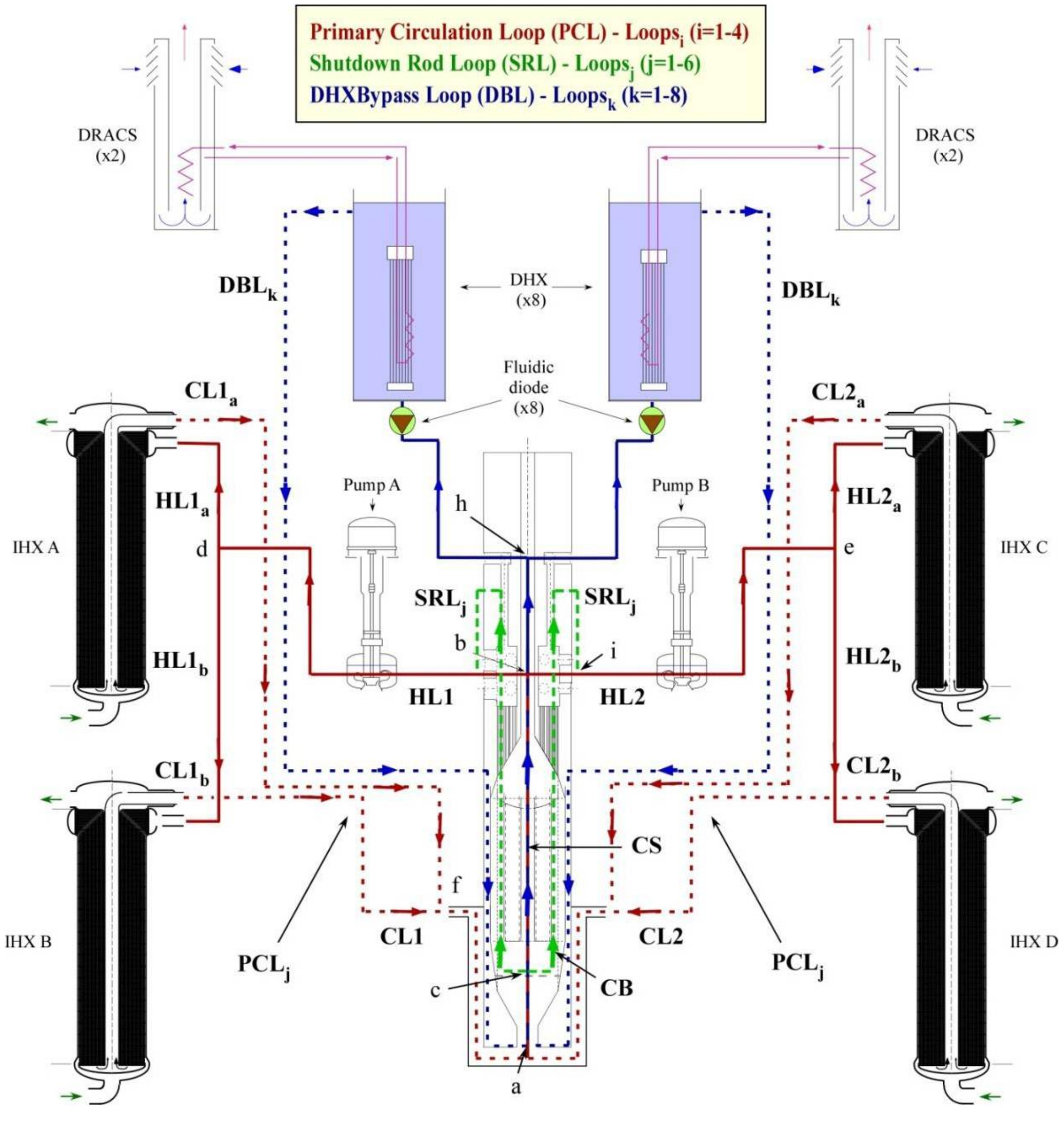

Figure 3.10: Logic diagram illustrating the various flowpaths for the PB-AHTR during a LOFC transient.

performance including, but not limited to, decay heat removal and reactivity response. Therefore, the simplified baseline ATR will demonstrate the performance of onset of natural circulation through the DHX's as well as the performance of the shutdown rod design. Due to the simplicity of the ATR, the global scaling analysis done in the next chapter focuses on the ATR design as it makes following the scaling process easier and reduces the require loops for analysis (3 versus 18).

3.3.4 AHTR Test Reactor System Decomposition

The ATR primary system is presented here (Figure 3.11) as consisting of three types of closed loops with shared sections that are constantly under operation for all three phases of the transient (more on the ATR loops are discussed in the following chapter). This simplification is introduced in order to ease the demonstration of the scaling methodology while capturing the governing phenomena expected to dominate the full system response. The overall performance of these loops under a wide range of operational modes is one of the dominant focuses of the ATR. In phase 2 and 3 of the transient (see Appendix A), the flowpaths change direction as indicated in Figure 3.9 where there is minimal circulation through the PCL. The details of each closed loop and branch points are discussed closely in the following chapter.

3.4 Scales of Interest

In the following three chapters, examples are given on the developmont of reactor similarity criteria at three distinct hierarchical levels of the AHTR: system (Chapter 4), subsystem (Chapter 5), and component level (Chapter 6). As was discussed, the identification of the control volume or scale of interest is the crucial first step in establishing a set of assumptions before developing physical similarity criteria. In Figure 3.12, a notional schematic of the AHTR is shown where the important various flowpaths are illustrated however detailed information about the subsytems and components is left out.

The first figure illustrates the control volume that encompasses the entire reactor primary system capturing global interactions between components. For any type of integral effects testing, the primary control volume encompasses the entire reactor system however typically simplifications are made about non-dimensionalizing the spatial characteristics of each loop [48, 41] (the treatment of loops is discussed in more detail in the following chapter). In the second figure, the primary control volume is selected at the subsystem level which in this case refers to the AHTR shutdown rod system. At this particular level the shutdown rod system is in fact a coupled problem where global information about the system (system level) drives the shutdown rod response (component level) while the reverse is true with the shutdown rod dynamics driving reactivity control leading to changes in the global response. Therefore at the subsystem level, a systematic approach to understanding where complexity can be minimized using decoupling boundaries ([33]) will

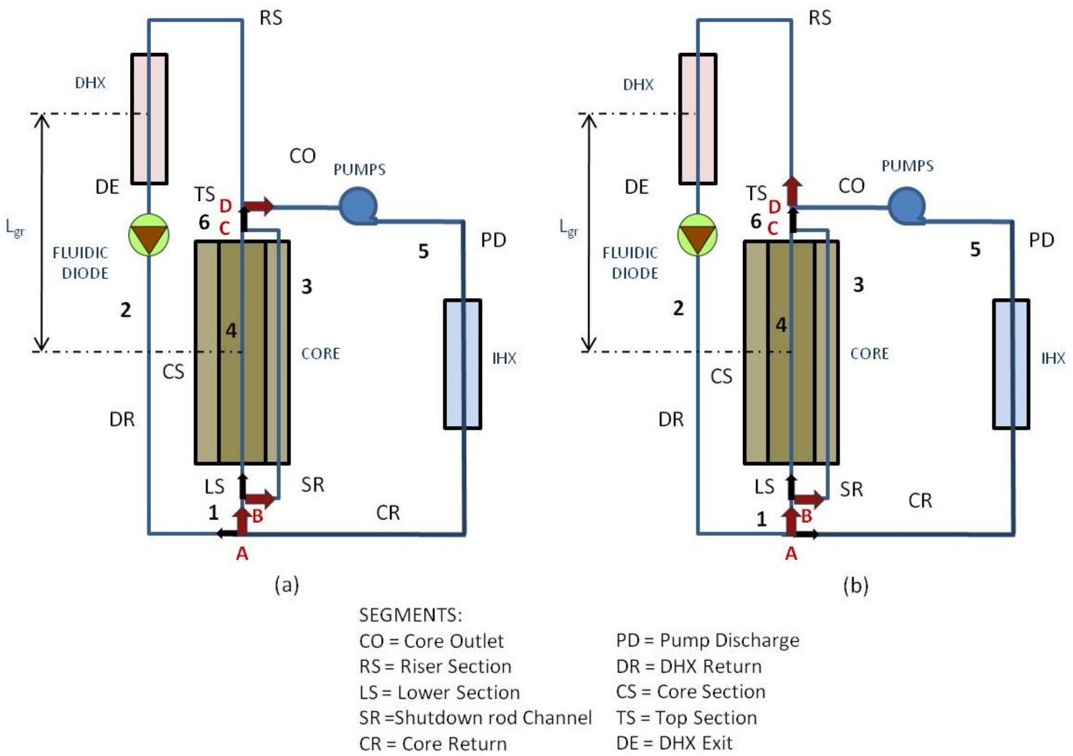

Figure 3.11: Simplified logic diagram illustrating the various flowpaths for the 16 MWth Test Reactor System during a LOFC transient before (a) and after (b) the natural circulation flowpath has been established.

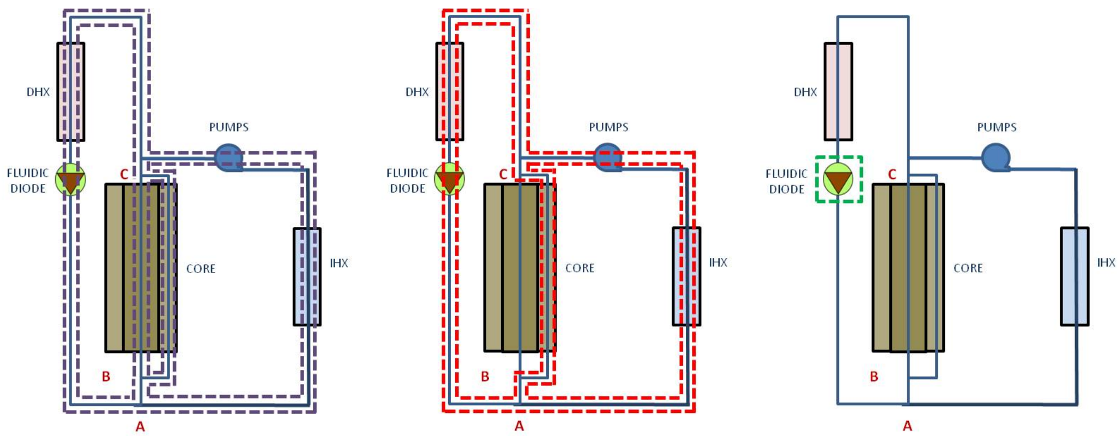

Figure 3.12: Starting from left to right, the identification of the control volume for problems at the system (purple), subsystem (red), and component level (green) for the AHTR

be required and is the focus of Chapter 5. Finally in the third figure, the scale of interest is solely at the component level where the focus is on the performance of the fluidic diode and establishing similarity criteria. In the case of all reactor components (i.e. core, DHX), the analysis of these systems can be decoupled from the system analysis however the *performance* of these systems cannot be fully ascertained as the global response is what drives the boundary and initial conditions. This is an extremely important point to make and is one of the major limitations of bottom-up scaling methods (more on this idea will be a strong focus in Chapter 6).

Chapter 4

Physical Similitude at the System Level

4.1 Global Response of the AHTR

In order to assess the global response of the AHTR, an inductive approach to scaling must be employed. As discussed in Chapters 1 and 3, inductive methods start with the whole and work down to the physical process levels where the emphasis is on overall system importance as opposed to specific mechanisms. The importance of identifying key phenomena, or dominant processes, cannot be overemphasized. The PIRT process can be highly subjective for complex engineered systems where the experience base is small (see Chapter 2). A methodology developed by Zuber et al. [53] called Fractional Scaling Analysis (FSA) identifies dominant processes, such as stored energy in the fuel, ranks them quantitatively by importance and provides a more rigorous foundation for the PIRT process. FSA has been demonstrated at the system level [87, 80] and at the component level [36] for PWR SBLOCA analysis, however it has yet to be applied to Gen IV reactor types. In this section, FSA and the Causative Process Scaling Analysis (CPSA) method are demonstrated at the system level for the AHTR where the focus is on developing similarity criteria first at the highest level of the reactor system. The role of the low-pressure containment is not discussed in this work as the main interest is in the primary reactor system design and there are no design basis events that can result in pressurization of the containment.

4.2 Scenario Description and Figure of Merit

The scenario of interest for this scaling analysis is a loss of forced circulation (LOFC) transient (i.e. after a primary pump trip) where a natural circulation flow loop is subsequently formed between the core and a set of DRACS heat exchangers (DHX modules). The DRACS heat exchangers transfer heat by natural circulation flow of a DRACS salt from the DHX modules to heat rejection exchangers cooled by outside ambient air. Appendix A provides a detailed description of each phase of the transient.

It is important to note that for the case of the AHTR, the figure of merit during a LOFC is the peak temperature of the metallic structures in the primary system and not the fuel temperature. These metallic structure are susceptible to an array of failure degradations (predominately creep-related) at elevated operational temperatures well below the fuel failure temperature. The AHTR fuel failure threshold is above 1600°C, while the ASME code temperature limit for a material like Alloy 800H is much lower, 760°C. Therefore, the thermal response of all metallic internals due to reactor transients is the key system phenomena of importance where reactivity and fluid flow can play important roles. It should be noted that the figure of merit for overcooling transients has switched to the flibe temperature due to the concerns of freezing the salts as opposed to alloy performance at lower temperatures.

4.3 System Scaling Approach

The global scaling analysis developed for the AHTR is based primarily on work by Wulff and Rohatgi [87], Wulff [80, 85] and Zuber et al. [53, 90]. Here the interest is in developing the similarity criteria at the global level by which the dynamic interactions between the AHTR components are studied. Scaling a system at the global level is fundamentally based on integral methods where the governing transport equations are converted from partial to ordinary differential equations using modeling simplifications [85]. What one loses in terms of local spatial distribution information is replaced with simplified closure relationships, making it tractable to predict and understand the overall system response. The momentum balance has been decoupled from the mass and energy conservation equations and fluid velocities are assumed to be much smaller than the speed of sound. The process for determining the global momentum balance is discussed in more detail in the following section.

4.3.1 Analogy with Electrical Circuits

There is a strong analogy between the treatment of fluid flow loops and electrical circuits. In pressurized water reactors, pressurized vessels respond to an addition or a removal of energy by changes in pressure and temperature where these vessels can be treated as both mechanically and thermally compliant [85]. The AHTR, however, operates near atmospheric pressure with little changes in pressure and are therefore only considered thermally compliant capacitances. Therefore, the mass and energy balances for the fluid can be used to determine the component thermal compliance within the system. A similar analogy exists between the fluid inertia in the interconnecting channels and inductances. Additionally, the flow resistance due to form losses and friction can be treated similarly as electrical impedance in electrical circuits.

When dealing with a multi-loop circuit, an electrical engineer must utilize Kirchhoff's laws. The first law is a direct analogy to mass conservation in fluid mechanics where the charge must be conserved at each junction. Also known as the junction rule, the law states that the sum of the currents coming in to a junction is equal to the sum leaving the junction. For simple circuits, the junction rule is sufficient to describe circuit response. However in the case of multi-loop circuits, Kirchhoff's second law must also be utilized. This law, also known as the loop rule, says the sum of all the potential differences around a complete loop is equal to zero. Kirchhoff's second rule is used to write down loop equations for as many loops as it takes to include each branch at least once. To write down a loop equation, one chooses a starting point, and then walks around the loop in one direction until one gets back to the starting point. By analyzing the single loops in a multi-loop circuit with Kirchhoff's Loop Rule and the junctions with Kirchhoff's Junction Rule, one can obtain a system of coupled equations with several unknown variables.

There is a loop momentum balance written for every closed loop in the AHTR reactor system. The loop momentum balances are then combined into a vector equation of first-order ordinary differential equations for scaling as one single vector equation. The vector equation is the global momentum balance of the system. The loop momentum balance is derived by summing up the pressure differences across the segments of the loop where the contour integral of pressure gradient around every loop, $\oint dp$, equals the sum of the pump-induced pressure increases in that loop [87]. The summation eliminates all internal pressures which are scalars (analagous to voltages in electrical circuits) and more natural to eliminate than internal forces (which are vectors, involving fluid-to-structure interactions) [85, 86]. As noted by Wulff and Rohatgi [87], the key consequence of formulating the momentum balance of a single-phase fluid for a loop segment in terms of pressure difference, instead of resultant forces, and in terms of volume flowrate instead of the familiar velocity, is that one obtains the inertia per area squared ($\rho L/A$) instead of the familiar fluid mass (ρV). This is analagous to capacitance in an electrical circuit. The global momentum balance and it's resultant terms are discussed in Section 4.4.

4.3.2 Loop Descriptions for System Scaling

The overall performance of the loops described in Section 3.3.4 is the main focus of the proposed AHTR test reactor (ATR) in the experimental validation program (see Figure 4.1). In phase 2 and 3 of the transient, the flowpaths change direction where there is minimal circulation through the PCL. In this section, the momentum analogy to Kirchhoff's second law is utilized where a set of loops are determined. For the proposed ATR primary system illustrated in Figure 4.1, the PCL, SRL, and DBL loops ($\Omega_{a,1}, \Omega_{a,2}, \Omega_{a,3}$ respectively) consists of the following segments during the first phase of the transient (1, 4, 6, 5), (1, 3, 6, 5), and (2, 5, 1, 4). The primary system contains a total of 3 closed loops (N_L) with a total of 4 independent branch points (N_B) rendering ($N_L + N_B - 1 = 6$) linearly independent equations for the same number of transient volumetric flow rates at branch exits. For phase 2 and 3, the primary flow follows the DHX flowpath dominantly where heat removal from the IHX drops to zero and stably stratifies. Therefore, the PCL, SRL, and DBL loops ($\Omega_{b,1}, \Omega_{b,2}, \Omega_{b,3}$ respectively) contain the following segments during the latter two phases of the transient (1, 4, 6, 5), (1, 3, 6, 2), and (1, 4, 6, 2) as shown in Figure 4.1b.

Wulff [85, 86] describes in detail the approach for determining flow distributions in the loop system. For each closed loop in the system, a primary segment has been identified (indicated by red arrows in Figure 4) with a corresponding primary (with subscript pr) volumetric flow rate at the respective branch point for each accident phase. All of the other segments are considered secondary (with subscript sn) with their own respective secondary volumetric flow rates (black arrows). Primary segments for phase 1 are 1, 3, and 5 and secondary segments are 2, 4, and 6. Whereas for phases 2 and 3, the primary segments are 1, 3, and 2 and the secondary segments are 4, 5, and 6

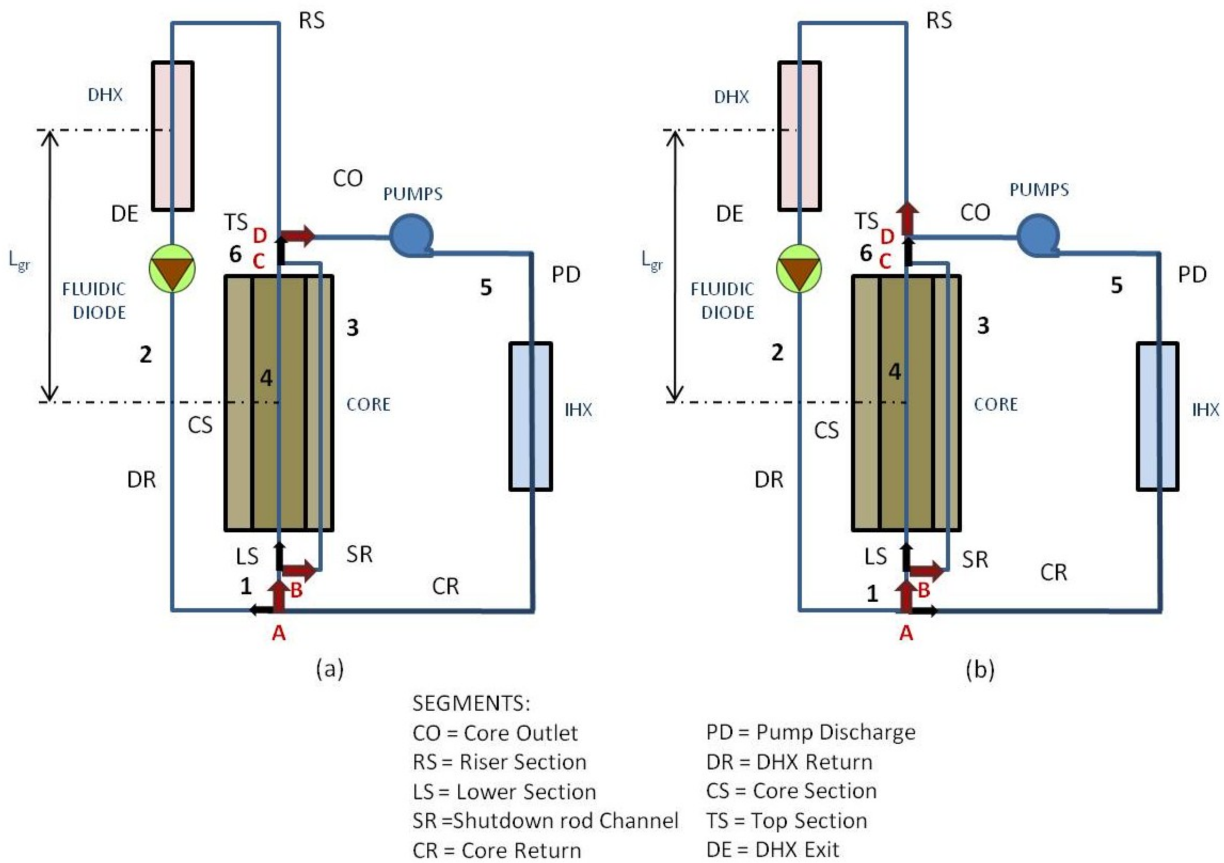

Figure 4.1: Simplified logic diagram illustrating the various flowpaths for the 16 MWth Test Reactor System during a LOFC transient before (a) and after (b) the natural circulation flowpath has been established.

4.4 Global Momentum Balance

For the purpose of this section, only the global momentum balance equation is considered and not the governing energy balance equations between the heated structures and the working fluid. Pressure disturbances in the primary system are assumed to propagate instantaneously and the very small density variations due to spatial pressure variations are neglected. The gradient of the pressure is therefore assumed to be zero in the mass and energy conservation equations.

$$\nabla p = 0 \tag{4.1}$$

For each closed loop of the AHTR primary system, one can write a loop momentum balance and then combine them into a vector equation of first-order ordinary differential equations for scaling as a single vector equation. The system momentum balance in compact vector notation was developed by Wulff [85]:

$$\boldsymbol{I} \cdot \frac{d\overrightarrow{W}}{dt} = \overrightarrow{G} + \triangle\overrightarrow{P}_{PP} - \left[\mathbf{R} \cdot \left(\mathbf{W^2}\right)\right] \cdot \boldsymbol{\Upsilon} \tag{4.2}$$

where $\boldsymbol{I}$ is the geometry-dependent, time invariant inertia matrix and $\overrightarrow{W}$ represents the mass flowrate. On the RHS, $\overrightarrow{G}$ and $\triangle\overrightarrow{P}_{PP}$ are the buoyancy and pressure difference vectors respectively where the latter is imposed by pumps or pressure vessels. The final term is made up of the impedance matrix, $\boldsymbol{R}$, the kinetic energy matrix, $\boldsymbol{W}^2$, and the identity matrix, $\boldsymbol{\Upsilon}$. Since the primary interest is in a simultaneous trip of both pumps, the pressure differences due to pumping power are equal to zero following the coastdown phase. In the case of a single pump trip for the prototype AHTR (ATR will only have one pump), the pumping power for the operational pump remaining must be accounted for in this term, however this is not the focus of this work.

$$\triangle\overrightarrow{P}_{PP} = 0$$

In the following subsections, each term of the system momentum balance is discussed in greater detail with respect to the AHTR.

4.4.1 Inertia Matrix

The LHS of the global momentum balance represents the product of the inertia matrix and the multi-dimensional vector of the flow rates which comes directly from the time-dependent storage term in the momentum balance,

$$\frac{dM_i}{dt} = \frac{d}{dt}\oint \phi \cdot \rho \frac{dz}{A} = \oint \frac{dz}{A}\frac{d\overrightarrow{W}}{dt} \tag{4.3}$$

The inertia matrix contains the inertia information for each segment between the independent branch points where each row represents. In order to determine the $N_L \times N_L$ global system inertia matrix for each phase, a specified admittance matrix characterizing the system topology [86] was developed. The entire process for determining the admittance matrix and ultimately the inertia matrix is discussed in Appendix A.

If one substitutes the inertial contribution from each segment in for $\boldsymbol{I}$, the two three-dimensional inertia matrices derived in Appendix A (Equations A.9 and A.10) become ,

$$\boldsymbol{I}_a = \begin{bmatrix} \left(\frac{L}{A}\right)_{LS} + \left(\frac{L}{A}\right)_{CS} + \left(\frac{L}{A}\right)_{TS} & -\left(\frac{L}{A}\right)_{CS} & \left(\frac{L}{A}\right)_{CO+PD+PR} \\ \left(\frac{L}{A}\right)_{LS} + \left(\frac{L}{A}\right)_{TS} & \left(\frac{L}{A}\right)_{SR} & \left(\frac{L}{A}\right)_{CO+PD+PR} \\ \left(\frac{L}{A}\right)_{LS} - \left(\frac{L}{A}\right)_{DHR} + \left(\frac{L}{A}\right)_{CS} & -\left(\frac{L}{A}\right)_{CS} & \left(\frac{L}{A}\right)_{CO+PD+PR} + \left(\frac{L}{A}\right)_{DHR} \end{bmatrix} \tag{4.4}$$

$$\boldsymbol{I}_b = \begin{bmatrix} \left(\frac{L}{A}\right)_{LS} + \left(\frac{L}{A}\right)_{CS} - \left(\frac{L}{A}\right)_{CO+PD+CR} + \left(\frac{L}{A}\right)_{CS} & 0 & \left(\frac{L}{A}\right)_{CO+PD+PR} \\ \left(\frac{L}{A}\right)_{LS} + \left(\frac{L}{A}\right)_{TS} & \left(\frac{L}{A}\right)_{SR} & \left(\frac{L}{A}\right)_{DHR} \\ \left(\frac{L}{A}\right)_{LS} + \left(\frac{L}{A}\right)_{CS} + \left(\frac{L}{A}\right)_{TS} & 0 & \left(\frac{L}{A}\right)_{DHR} \end{bmatrix} \tag{4.5}$$

where the local values for each section have been included ($I_{RS+DE+DR} = I_{DHR}$). Numerical values for the inertia matrices can be found in Appendix A. It is important to note that the actual inertia matrix for the final design of the AHTR will have considerably more terms due to the increase in the actual number of loops that exist in a detailed design.

4.4.2 Flow Rate Vector

The flow rate vector for the two different systems under consideration is made up of all the primary segment mass flow rates for each respective loop. Since the ATR is still in conceptual design, the exact number and types of loops will impact this term. The flow rate vectors can be written as,

$$\vec{W}_a = \begin{pmatrix} W_{LS} & W_{SR} & W_{CO+PD+CR} \end{pmatrix}^T \tag{4.6}$$

$$\vec{W}_b = \begin{pmatrix} W_{LS} & W_{SR} & W_{RS+DE+DR} \end{pmatrix}^T \tag{4.7}$$

4.4.3 Buoyancy Vector

The buoyancy vector represents the pressure differences caused by gravitational forces in the respective closed loops. During power operation, the pressure differences caused by the pumping forces dominate over the contribution from the buoyancy vector. However, following a pump trip and shutdown rod insertion, flow in the primary loop is driven by the thermal driving head generated by the temperature difference between the DHX and core region and height difference. The buoyancy vector for the two phase types under investigation are below,

$$\vec{G}_a = \begin{bmatrix} 0 \\ \overrightarrow{g} \cdot \oint_{SRL} \hat{k}\rho dz \\ \overrightarrow{g} \cdot \oint_{DBL} \hat{k}\rho dz \end{bmatrix}, \quad \vec{G}_b = \begin{bmatrix} 0 \\ \overrightarrow{g} \cdot \oint_{SRL} \hat{k}\rho dz \\ \overrightarrow{g} \cdot \oint_{DBL} \hat{k}\rho dz \end{bmatrix} \tag{4.8}$$

Each row in the buoyancy vector represents the gravity-driven flow contribution from the PCL, SRL and DBL respectively and is defined further below (applicable for both loop configurations). More information on the buoyancy term can be found in [85].

$$\overrightarrow{g} \cdot \oint_{SRL} \hat{k}\rho dz = \int_{CS} \hat{k}\rho dz - \int_{SR} \hat{k}\rho dz \tag{4.9}$$

$$\overrightarrow{g} \cdot \oint_{DBL} \hat{k}\rho dz = \sum_{j \epsilon DBL} \int_{j} \hat{k}\rho dz \tag{4.10}$$

4.4.4 Impedance and Directed Kinetic Energy Matrix

In this section, the impedance, or flow resistance, and directed kinetic energy matrices are derived for the global momentum balance corresponding to the friction and form losses for all sections making up each respective segment. For certain parts of the transient, the flow in the primary loop is expected to be in the laminar regime during passive decay heat removal therefore making the losses due to friction proportional to the mass flow rate (unlike losses in the turbulent regime). Therefore, the total losses due to friction and form losses can be written as

$$\sum_{i \epsilon j} \left(\Delta p_{fr} + \Delta p_{form}\right)_i = \boldsymbol{R_{kj}} \left(\boldsymbol{W}|\boldsymbol{W^n}|\right)_{\boldsymbol{j}} \tag{4.11}$$

where the irreversible dissipation is determined in terms of the resistance of each component (characterized by i) in each loop segment (indicated by j) between branch points of a loop (indicated by k). For each component evaluated, frictional losses in the laminar regime are distinguished by setting the exponent of the second term in the directed kinetic energy vector, n, to zero instead of one for flow in the turbulent regime. The impedance matrices for the two phase categories are written below.

$$\boldsymbol{R_a} = \frac{1}{2\rho_0 A_{a,i}^2} \begin{bmatrix} R_{LS} & 0 & R_{CO+PD+CR} & 0 & R_{CS} & R_{TS} \\ R_{LS} & R_{SR} & R_{CO+PD+CR} & 0 & 0 & R_{TS} \\ 0 & 0 & R_{CO+PD+CR} & R_{RS+DE+DR} & R_{CS} & 0 \end{bmatrix} \tag{4.12}$$

$$\boldsymbol{R_b} = \frac{1}{2\rho_0 A_{a,i}^2} \begin{bmatrix} R_{LS} & 0 & 0 & R_{CS} & R_{CO+PD+CR} & R_{TS} \\ R_{LS} & R_{SR} & R_{RS+DE+DR} & 0 & 0 & R_{TS} \\ R_{LS} & 0 & R_{RS+DE+DR} & R_{CS} & 0 & R_{TS} \end{bmatrix} \tag{4.13}$$

Where R_{AB} is a single loss coefficient representing the flow resistances of all components in a loop segment (i.e. CO, PD etc...),

$$R_{AB} = \sum_{ij\epsilon AB} \frac{K_i + f_j \frac{L}{d_{h,j}}}{a_j^2} \tag{4.14}$$

The six-dimensional vector of direct kinetic energies for the two respective phase categories are written below where $W_{PDL} = W_{CO+PD+CR}$,

$$\overrightarrow{W}_a = \begin{bmatrix} W_{LS} & W_{SR} & W_{PDL}|W_{PDL}| & W_{LS} + W_{PDL} & W_{LS} + W_{SR} & W_{LS} \end{bmatrix}^T \tag{4.15}$$

$$\overrightarrow{W}_b = \begin{bmatrix} W_{LS} & W_{SR} & W_{RS+DE+DR} & W_{LS} & W_{LS} + W_{RS+DE+DR} & W_{LS} \end{bmatrix}^T \tag{4.16}$$

4.5 Normalization of Governing Loop Momentum Equations

The governing loop momentum balance is next normalized using the normalization principles outlined by Zuber et al. [53] and Wulff et al. [87, 80]. Each variable, $\phi(t)$, in the momentum balance is reduced by its predicted minimum value, ϕ_{min}, divided by its expected range, $\phi_{max} - \phi_{min}$, yielding the normalized variable measuring the fractional value of ϕ (between 0 and 1),

$$\phi^* = \frac{\phi - \phi_{min}}{\phi_{max} - \phi_{min}} \tag{4.17}$$

In the case of the LOFC where most reference parameters are decreasing monotonically as the power level drops, ϕ_{max} is typically their initial value at the start of the transient. The reference parameters selected for this analysis were taken from RELAP5-3D simulations and are discussed further in Appendix A. Following this approach, each term in the momentum balance is normalized with respect to the main loop fluid residence time defined as $\tau = V_L/Q_L$. For the first phase of the transient, the reference time will be the fluid residence time in the PCL loop whereas for the last two phases the reference time will be the fluid residence time in the DBL. In the first case, the flow rate is imposed by the two main salt pumps whereas for the latter case the flow rate can be determined from the Richardson number that emerges from the steady-state momentum balance [41].

Starting with the governing loop momentum balance (Equation 4.2), the elements of the inertia, gravity, and flow resistance vectors are normalized with the reference parameters of the dominant loop such that the scaled and time-dependent element of the inertia matrix, I^*_{ji}, the scaled and time-dependent gravity force element, G^*_j, the scaled and time-dependent element of the impedance matrix, P^*_{jk}, and the scaled and time-dependent element, E^*_j, of the directed kinetic energy vector are of order unity [87, 86]. Each term is defined further below,

$$M^*_j = (S_I I^*)_{ji}\,\phi^*_i,\; G^*_j = \hat{g}\cdot\oint_j \hat{k}\rho^*_m dz,\; P^*_{ji} = \frac{R_{ji}(t)}{R_{ji}(0)},\; E^*_{ji} = \frac{E_i\,(t)}{E_i\,(0)},\; I^*_{ji} = \frac{I_{ji}(t)}{I_{ji}(0)} \tag{4.18}$$

Starting from the left, the normalized momentum term consists of the non-dimensional inertia metric, S_I, that measures the distribution of inertia relative to the main loops identified in the previous section. By incorporating the respective loop average mixture densities into the inertia matrix, the primary mass flowrate values are replaced with their respective normalized primary volumetric flowrates. The gravity force element is a one-dimensional array containing the pressure differences due to gravitational forces associated with each loop with respect to the reference loop (i.e. PCL for phase a and DBL for phase b). The same normalization process is repeated for both the impedance and directed kinetic energy term. Just like the normalized inertia term, the remaining two normalized driving terms (i.e. gravity and impedance) contain metric terms that measure the distribution of gravity and flow resistance relative to the reference loop. These three metric terms are defined below [85] and are utilized in the next section for both scaling methods.

$$S_{I_{ji}} = \frac{(\phi_0)_j\,(I_0)_{ji}}{\sum\limits_{i \epsilon loop_{ref}} (\phi_0)_{ref}\,(I_0)_{ref,i}},\; S_{G_j} = \frac{[(\Delta H_{GR}\beta_T \triangle T_{GR})_0]_j}{(\triangle H_{GR}\beta_T \Delta T_{GR})_{ref}} \tag{4.19}$$

$$S_{P_{jk}} = \frac{\left(\frac{W_{j,0}}{W_{ref}}\right)^2 (R_0)_{jk}}{\sum\limits_{i \epsilon loop_{ref}} \left(\frac{W_{i,0}}{W_{ref}}\right)^2_i R_{ref,i}}$$

Here, the subscripts j, 0, and ref stand for j^{th}, initial value of that parameter, and reference or main loop respectively. As mentioned previously, the inertia metric measures the distribution of the inertia relative to the main loop where larger numerical values indicate a lower fluid response in that particular loop relative to the other elements in the metric. The gravitational metric indicates the overall importance of gravitational effects in the considered loop with respect to the reference loop. Finally, the impedance metric has a row associated with each loop and a column respectively for each segment of the loop. The impedance metric ultimately determines the flow distribution in the primary system as steady-state conditions are reached [87].

4.6 Scaling of Governing Loop Momentum Equations

In this section, integral scaling groups for CIET are determined using both Causative Process Scaling Analysis (CPSA) and Fractional Scaling Analysis (FSA) methods. As mentioned previously, the focus of this work is on the momentum balance however a complete global scaling analysis must consider the global energy balance between the heated structures and the fluid. The system-specific parameters used in calculating each scaling group are presented in Appendix A.

4.6.1 Causative Process Scaling Analysis of the Global Loop Momentum Balance

In the first section the governing momentum balance equation is scaled using CSPA method. The CSPA method scales the governing transport equation of interest by the causative or dominant driving term for the phase of interest. In the case of a LOFC, the causative process is the gravitational forces generated by temperature and elevation differences between the heated and cooled sections. Following the scaling principles outlined in the previous section and by Wulff [85, 87], the momentum balance for single-phase natural circulation reduces to the form below,

$$\Pi_{IN} \cdot \frac{dM_j^*}{dt^*} = \left(S_G G^*\right)_j - \Pi_{RS} \left(S_P P^*\right)_{jk} E_k^* \tag{4.20}$$

where the subscripts IN and RS refer to inertial and resistance respectively (no pumping terms). The product of the inertia matrix and the flow rate vector (LHS of Equation 4.2) represent the momentum capacitance term, whereas the RHS of the same equation represents the driving and retarding contributions to the momentum flux. The first non-dimensional group that emerges is the *global system inertia* group which represents the ratio of global inertial to gravitational forces,

$$\Pi_{IN} = \frac{\phi_{ref}}{t_{ref} g \Delta H_{GR} \left(\beta_T \rho \Delta T_0\right)_0} \sum_{i \epsilon loop_{ref}} \frac{(\phi_0)_i}{\phi_{ref}} \left(I_0\right)_i \tag{4.21}$$

$$\Delta T_0 = \frac{\dot{Q}}{\left(c_{p,l}\right)_0 W_{ref}}$$

The second scaling group that emerges is the *global system impedance* group which is the ratio of global flow resistance over gravity forces resulting in the system impedance for natural circulation,

$$\Pi_{RS} = \frac{W_{ref}^2}{g \Delta H_{GR} \left(\beta_T \rho \Delta T\right)_0} \sum_{i \epsilon loop_{ref}} \left[\frac{(W_0)_i}{W_{ref}}\right]^2 \left(R_0\right)_{ref,i} \tag{4.22}$$

Scaling Group Definition	Π-group Symbol	PB-AHTR (Phase a)	PB-AHTR (Phase b)
System Inertia	Π_{IN}	9×10^{-3}	N/A
System Impedance	Π_{RS}	3.9	1.1
System Gravity (reference)	Π_{GR}	1	1

Table 4.1: Values for Π-groups developed using the causative process method

Numerical values for each scaling group are presented below in Table 4.1. In the first row of Table 4.1, values for the global system inertia groups are given. As can be seen, the inertial contribution is very small with respect to the gravitational term during the initial phase of the LOFC. As the system reaches quasi-steady equilibrium, the inertial contribution becomes negligibly small and the global system inertia scaling group is no longer applicable. Since the each driving term is divided through by the causative process term (gravity-driven), the system gravity scaling groups are unity for both phases. Finally, numerical values for the global system impedance scaling group are provided in the third row. The results for each phase show that the impedance forces are not initially balanced by the driving gravitational forces at the beginning of the transient following the pump trip. As expected, this scaling group decreases in value as the transient approaches quasi-steady conditions in the later stage of the transient.

4.6.2 Fractional Scaling Analysis of the Global Loop Momentum Balance

In this section the governing momentum balance equation is scaled using the FSA method where the each term is divided through by the time-dependent inertial term instead of the causative process term. Therefore, the two fractional scaling groups that emerge are the global fractional impedance and the global fractional gravitational groups.

$$\Pi_{RS,F} = \frac{W_{ref}^2 \sum\limits_{i \epsilon loop_{ref}} \left[\frac{(W_0)_i}{W_{ref}}\right]^2 (R_0)_{ref,i}}{\phi_{ref} \sum\limits_{i \epsilon loop_{ref}} \frac{(\phi_0)_i}{\phi_{ref}} (I_0)_i} \tag{4.23}$$

$$\Pi_{GR,F} = \frac{g\Delta H_{GR} \left(\beta_T \rho \Delta T\right)_0}{\phi_{ref} \sum\limits_{i \epsilon loop_{ref}} \frac{(\phi_0)_i}{\phi_{ref}} (I_0)_i} \tag{4.24}$$

The first group can be determined by dividing the global system impedance group by the global system inertia group (both in Table 4.1). The global factional gravitational group can be determined by just taking the inverse of the global system inertia group. As discussed in the previous section, the time-dependent inertial term becomes negligibly small during the later stages of the transient as quasi-steady conditions are reached.

Therefore, fractional scaling groups are only presented for the time-dependent phase of the transient.

Scaling Group Definition	Π-group Symbol	PB-AHTR (Phase a)
System Impedance	$\Pi_{RS,f}$	428.9
System Gravity	$\Pi_{GR,f}$	111.1
System Inerta (reference)	$\Pi_{IN,f}$	1

Table 4.2: Values for Π-groups developed using the fractional scaling analysis method

Numerical values for each group can be found in Table 4.2. Since the inertial contribution was deemed to be very small, the magnitude of each fractional scaling group is larger than the respective causative process scaling groups in Table 4.2. As a result, the fractional scaling groups show that the system will adjust quickly to any changes in the loops flow resistance. This indicates that the primary system will in fact respond very quickly to the change in flow directions as both pumps are tripped simultaneously.

Chapter 5

Physical Similitude at the Subsystem Level

5.1 Subsystem Response of the AHTR

The AHTR implements a novel buoyant shutdown rod design for passive reactivity control. In this section, the similarity criteria for a buoyantly-driven shutdown rod in a liquid salt reactor system are given. As discussed in Chapter 2, scaling at the component level provides important insights into the local forces acting on the component but yields no insights into the boundary conditions that provide the driving force for the dynamic response of the component. The shutdown rod system is considered a subsystem and not a component due to the fact that there is a direct coupling between the core neutronic response which impacts the thermal-fluid exchange in the reactor primary loop ultimately driving the boundary conditions in the shutdown rod channel. In other words, there is a direct coupling between the core reactivity control and the dynamic response of the shutdown rod itself. Due to the exploratory nature of this concept, the first step in assessing the overall viability of the shutdown rod design is to decouple the multi-physics nature of the problem and focus initially on the thermal-fluid phenomenology.

5.1.1 Reactivity Control of the AHTR

In the AHTR, reactivity is controlled by the reactor control system (RCS) during normal or expected operation. As required by general design criterion 26 in Appendix A in 10CFR Part 50, the AHTR is required to have two independent reactivity control systems with different design principles.

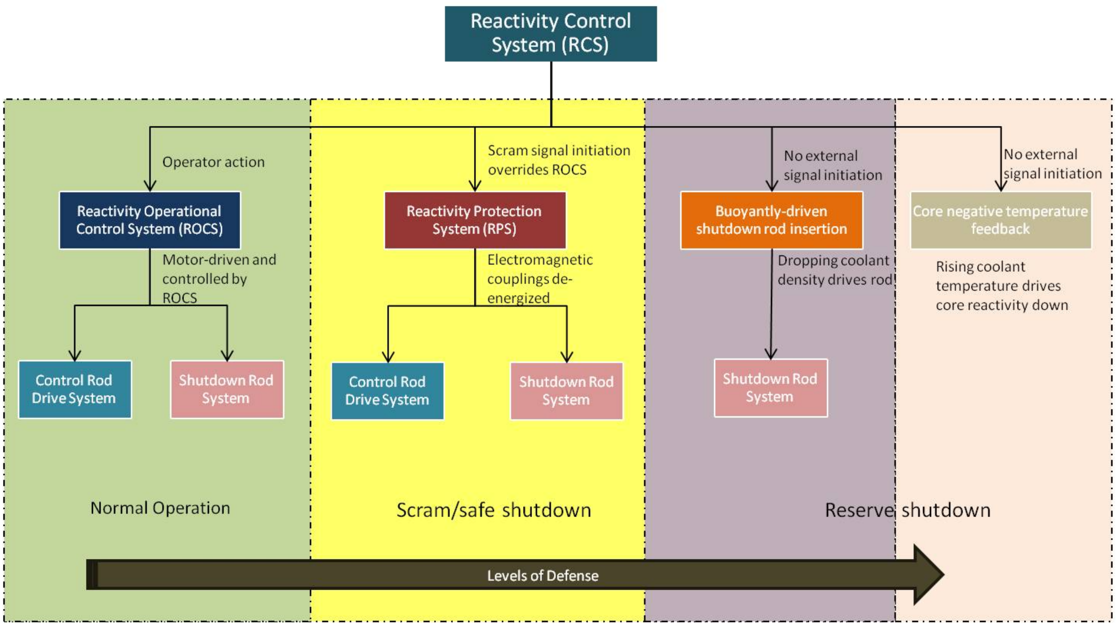

Figure 5.1: Levels of Defense for Reactivity Control in the AHTR from Normal Operation to Reserve Shutdown.

The AHTR has the following reactivity control methods which are illustrated in Figure 5.1, (1) normal shutdown by forced insertion of 6 shutdown rods; (2) reserve shutdown by insertion of 32 control rods; (3) reserve shutdown by passively driven buoyancy-activated insertion of the 6 shutdown rods; and (4) shutdown by core negative temperature feedback. Plan and elevation views of the AHTR depicting the locations of the control and shutdown safety rods can be found in Appendix C (Figs. C.1 and C.2 respectively). Following a scram signal or other shutdown signal, the shutdown rods and control rods are inserted via gravity by a heavy control rod actuator located above the rod, when the power is cut to the magnetic latches holding the actuators. For reserve shutdown, the shutdown rods will also insert passively due to negative buoyancy resulting from the rise of coolant temperature. The baseline AHTR design has six buoyant shutdown rods that sink into the reactor core if the coolant temperature exceeds normal levels. The shutdown rods are located in 19.8-cm diameter channels in six of the seven hexagonal Pebble Channel Assemblies (PCA) that comprise the reference AHTR reactor core (see Chapter 2 for a more detailed description). Each of the shutdown rods is designed to be neutrally buoyant at a flibe salt density corresponding to a flibe temperature of 615°C ± 5°C, taking into account all sources of uncertainty in the safety rod buoyancy (mass of the rod, volume of the rod, entrained gas bubbles on rod surfaces, flibe density, and other phenomena that would be identified by a detailed safety rod PIRT). The geometry that maximizes the rod drop velocity is a cylinder, which provides the minimum surface area to volume ratio. To maximize reactivity worth, however, the proposed shutdown rod geometry consists of crucifix section in the center with two cylindrical sections at the ends (see Figure 5.2).

Under normal steady-state forced circulation operation, a purge flow is metered into the bottom of each shutdown channel by a fluidic diode. The purge flow comes from the core inlet plenum at the bottom of the core, at the core inlet temperature $T_{c,in} = 600°\text{C}$. The purge flow results in an average upward coolant flow velocity in the channel uco of approximately 0.2 m/s. The purge flow is metered by a small fluidic diode, so that reverse flow after the primary pumps shut down has low flow resistance. The insertion of the shutdown rod elements provides negative temperature feedback in order to augment the negative feedback already provided by the negative coolant and fuel temperature reactivity coefficients [14]. Insertion of the shutdown rods occurs due to buoyancy forces generated by the difference between the density of the control element and the reactor coolant during an unprotected reactor transient. A heavy metallic driver element is suspended by a magnetic latch system above each shutdown rod and is not physically attached to the shutdown rod. In the event of a reactor scram signal, the electromagnetic coupling holding the drive elements are de-energized thus causing the elements to drive the shutdown rods into the active core region via gravity. If this active insertion mechanism does fail to operate, buoyancy forces cause the shutdown rods to inert anyhow.

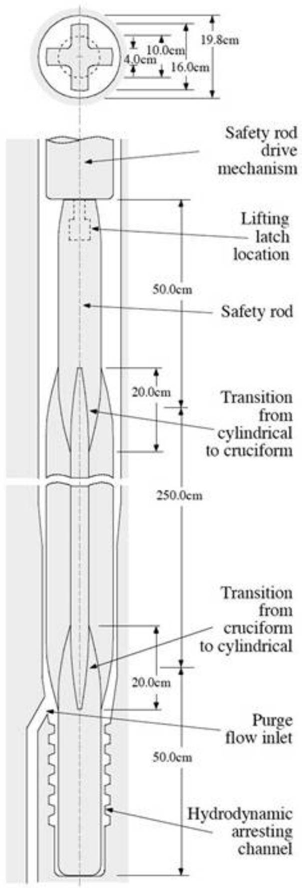

Figure 5.2: PB-AHTR shutdown rod geometry and hydrodynamic arresting channel.

5.2 Scenario Description and Figure of Merit

One of the more challenging events for the AHTR is a loss of heat sink (LOHS) transient without scram, where the IHX heat removal is interrupted but the primary pumps continue to operate and transfer fission power from the core to primary loop structures. This would also be a very severe transient for a MHR, since if forced circulation of the primary coolant continues without scram after loss of heat removal, the shutdown of an MHR on negative fuel temperature feedback would drive primary loop components and the pressure boundary to very high temperatures. The ATHR reaches a lower peak temperature than a MHR because it also has negative coolant temperature feedback. The goal in the design of the buoyant shutdown rod system is to further reduce this peak temperature under a LOHS transient without scram, as well as for LOFC without scram. Therefore the figure of merit for a LOHS is the same as the LOFC where the peak metallic internal temperature is the main parameter of interest. However, one key difference is overcooling transients are not of concern for a LOHS.

5.3 Technology Demonstration Approach

Consistent with the AHTR phased experimental validation program discussed in Chapter 2 (see Figure 2.3), the experimental testing of the shutdown rod performance must follow a similar trajectory starting from proof-of-principle all the way to confirmatory experimental work. Key experimental validation program objectives for the shutdown rod during the Viability Phase are illustrated in Figure 5.3. For the purpose of this dissertation, the scope of work presented in this chapter focuses primarily on the first two objectives relating to proof-of-principle and systems analysis. In Appendix B, a detailed description of a reduced–scale experiment for validating the rod performance is discussed and results are presented at the end of this section. Additionally, an analytical model used to predict the dynamic response of the rod as a function of density history is presented. The purpose of the next section is to derive the similarity criteria for this experiment with respect to the shutdown rod and the channel.

5.4 Similarity Criteria for the Buoyant Shutdown Rod System

In order to determine the similarity criteria for the shutdown rod, priorities for which non-dimensional parameters must be preserved has to be established. Similarity criteria are typically established using dimensional analysis or similarity theory. Both methods are not exclusive but rather utilize different approaches to reach similar conclusions. In the case of the shutdown rod, dimensional analysis was used where the key forces acting on the rod must be first examined.

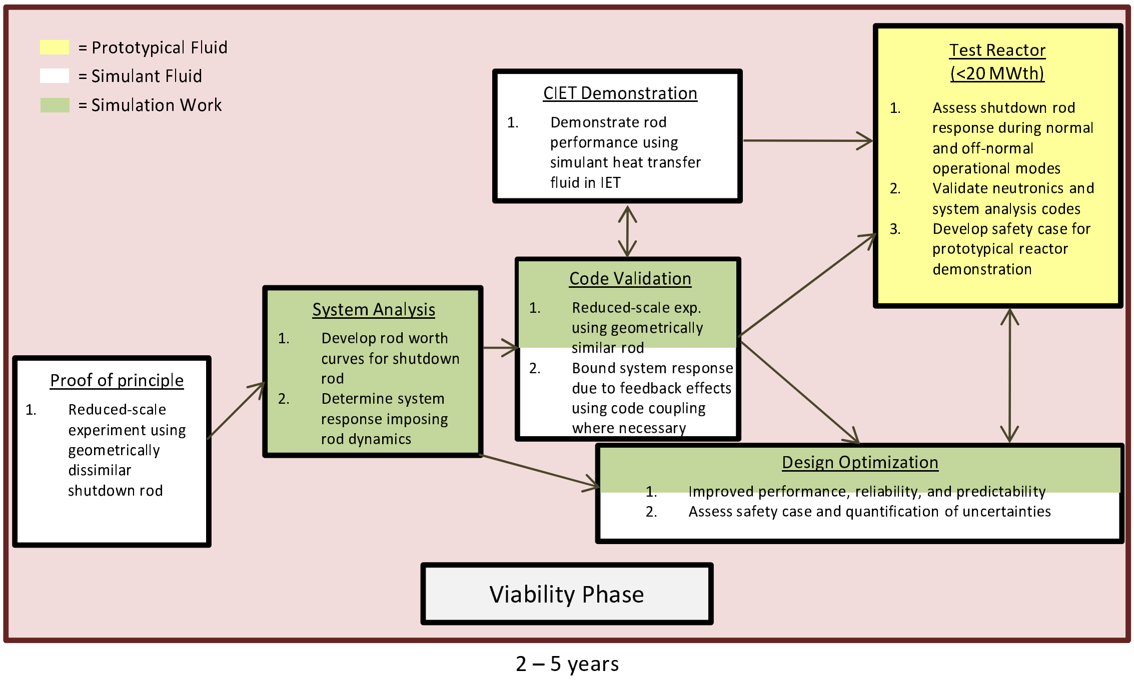

Figure 5.3: Experimental validation program using both simulant and prototypical working fluids of AHTR buoyantly-driven shutdown rod concept.

The buoyant rod can be modeled as an immersed body being subjected to drag and buoyancy forces. Therefore, a correctly scaled model experiment must match drag, inertial, gravitational forces acting on the prototypical rod in order to ensure physical similitude. The three non-dimensional parameters that are important to preserve include the Froude number, Reynolds number, and drag coefficient.

$$\Pi_{Fr} = \frac{u}{\sqrt{g'h}}, \quad \Pi_{Re} = \frac{uL}{\nu}, \quad \Pi_{c_d} = \frac{2F_d}{\rho u^2 A} \tag{5.1}$$

Bardet [28] showed that Reynolds and Froude numbers can simultaneously be preserved for prototypical conditions (Flibe at 650°C) using room temperature water as a simulant fluid at a reduced length scale ($L_r = L_m/L_p = 0.40$). The third non-dimensional parameter of interest is the drag coefficient which is preserved as long as geometric similarity and surface roughness are preserved between the prototype rod and the model rod. As shown in Figure 5.3 and discussed in Appendix B, the proof-of-principle objective involves a reduced-scale experiment using a geometrically dissimilar model shutdown rod where the drag coefficient will differ from the prototypical shutdown rod (see Figure 5.2). This distortion between model and prototype is of lesser concern since the drag coefficient is an empirically measured quantity and will not impact the fundamental physics captured in the predictive model.

Temperature (°C) in AHTR	Density ($kg \cdot m^{-3}$)	Specific Gravity in PRISM	Sugar water concentration (WT %)
600	1987.0	1.026	6.93
615	1980.0	1.023	5.98
704	1936.2	1.000	0

Table 5.1: AHTR and PRISM shutdown rod channel operating conditions.

Determining the similarity criteria for the shutdown rod channel requires establishing the correct boundary conditions from the prototypical system to model system. As discussed in the first section of this chapter, there is a direct coupling between the core neutronic, system, and shutdown rod responses that can't ultimately be ignored. However for proof-of-principle demonstration, this coupling can be initially ignored in order to assess the viability of the concept. Once the dynamic response of the rod due to density changes in the channel can be assessed with confidence, the coupled response of the core and shutdown rod can be determined.

Since the insertion of the shutdown rod occurs due to a change in density in the fluid, sugar water diluted by water can be used to simulate this density transition with minimal distortion where maintaining the correct specific gravity ratio is of dominant interest. During an LOHS, the actual density history in the prototypical AHTR shutdown rod channel is determined by the system response. During normal operation, fluid enters the shutdown rod channel at the same temperature as the core inlet (600°C) at a reduced flowrate. Since the shutdown rod channel is separate from the pebble flow channels, there is minimal heat transfer to the fluid and the fluid exits the shutdown rod channel at the same temperature where it mixes with coolant exiting the core (704°C). During a LOHS, the system's ability to reject heat has been compromised and therefore the core inlet temperature will ultimately thermally equilibrate and reach the core outlet temperature. The rate at which the system thermally stabilizes is a strong function of the mechanism by which the heat sink is compromised in addition to the fluid residence times from the heat sink to the core. In order to demonstrate proof-of-principle, it is initially assumed that that this transition occurs instantaneously and presents a favorably best-case scenario. Therefore, the similarity criterion for a geometrically similar channel is the ratio of inlet and outlet fluid specific gravities must be matched. Numerical values for the corresponding specific gravity ratios as well as sugar concentration by weight percent are given in Table 5.1.

$$\frac{\Pi_{\gamma_r,m}}{\Pi_{\gamma_r,p}} = \frac{\rho_{o,m} \cdot \rho_{i,p}}{\rho_{o,p} \cdot \rho_{i,m}} = 1 \tag{5.2}$$

5.5 Results from Reduced-scale Experiment

An integral effects test was run two times successfully to assess the performance of the passive shutdown rod concept. Each test involved a rapid step-change in the fluid density which is achieved by switching open the fresh water valve while simultaneously closing the sugar water valve. The PB-AHTR inlet temperature (i.e. the flow that is metered into the shutdown rod channel) will eventually reach the outlet flow temperature as the heat sink is compromised. In the event of a beyond design basis event, it was conservatively assumed that the channel inlet temperature increases instantaneously. The true evolution of the density or temperature of the core inlet is being further investigated using RELAP5-3D. Additionally, the effects of axial mixing in the channel will be strongest under these conditions and provide a conservative bounding case for the model comparison. Results from each trial are discussed in this section.

A successful trial is defined as a run where all data acquisition systems perform. Visual cues from all three camera locations were used to cross-check the fluid density history at the channel inlet. The mean channel velocity was independently checked using the rising water level and the high-speed camera during startup. The pre-prediction calculation was performed for an immediate step-change where there is no mixing from diffusion or combined flow from both streams (see Appendix B for details on pre-prediction model). Since a slight delay in closing off the primary tank yielded a more seamless transition in fluid densities, it was decided to rerun the pre-prediction with the actual density history. Results from each trial are presented below (Figure 5.4 and Figure 5.5). The rod location was independently verified using the photogate system, the high-speed camera (Figure 5.6) and the camera observing the jet region. The only difference between the two trials was the volumetric flowrate was reduced for the second trial. While the rotameter gives us general knowledge of the flowrate, the channel camera was used to measure the rise in the channel water level during startup for verification. In both cases, there appeared to be some slight axial mixing however the rod dropped rather rapidly once the surrounding fluid had dropped in density. Since the two flow paths are determined using simple valve actions, the in-situ density measurements become increasingly more important. The rod reaches the bottom of the channel at 29.40 and 28.87 seconds for trial 1 and 2 respectively. MCNP was used to determine the rod worth as a function of insertion position assuming all six rods are functioning. A prototypical rod insertion of 2.28 meters provides enough reactivity control to bring keff down to 0.95 in order to ensure a safe shutdown. Under model conditions, the rod reaches the same scaled point at 25.11 and 24.01 seconds for trials 1 and 2 respectively (indicated by a dashed red line in Figure 5.4 and Figure 5.5).

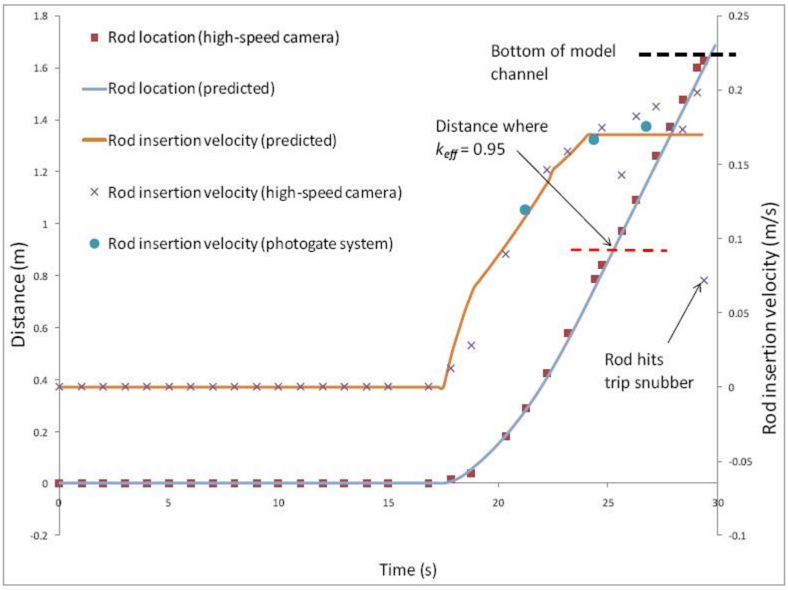

Figure 5.4: Predicted vs. experimental rod velocity and position values for trial 1. Rod location measurements were determined using the high-speed channel camera and the photogate system in both trials. The black dashed line indicates the location where the rod reaches the bottom of the channel.

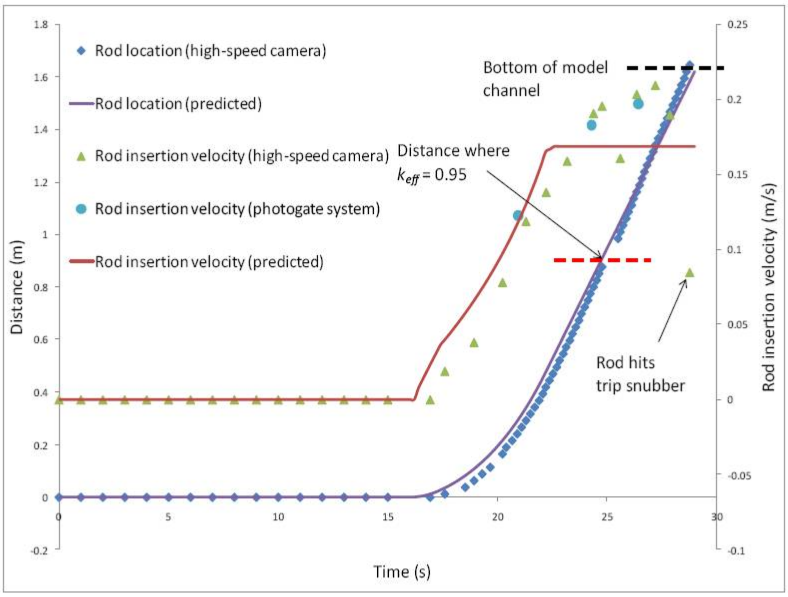

Figure 5.5: Predicted vs. experimental rod velocity and position values for trial 2.

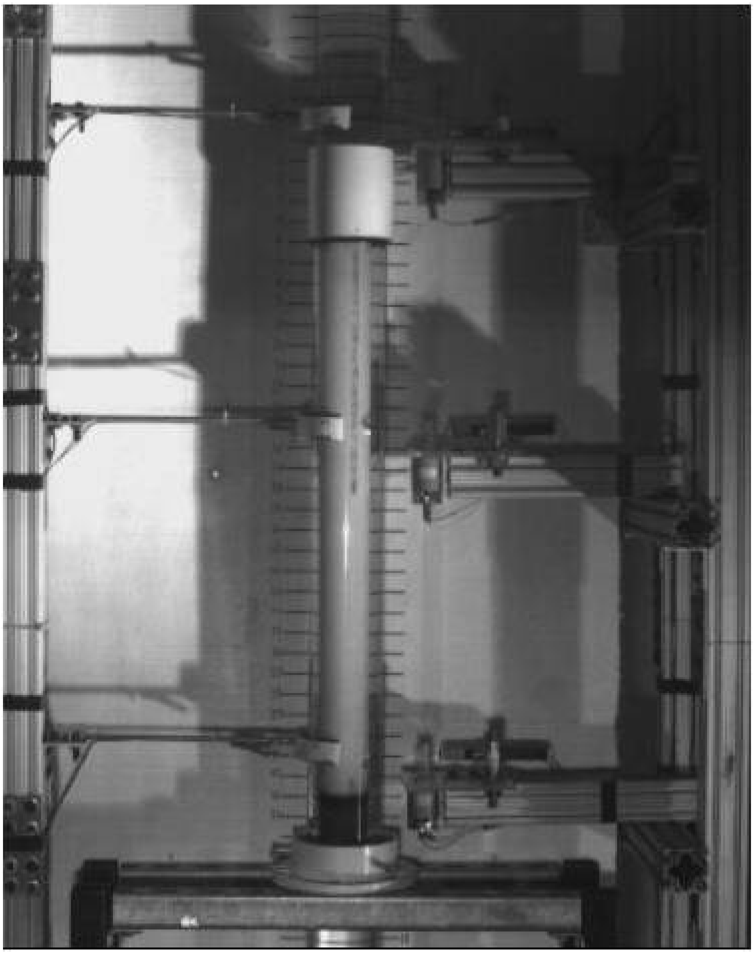

Figure 5.6: Frame from the channel-view high-speed camera used to determine rod location (note LED to left of the channel).

Using the shutdown rod worth curves, a preliminary system response evaluation was performed where the primary coolant inlet and outlet temperatures were compared with the case where the reactor shuts down on negative reactivity alone (see Figure 5.7). Using the aforementioned assumptions, initial results show a reduction in peak coolant temperature by approximately 40°C as compared with shutting down on negative reactivity alone. A big component of improving the performance of the shutdown rod includes minimizing the drag on the shutdown rod and decreasing the amount of time it takes for the inlet and outlet core temperatures to thermally equilibrate.

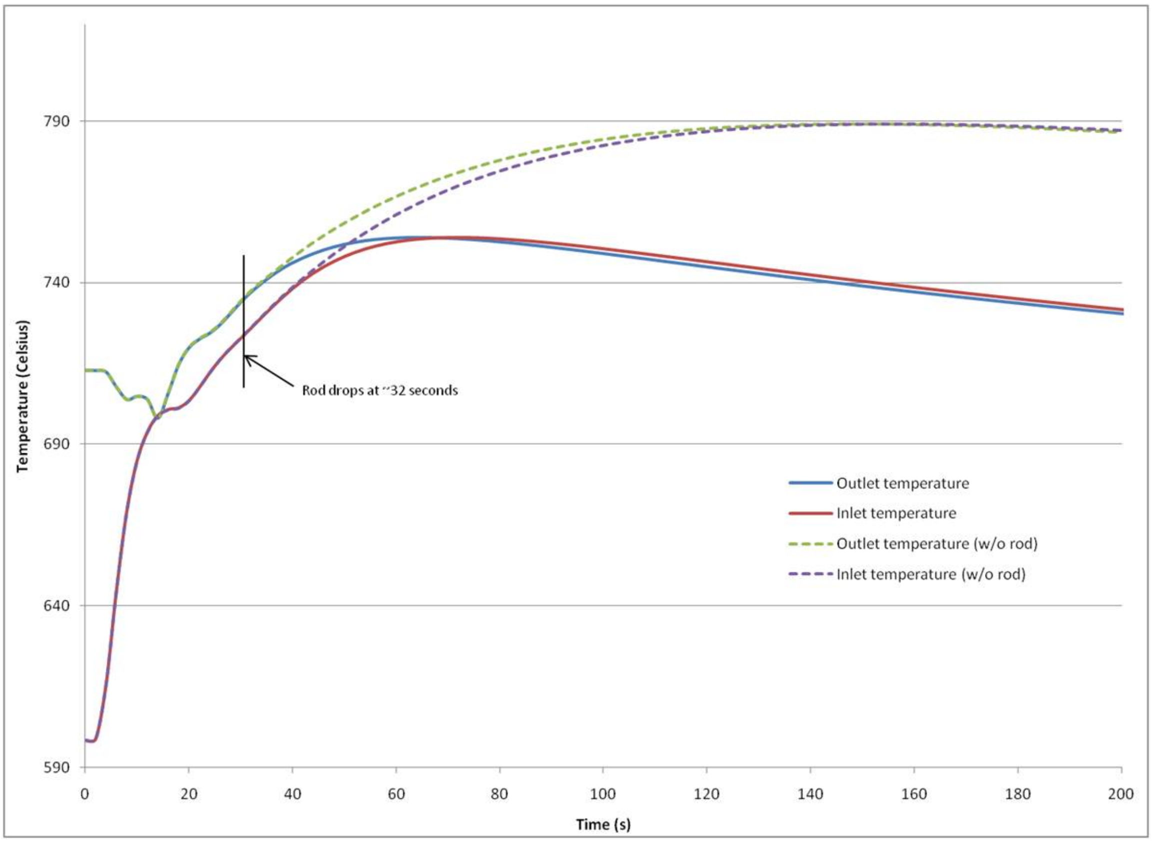

Figure 5.7: System response using RELAP5-3D during a LOFC where kinematic information of the shutdown rod was incorporated.

Chapter 6

Physical Similitude at the Component Level

6.1 Component Response of a Fluidic Diode

Fluidic diodes are one-way valves with no moving parts that are used in a wide variety of flow applications. Due to the passive nature of fluidic diodes, the reliability of fluidic diodes are considered higher than equivalent valves (i.e. check valves) and require little to no maintenance. The original patent for a fluidic diode comes from Nikola Tesla with his design of a *valvular* conduit [77] which was essentially a channel network made up of an open main duct and a set of side loop channels joining the duct at oblique angles. There are three general classifications of fluidic diodes: (1) scroll diode, (2) flow rectifier diodes, and (3) vortex diodes.

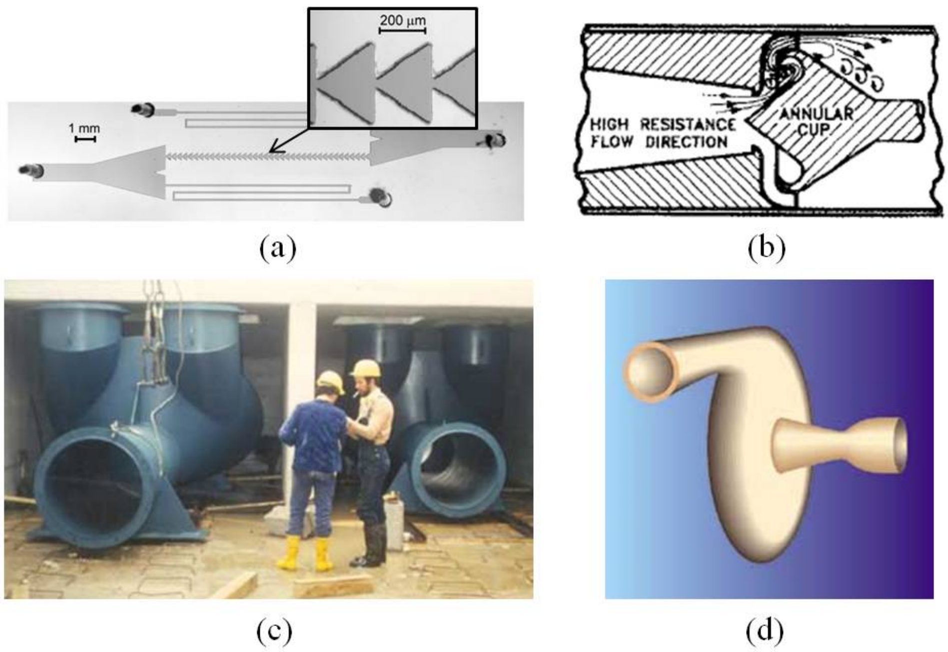

Figure 6.1: Fluidic diodes come in a range of sizes and perform a variety of functions. Diodes depicted: (a) flow rectifier diode for microfluidic applications, (b) scroll diode, (c) vortex diode amplifier for dam applications, and (d) generic vortex diode.

Fluidic diode performance is measured by a quantity called diodicity which, much like its electrical analogue, refers to the ratio of the flow resistance in the reverse direction over the forward direction. More specifically, the diodicity is the ratio of reverse flow pressure drop to the forward flow pressure drop for the same flow rate ($D = \Delta P_r/\Delta P_f$). The reverse and forward flowpaths refers to the undesired and desired direction of the flow respectively [2]. The vortex diode is considered to have the highest performance of the three classes of diodes with typical diodicity values of approximately 50 [26]. In the reverse direction, a vortex develops inside the device where high centrifugal forces create a high radial pressure gradient and thus a large pressure drop at low flow rate. In the forward direction, a radial flow distribution is set up inside the device where there is minimal flow resistance roughly equal to two 90 degree pipe bends. The scroll diode operates on a similar principle where typical diodicity values of 30 have been reported [26]. The fluid flow rectifier operates on a slightly different principle where flow seperation plays the dominant role for providing high flow resistance and has been reported to have lower diodicities than the other two types [26]. For the purpose of this dissertation, the vortex diode will be the focus of this chapter.

In this chapter, the reference fluidic diode for the AHTR is discussed in greater detail. As discussed in Chapters 1 and 3, component response is best understood using deductive logic where one starts with the physical processes and works towards the system response. Components such as pumps or valves can be decoupled from the integral response in order to assess their performance.The boundary conditions for both forward and reverse directions are discussed from the perspective of system response. Similarity criteria and results from a reduced-scale experiment (see Appendix C) are also presented.

6.1.1 Vortex Diode Description

The vortex diode (depicted in Figure 6.2) is made up of three parts: (1) tangential port, (2) vortex chamber, and (3) axial port. The reference vortex diode for this dissertation is fundamentally based off of work by Zobel [89] and a recently modified design by Kulkarni et al. [2, 1].

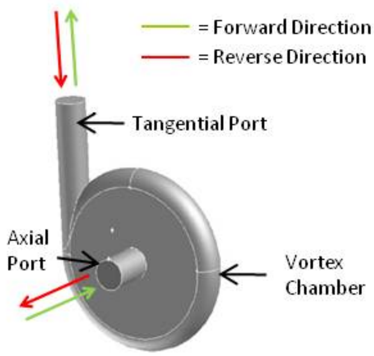

Figure 6.2: Schematic of vortex diode illustrating forward and reverse flow directions.

During normal operation in the AHTR, flow enters the tangential port for each fluidic diode from flow bypass lines exiting the inlet plenum (see Figure 3.11). Once the flow enters the vortex chamber of the diode, a confined vortical flow is established where the tangential velocity of the flow increases from the peripherary towards the center of the port. Classical studies in confined vortical flow by Wormley [83] and Stairmand [71] have shown that the flow can be divided into two regions: (1) a free vortex region and (2) a forced vortex region. As the swirl velocity increases from the periphery, the flow

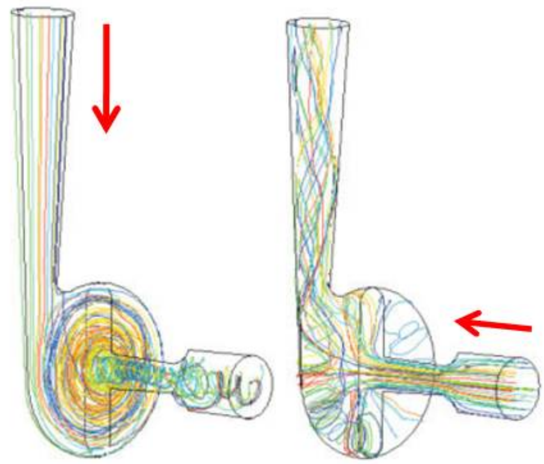

Figure 6.3: Typical pathlines for a vortex diode in the reverse (left) and forward (right) direction [1].

circulation is constant until a critical radius, r_c, where the vortical flow transitions to a forced vortex [2]. In the forced vortex region, the fluid rotates as a solid body where very little shear in the flow is present. Where the critical radius occurs in the vortex chamber is a strong function of the diode's geometry and flow boundary conditions. Figure 6.3 illustrates typical pathlines for a vortex diode.

6.2 Scenario and Phase Description

The prototypical conditions for the fluidic diode will fall within a range of nominal normal and abnormal flow conditions. Expected operational modes (i.e. startup, low power testing, etc..) and off-normal operational modes encompassing the entire design base envelope must be considered. Since the geometry of the diode is fixed, the Reynolds number is just a function of the mean channel velocity and fluid density and dynamic viscosity. Pressure drop measurements can be performed for a range of Reynolds numbers by adjusting the volumetric flowrate in the test loop. In the case of the PB-AHTR, each of the fluidic diodes accompanying the eight DHX units in the reactor core will be subjected to flow conditions over a range of Reynolds numbers in both directions. Ideally, the fluidic diode should allow less than 10% (preferably less than 5%) of the total core flow bypass through the DHX under power operation. Since the diode provides the primary flow resistance through the DHX bypass path, its flow resistance should be at least 10 to 20 times greater than the flow resistance provided by the core. In the following two sections, these flow regimes are discussed by flow orientation.

6.2.1 Range of Flow Conditions for Forward Direction Flowpath

During normal operation, the fluidic diode serves the function of limiting the amount of bypass flow that mixes with hot fluid exiting the core outlet plenum. When the reactor is started up from zero power, flow entering through the tangential port of the vortex diode will start at a lower Reynolds number regime and rise until full power is reached. For full power steady-state operation, the Reynolds number of the flow entering the diode is expected to be around 35,000. There are some postulated transients where the primary fluid temperature rises while still being directed through the high resistance flowpath. For example in the event of losing the ultimate heat sink, the fluid is still circulated through the primary loop however at an increasingly higher temperature. One can see from Table 6.1 below that as the primary loop reaches higher temperature, the drop in flibe viscosity drives the fluid to higher Reynolds numbers.

6.2.2 Range of Flow Conditions for Reverse Direction Flowpath

When the PB-AHTR loses the active ability to remove heat from the core, a natural circulation loop is set up by reversing the direction of the flow through the core fully engaging the set of DHX heat exchangers. Under this scenario, the flowpath of the primary loop is in the low resistance direction of the fluidic diode. It is desired to have the DHX remove decay heat with a similar or smaller temperature drop than the temperature drop for full power operation. Since decay heat will be a few percent of full power, the desired mass flow under natural circulation is similar to the desired bypass mass flow, and thus the Reynolds number will be similar for both directions. Much of the flow during this scenario is in the low Reynolds regime where the flow is fully laminar. Therefore it is expected that the required range of Reynolds number for analysis will be fully bounded by the Reynolds number regime required for the reverse flow case. Since the diodicity will be measured at each desired Reynolds number, the diode performance will be assessed for a range of Reynolds numbers up to 35,000.

6.3 Similarity Criteria for a Fluidic Diode

To design a scaled experiment demonstrating the prototypical performance of a fluidic diode in an AHTR, priorities for which non-dimensional parameters should be matched must be established. In order to determine the similarity criteria for a flow obstruction such as a fluidic diode, one must start with the governing momentum equation derived from NSE which can be written in its non-dimensional form as,

$$\vec{V}^* = \vec{V}/u, \quad P^* = \frac{P - P_\infty}{P_0 - P_\infty}, \quad t^* = \frac{t}{L/u}, \quad \vec{g}^* = \vec{g}/g, \quad \vec{\nabla}^* = L\vec{\nabla} \tag{6.1}$$

$$St \cdot \partial_{t^*}\vec{V}^* + \left(\vec{V}^* \cdot \vec{\nabla}^*\right) = -Eu \cdot \vec{\nabla}^* P^* + \frac{1}{Fr^2}\vec{g}^* + \frac{1}{Re}\vec{\nabla}^{*2}\vec{V}^* \tag{6.2}$$

where,

$$St = \frac{fL}{V}, \quad Eu = \frac{2\Delta P}{\rho V^2}, \quad Fr = \frac{V}{\sqrt{gL}}, \quad Re = \frac{\rho V L}{\mu} \tag{6.3}$$

The two key dimensionless parameters which must be matched are the Reynolds number and the Euler number. By matching the Reynolds number where the characteristic length is the diameter of the inlet port, the flow regime entering the fluidic diode in the model will match the flow regime in the prototype. The Euler number is critical in situations where pressure and inertia influence the flow.

Geometric and kinematic similarity conditions are easily met by uniformly scaling the design by the appropriate length scale and ensuring diode orientation and flow boundary conditions are similar to prototypical conditions. In order to maintain dynamic similarity, we are interested in matching Reynolds and Euler numbers between the prototype and the model experiment.

$$\frac{\Pi_{Re,m}}{\Pi_{Re,p}} = \frac{\Pi_{Eu,m}}{\Pi_{Eu,p}} = 1 \tag{6.4}$$

$$\left(\frac{\rho_m}{\rho_p}\right) \cdot \left(\frac{L_m}{L_p}\right) \cdot \left(\frac{V_m}{V_p}\right) \cdot \left(\frac{\mu_p}{\mu_m}\right) = \left(\frac{\Delta P_m}{\Delta P_p}\right) \cdot \left(\frac{\rho_p}{\rho_m}\right) \cdot \left(\frac{V_p}{V_m}\right)^2 = 1 \tag{6.5}$$

Solving for ratio between model and prototype (indicated by r) of the fluid velocity, Equation 6.5 can be rewritten as,

$$V_r = \left[\left(\frac{\rho_r^2}{\mu_r}\right) \cdot L_r\right]^{-1/3} \tag{6.6}$$

The first assumption in Equation 6.5 is that the pressure drop across the diode from inlet to outlet is the same for the model and the prototype. It is also important to note that the designer has substantial flexibility in performing highly similar scaled experiments for design and code validation. The term in the square bracket contains all the prototypical and model simulant fluid thermo-physical property relationships as well as an assumed length scale (Table 6.1). This also implies in practice that physical similarity can be met at even smaller length scales with higher flowrates. One major issue is whether the surface morphology (i.e. surface roughness) scales similarly with length scale. Therefore, experimental test sections should be fabricated to minimize surface roughness.

6.4 Results from Reduced-Scale Experiment

A reduced-scale experiment investigating the performance of vortex diodes for the AHTR was performed in the UC Berkeley Thermal-Hydraulics Laboratory (a detailed description of the experimental work can be found in Appendix C). Water was used as a

Thermophysical Property	Flibe	Water
Fluid density ($kg \cdot m^{-3}$)	1987.0 (600°C)	1000 (25°C)
	1962.5 (650°C	
	1913.7 (750°C)	
Fluid dynamic viscosity ($kg \cdot m^{-1} \cdot s^{-1}$)	8.56E-03 (600°C)	9.93E-04 (25°C)
	6.78E-03 (650°C)	
	4.56E-03 (750°C)	

Table 6.1: Thermophysical properties of prototypical and simulant working fluids.

simulant fluid where both Reynolds and Euler numbers were matched at a reduced length scale. The purpose of the experiment was to investigate the performance (diodicity) of the diode for three different chamber sizes defined by the diode aspect ratio relating the chamber diameter and height ($\alpha = D/h$). Additionally, the experiment investigated the impact of different axial port diameters on the diodicity of the diode. Results from these trials are presented in this section. In addition to measuring absolute diodicity values, it was important to assess how diodicity varied with Reynolds number. The range of Reynolds numbers evaluated were limited on the low end by the capability of the rotameter to measure small flowrates and on the high end due to the fact that the pressure head required for the flow rate to reach steady state was higher than the height of the tank.

The three major parameters varied in the experiment were the aspect ratio of the diode (α), the diameter of the axial port exit, and the height of the axial port. Results for the first case where the smallest diode ($\alpha = 6$) was tested using all three axial ports are shown in Figure 6.4. For the second case, the axial port with the nominal diameter was tested where the three diodes with varying aspect ratios were tested (Figure 6.5). For the third case, the experiment was run using the smallest diode (alpha = 6) for two different axial ports of differing heights and results are presented in Figure 6.6.

In looking through the results, some key observations can be drawn with respect to the optimal geometry for the diode. First, the measured diodicity values for all three diodes were appreciably lower than measured values reported in the literature. The maximum achievable diodicity was just below 11 which is significantly lower than reported values between 50-60 [26, 2]. There are several potential sources of uncertainty that could have contributed to this discrepancy including, but not limited to, the surface finish of the diodes, pressure measurement techniques, and non-optimal axial port geometries. Second, the diameter of the axial port did have an appreciable impact on the diodicity of the device. In Figure 6.4, it appears as if the nominal axial port (equal diameter to that of the tangential port) performed the best however limitations in testing the smaller diameter axial port (50% of the tangential port diameter) at higher Reynolds numbers requires inferring from the distribution. It is clear, however, that the third axial port with the largest diameter (150% of the tangential port diameter) performed the worst of the

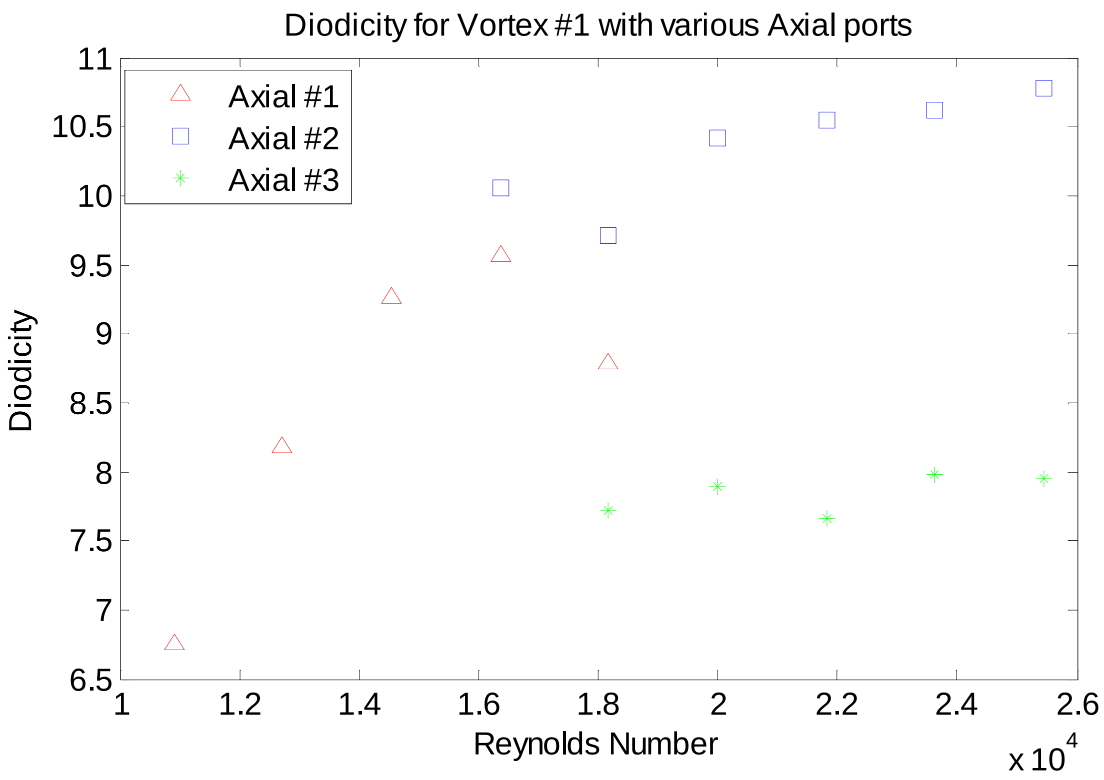

Figure 6.4: Diodicity with respect to Reynolds number for small diode ($\alpha = 6$) with the three axial ports [65].

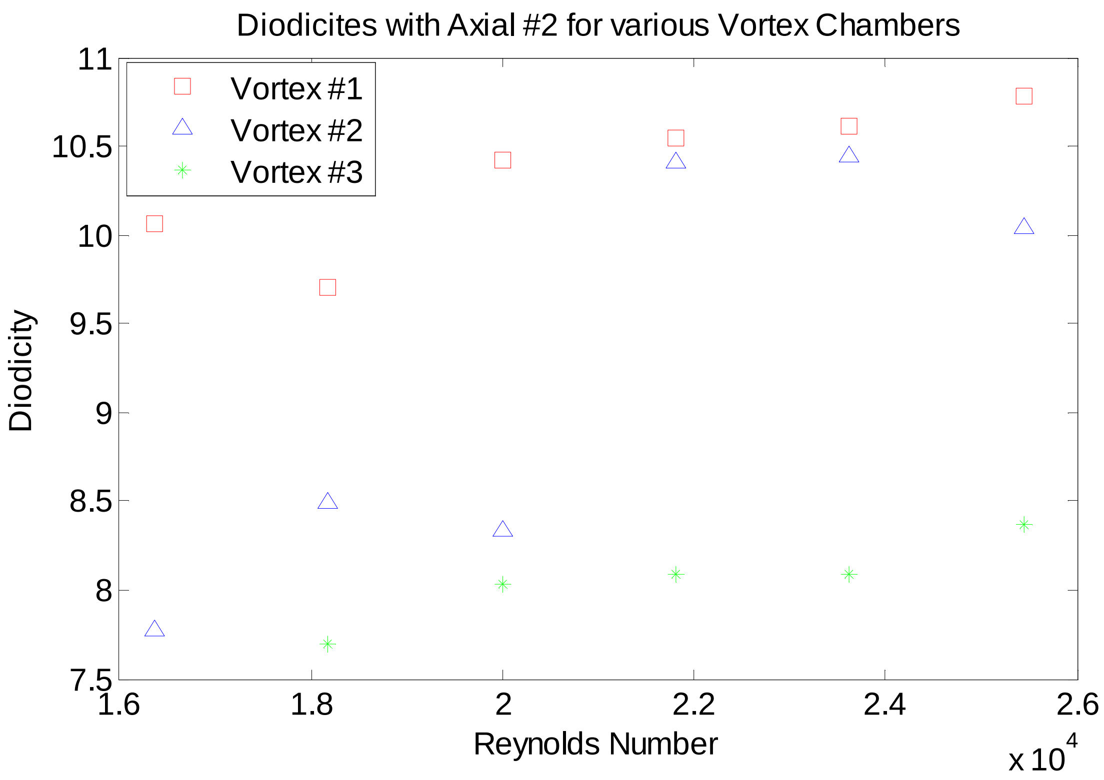

Figure 6.5: Diodicity with respect to Reynolds number for small, medium, and large diodes ($\alpha = 6, 9, 12$) with nominal axial port [65].

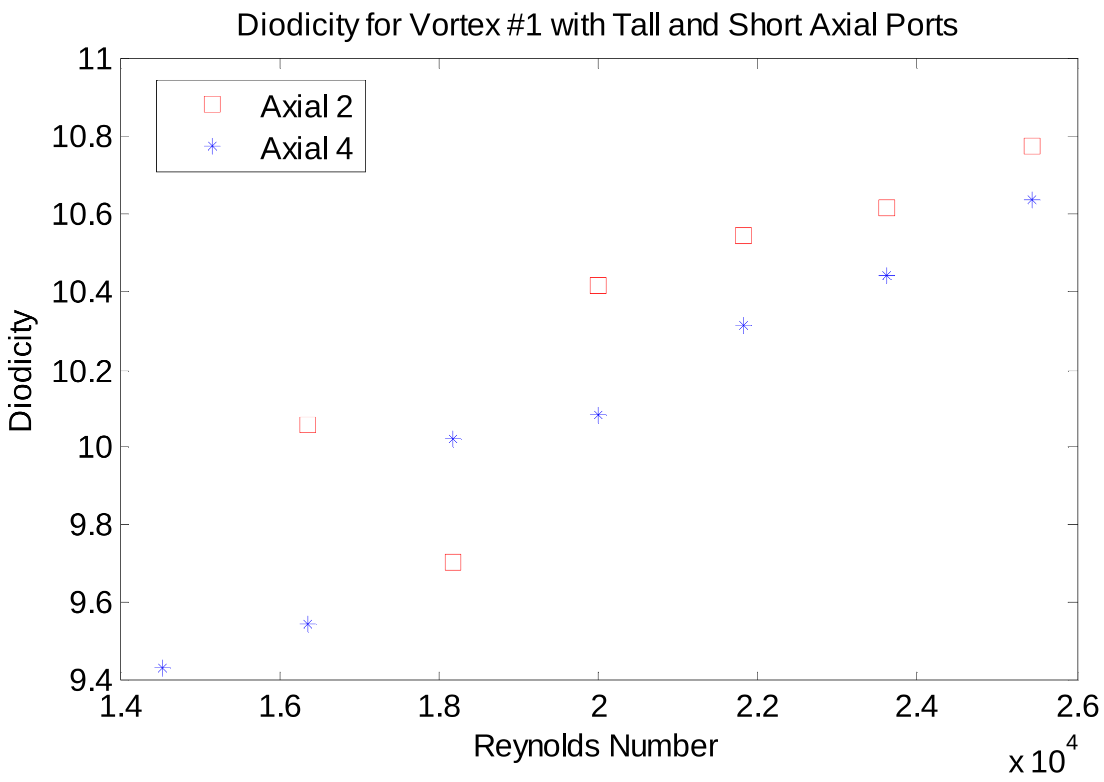

Figure 6.6: Diodicity with respect to Reynolds number for small diode ($\alpha = 6$) with axial ports 2 (tall) and 4 (short) [65].

Figure 6.7: Top view of a fluidic diode under reverse flow operation.

three. The aspect ratio of the diode also appeared to have an impact on the diodicity of the device (Figure 6.5) where the diodicity was highest for the smallest diode ($\alpha = 6$). One possible reason for this is that as the aspect ratio increases, the swirling flow would laminarize prior to setting up a forced vortex in the center of the chamber. Another observation can be made from Figure 6.6 where the taller axial port resulted in higher diodicity values. Physically this seems to be plausible due to the fact that the swirling flow exiting the flow chamber is maintained for a longer distance thus adding to the flow resistance. In the forward direction, the increased height in the axial port contributes a smaller relative amount of flow resistance due to the wall friction.

Chapter 7

Summary

7.1 Overview

Complex engineered systems require understanding phenomenology across wide-ranging spatial and temportal scales. Inductive methods start with the global system response and work towards the local level while deductive methods begin with local physical processes and work upwards towards the system response. The fact that nuclear power plants can be described within a hierarchical architecture where each level can be characterized by three unique metrics (i.e. by length, time, and volumetric fraction) makes the problem particularly tractable. As noted by Zuber [90], these hierarchical levels reflect the details of information the engineer is seeking. Thus, the observer looks to higher levels for system synergism and significance while the observer looks at lower levels for details and mechanisms. The key point is that both methods yield different insights into the system where the level of observer (in this case, the control volume) provides the "window" into the problem.

The concept of a "risk triplet" serves as a good starting point for better understanding the implications of inductive and deductive methods. One of the key issues surrounding the licensing of advanced reactor technology involves the identification of a complete set of design basis events over a reasonable frequency space. Perhaps the biggest challenge with licensing new nuclear technology is establishing this design basis envelope where there is very limited operational experience. Defense in depth, rooted in redundancy and diversity principles, will play an important role in reducing completeness uncertainty. However, the process by which the regulatory body would deem acceptability is very uncertain. Assessing the likelihood of initiating event occurance involves phenomenology that evolves over significant temporal and spatial scales making predictive simulation a challenging task. The methods presented in this dissertation focus on developing similarity criteria for validation experiments in order to better understand the consequence space. Phenomenology in the consequence space typically occurs over much shorter temporal scales and a smaller range of spatial scales. A summary of results from each effort at the global, subsystem, and component level are presented in the following sections.

7.2 Global Scaling Summary

Physical similarity criteria with respect to dynamic component interaction for a prototypical 16 MWth ATR during a LOFC was developed based on the full scale 900 MWth PB-AHTR concept. Both fractional scaling and causative process related scaling methods were utilized. The scaling groups from the causative process scaling analysis show the relative global importance of the inertial and impedance term with respect to the driving gravitational force while results from the fractional scaling analysis show the relative global importance of the gravitational and impedance terms with respect to the time-dependent inertial term. During the early stages of the LOFC, the primary systems is not initially balanced with the overall flow resistance in the loop due to change in flow direction. Additionally, fractional scaling revealed that fluid inertia effects are small and the system will adjust very quickly to any changes in the loops flow resistance. The resultant scaling groups can be used to design a model IET capable of capturing the dominant phenomena during the PB-AHTR LOFC transient while providing a quantitative means of assessing scale distortion from the model to the prototype. Additional integral scaling analyses, such as the global energy balance between heated structures and the working fluid in the primary loop, will need to be developed in order to ensure the model physical similitude with the prototype.

7.3 Subsystem Scaling Summary

The concept of a buoyantly-driven shutdown rod holds great promise for controlling reactivity in the PB-AHTR during anticipated transient without scram, including the case of LOHS where the primary pumps continue running even though heat removal from the IHXs stops.. The PRISM experiment was used successfully to run a scaled integral effects test of the PB-AHTR shutdown rod response under prototypical conditions. Using the appropriate length and time scales for prototypical conditions, the PB-AHTR shutdown rods would have inserted far enough to provide adequate reactivity control for a safe shutdown after approximately 40 seconds (assuming the same rod geometry and density history). The pre-predicted dynamic response of the rod was in close agreement with experimental results. Preliminary system code simulations have indicated this dynamic response of the rod during LOHS conditions could provide effective reactivity control under LOHS and warrants further investigation. In order to improve the fidelity of the rod dynamic response model, the coupling effects of the neutronics and channel thermal response need to be analyzed. Additionally, the overall reliability of the system will need to be determined and compared with commensurate Gen IV reactivity control systems.

7.4 Component Scaling Summary

Similarity criteria and results from a fluidic diode reduced-scale experiment were presented. An empirical approach was used to determine design optimization. Despite preliminary diodicity values being lower than expected, the experimental approach warrants further investigation where a wider range of Reynolds numbers can be examined. Additionally, a systematic approach to identifying experimental uncertainties should be performed where discrepancies with results from the published literature can be further investigated. The simplicity in fabrication methods as well as the use of a simulant fluid makes further investigation particularly tractable. A modest investment in improved pressure and flowrate measurement equipment should also greatly improve experimental accuracy.

Bibliography

[1] R. Rajeev A. A. Kulkarni, V. V. Ranade and S. B. Koganti. Cfd simulations of flow in vortex diodes. *AIChE*, 54:1139, 2008.

[2] R. Rajeev A. A. Kulkarni, V. V. Ranade and S. B. Koganti. Pressure drop across vortex diodes: Experiments and design guidelines. *Chemical Engineering Science*, 64:1285 – 1292, 2009.

[3] R. L. Ackoff. From data to wisdom. *Journal of Applies Systems Analysis*, 16:3–9, 1989.

[4] G. A. Apostolakis. A comment on model uncertainty. In *Model Uncertainty: Its Characterization and Quantification*, 1995.

[5] G. A. Apostolakis. Apostolakis on pra. Nuclear News, March 2000.

[6] C. L. Atwood. Correct bayesian and frequentist intervals are similar. *Nuclear Engineering and Design*, 93:145–151, 1986.

[7] P. M. Bardet and P. F. Peterson. Options for a scaled experiments for high temperature liquid salt and helium fluid mechanics and convective heat transfer. *Nuclear Technology*, 163:344–357, 2008.

[8] G. I. Barenblatt. *Scaling, Self-similarity and Intermediate Asymptotics.* Cambridge University Press, 1996.

[9] G. I. Barenblatt. *Scaling.* Cambridge University Press, 2003.

[10] G. I. Barenblatt and Ya. B. Zel'dovich. Intermediate asymptotics in mathematical physics. *Russian Mathematical Survey*, 26:45, 1971.

[11] G.R. Odette B.D. Wirth and R.E. Stoller. Recent progress toward an integrated multiscale-multiphysics model of reactor pressure vessel embrittlement. In *MRS Soc. Symp. Proc 677*, 2001.

[12] T. Bedford and R. Cooke. *Probabilistic Risk Analysis - Foundations and Methods.* Cambridge University Press, 2001.

[13] G. Berthoud. Vapor explosions. *Annual Review of Fluid Mechanics*, 32:573–611, 2000.

[14] E. D. Blandford and P. F. Peterson. A novel buoyantly-driven shutdown rod design for passive reactivity control of the pb-ahtr. In *4th International Topical Meeting on High Temperature Reactor Technology (HTR-2008)*, Washington, D.C., 2008.

[15] L. Burgazzi. Evaluation of uncertainties related to passive system performance. *Nuclear Engineering and Design*, 230:93–106, 2004.

[16] Nuclear Regulatory Commission. Framework for development of a risk-informed, performance based alternative to 10cfr part 5. Technical Report NUREG-1860, Nuclear Regulatory Commission, Washington D.C., 2006.

[17] U.S. DOE NUCLEAR ENERGY RESEARCH ADVISORY COMMITTEE and THE GENERATION IV INTERNATIONAL FORUM. A technology roadmap for generation iv nuclear energy systems. Technical Report GIF002-00, Department of Energy, December 2002.

[18] M. L. Corradini. Vapor explosions: A review of experiments for accident analysis. *Nuclear Safety*, 32:337–62, 1991.

[19] National Research Council. *Understanding Risk: Informing Decisions in a Democratic Society*. National Academy Press, 1996.

[20] S. Kaplan D. Bley and D. Johnson. The strengths and limitations of psa: where we stand. *Reliability Engineering and System Safety*, 38:3–26, 1992.

[21] R. L. Daugherty and J. B. Franzini. *Fluid Mechanics with Engineer Applications*. McGraw-Hill Books, 1965.

[22] W. J. M. de Kruijf et al. Experimental thermohydraulic stability map of a freon-12 boiling water reactor facility with high exit friction. *Nuclear Engineering and Design*, 229:75–80, 2004.

[23] R. G. Easterling. Measuring the predictive capability of computational models: Principles and methods, issues and illustrations. Technical Report SAND2001-0243, Sandia National Laboratories, Albuquerque, New Mexico, 2001.

[24] B. Efron. Why isn't everyone a bayesian? *The American Statistician*, 40:1–11, 1986.

[25] B. E. Boyack et al. Quantifying reactor safety margins. NUREG CR-5249, US NRC, 1989.

[26] C. W. Forsberg et al. Proposed and existing passive and inherent safety-related structures, systems, and components for alwrs. Technical Report ORNL-6554, ORNL, October 1989.

[27] Eardley et al. Quantification of margin and uncertainty (qmu). Technical Report JSR-04-330, JASON defense science advisory panel and prepared for the Department of Defense and the National Nuclear Security Administration, 2005.

[28] P. Bardet et al. The pebble recirculation experiment (prex) for the ahtr. In *ANS Global Conference*, 2007.

[29] P. F. Peterson et al. Design, analysis and development of the modular pb-ahtr. In *International Congress on Advances in Nuclear Power Plants (ICAPP)*, Anaheim, California, June 2008.

[30] G. A. Apostolakis F. J. Mackay and P. Hezlar. Incorporating reliability analysis into the design of passive cooling systems with an application to a gas-cooled reactor. *Nuclear Engineering and Design*, 238:217–228, 2008.

[31] F. R. Farmer. Reactor safety and siting: a proposed risk criterion. *Nuclear Safety*, 1:539–548, 1967.

[32] K. N. Fleming and F. A. Silady. A risk-informed defense-in-depth framework for existing and advanced reactors. *Reliability Engineering and System Safety*, 78:Issue 3, 2002.

[33] R. E. Gamble. *Decoupling, complexity and importance in the desi and analysis of complex transport systems*. PhD thesis, University of California, Berkeley, 2002.

[34] A. Gelman. A bayesian formulation of exploratory data analysis and goodness-of-fit testing. To appear in the International Statistical Review.

[35] J. Huxley. *Evolutionary Ethics 1893-1943*. Pilot Press, 1947.

[36] N. Zuber I. Catton, W. Wulff and U. S. Rohatgi. Application of fractional scaling analysis to loss of coolant accidents (loca) part 3. component level scaling for peak clad temperature. In *Proc. 11th International Topical Meeting on Nuclear Thermal Hydraulics (NURETH-11)*, Popes' Palace Conference Center, Avignon, France, October 2005.

[37] E. Manon J. Garnier and G. Cubizolles. Local measurement of flow boiling of refrigerant 12 in a vertical tube. *Multiphase Science and Technology*, 13:1–111, 2001.

[38] T. S. Kress J. N. Sorensen, G. E. Apostolakis and D. A. Powers. On the role of defense in depth in risk-informed regulation. In *Proceedings of PSA 99, International Topical Meeting on Probabilistic Safety Assessment*, 1999.

[39] E. T. Jaynes. *Probability Theory - The Logic of Science*. Cambridge University Press, 2003.

[40] S. Johnson. *Emergence*. The Penguin Press, 2001.

[41] J. N. Reyes Jr. and L. Hochreiter. Scaling analysis for the osu ap600 test facility (apex). *Nuclear Engineering and Design*, 186:53–109, 1998.

[42] S. Kaplan. Will the real probability please stand up? *Reliability Engineering and System Safety*, 23:285–192, 1988.

[43] S. Kaplan. The words of risk analysis. *Risk Analysis*, 17:407–417, 1997.

[44] S. Kaplan and B. J. Garrick. On the quantitative definition of risk. *Risk Analysis*, 1:11–27, 1981.

[45] J. Katz and A. Plotkin. *Low Speed Aerodynamics*. McGraw-Hill, New York, New York, 2nd edition, 1991.

[46] W. Keller and Mohammad Modarres. A historical overview of probabilistic risk analysis development and its use in the nuclear power industry: a tribute to the late profesor norman carl rasmussen. *Reliability Engineering and System Safety*, 89:271–285, 2005.

[47] S. T. Kline. *Similitude and Approximation Theory*. Springer, 1986.

[48] S. Levy. *TwoPhase Flow in Complex Systems*. John Wiley & Sons, 1999.

[49] G. E. Aposolakis M. J. Delaney and M. J. Driscoll. Risk-informed design guidance for future reactor systems. *Nuclear Engineering and Design*, 235:1537–1556, 2005.

[50] J. R. Skorpik M. S. Greenwood and J. A. Bamberger. On-line sensor for density and viscosity measurement of a liquid or slurry for process control in the food industry. In *Sixth Conference on Food Engineering 1999 AIChE Annual Meeting*, 1999.

[51] L. Meyer and M. Gargallo. Low pressure corium dispersion experiments with simulant fluids in a scaled annular cavity. *Nuclear Technology*, 141:257–274, 2003.

[52] Y. Oono N. Goldenfeld, O. Martin. Intermediate asymptotics and renormalization group theory. *Journal of Scientific Computing*, 1:355, 1989.

[53] U. S. Rohatgi N. Zuber, I. Catton and W. Wulff. Application of fractional scaling analysis (fsa) to loss of coolant accidents (loca): Part 1 methodology development. In *Proc. 11th International Topical Meeting on Nuclear Thermal Hydraulics (NURETH-11)*, 2005.

[54] J. Norton. Nature is the realisation of the simplest conceivable mathematical ideas: Einstein and the canon of mathematical simplicity. *Studies in History and Philosophy of Modern Physics*, 31B:135–170, 2000.

[55] W. L. Oberkampf and T. G. Trucano. Verification and validation benchmarks. *Nuclear Engineering and Design*, 238:716–743, 2008.

[56] Interntional Council on Systems Engineering. Systems engineering handbook - a guide for system life cycle processes & activities. Technical Report INCOSE-TP-2003-002-03.1, INCOSE, August 2007.

[57] G. W. Parry. The characterization of uncertainty in probabilistic risk assessments of complex systems. *Reliability Engineering and System Safety*, 54:119–126, 1996.

[58] PBMR. Design certification: Defense-in-depth approach for the pebble bed modular reactor. Technical Report Document Number 043593, PBMR, 2006.

[59] PBMR. Design certification: Probabilistic risk assessment approach for the pebble bed modular reactor. Technical Report Document Number 039144, PBMR, 2006.

[60] G. Polya. *Induction and Analogy in Mathematics.* Mathematics and Plausible Reasoning. Princeton University Press, 1973.

[61] M. A. Pope and V. A. Mousseau. Accuracy and efficiency of a coupled neutronics and thermal hydraulics model. *Nuclear Engineering and Technology*, 41:885–892, 2009.

[62] K. Popper. *Logik der Forschung (English Edition).* Springer, 1959.

[63] R. Powell. Strategic threats and probabilistic risk analysis. UC Berkeley Travers Department of Political Science White Paper, September 2008.

[64] L. Prandtl. On the motion of fluids with very little friction. *English trans. in Early Developments of Modern Aerodynamics*, 1:484, 1905.

[65] D. Caso R. Burnett and J. Tang. Fluidic diode development and optimization. Technical Report UCBTH-10-004, UC Berkeley Thermal-Hydraulics Laboratory, May 2010.

[66] R. B. Leighton R. P. Feynman and M. Sands. *The Feynman Lectures on Physics Volume II.* Addison-Wesley, 1964.

[67] D. W. Ramey. An inexpensive computer-controlled photogate. *The Physics Teacher*, 43:1–12, 2005.

[68] Y. Y. Haimes S. Kaplan and B. J. Garrick. Fitting hierarchical holographic modeling (hhm) into the theory of scenario structuring and a refinement to the quantitative definition of risk. *Risk Analysis*, 21:807–819, 2001.

[69] L. I. Sedov. The propagation of strong blast waves. *Prikl. Mat. Mekh. Akad. Nauk SSSR*, 10:2, 1946.

[70] D. J. Shlien. Inexpensive method of generation of a good quality laser light sheet for flow visualization. *Experiments in Fluids*, 5:356–358, 1987.

[71] J. W. Stairmand. Flow patterns in vorte chambers for nuclear duties. *Nuclear Energy*, 29:413–418, 1990.

[72] C. Starr. Societal benefit versus technological risk. *Science*, 19:1232–8, 1969.

[73] N. P. Suh. *The principles of design*. Oxford University Press, 1990.

[74] N. P. Suh. *Axiomatic Design: Advances and Applications*. Oxford University Press, 2001.

[75] T. Igusa W. L. Oberkampf T. G. Trucano, L. P. Swiler and M. Pilch. Calibration, validation, and sensitivity analysis - whats what. *Reliability Engineering and System Safety*, 91:1331–1357, 2006.

[76] G. I. Taylor. The formation of a blast wave by a very intense explosion. *Proc. Roy. Soc. A*, 201:159–186, 1950.

[77] N. Tesla. Valvular conduit, 1920.

[78] The Economic Modeling Working Group Of the Generation IV International Forum. Cost estimating guidelines for generation iv nuclear energy systems. Technical Report GIF/EMWG/2007/004, Department of Energy, September 2007.

[79] T. G. Trucano W. L. Oberkampf and C. Hirsch. Verification, validation, and predictive capability in computational engineering and physics. In *Foundations for Verification and Validation in the 21st Century Workshop*, 2002.

[80] U. Rohatgi W. Wulff, N. Zuber and I. Catton. Application of fractional scaling methodology (fsm) to loss of coolant accidents (loca), part 2. system level scaling for system depressurization. In *Proc. 11th International Topical Meeting on Nuclear Thermal-Hydraulic (NURETH-11)*, Popes' Palace Conference Center, Avignon, France, October 2005.

[81] W. Weaver. Science and complexity. *American Scientist*, 36:536, 1948.

[82] G. E. Wilson and B. E. Boyack. The role of the pirt process in experiments, code development and code applications associated with reactor safety analysis. *Nuclear Engineering and Design*, 186:23–37, 1998.

[83] D. N. Wormley. An analytical model for incompressible flow in short vortex chambers. *Journal of Basic Engineering*, 264:369–376, 1969.

[84] William A. Wulf. *Great Achievements and Grand Challenges*, volume 30. National Academy of Engineering, Fall/Winter 2000.

[85] W. Wulff. Scaling of thermohydraulic systems. *Nuclear Engineering and Design*, 163:359–395, 1996.

[86] W. Wulff. *Integral Methods for Two-Phase Flow in Hydraulic Sysytems - in Advances in Heat Transfer*. Academic Press, 1997.

[87] W. Wulff and U. Rohatgi. System scaling for the westinghouse ap600 pressurized water reactor and related test facilities. Technical Report NUREG/CR-5541, US NRC Report, prepared by Brookhaven National Lab, Upton, NY, 1998.

[88] W. Yao and C. Morel. Volumetric interfacial area prediction in upwards bubbly two-phase flow. *International Journal of Heat Mass Transfer*, 47:307–328, 2004.

[89] R. Zobel. Experiments on a hydraulic reversin elbow. *Mitt Hydr Inst Munich*, 8:1–47, 1936. UKAEA Risley Translation, No. 439.

[90] N. Zuber. A hierarchical, two-tiered scaling analysis, an integrated structure and scaling methodology for severe accident technical issue resolution. NUREG: Appendix D, US NRC, Washington DC 20555, November 1991.

[91] N. Zuber. The effects of complexity, of simplicity and of scaling in thermal-hydraulics. *Nuclear Engineering and Design*, 204:1–27, 2001.

Appendix A

Additional System Scaling Discussion

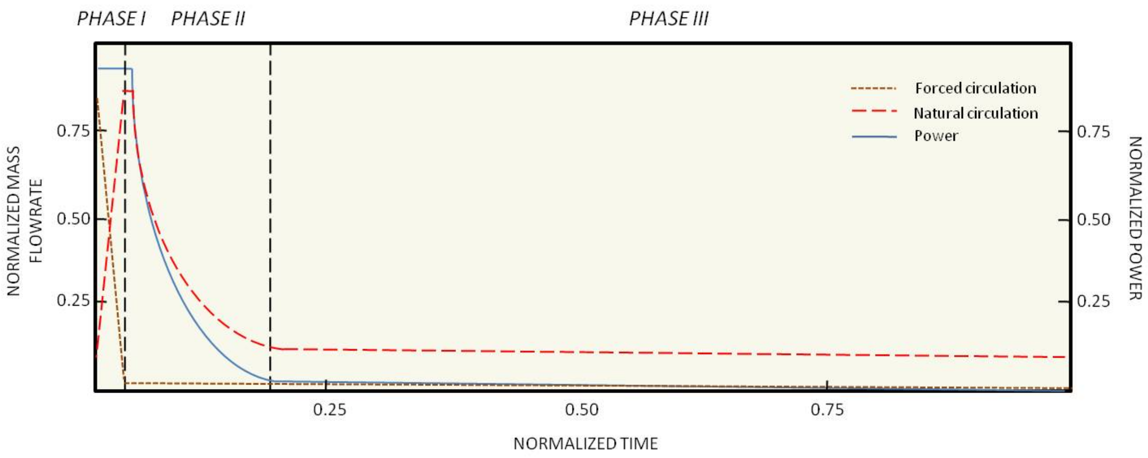

Figure A.1: PB-AHTR LOFC scenario illustrating transition from forced to natural circulation.

A.1 Detailed Scenario Description

Forced circulation in the AHTR is driven by two vertical-shaft, single-stage centrifugal pumps located adjacent to the core exit. The AHTR pump design requirements are derived from the pump technology used for the Molten Salt Breeder Reactor (MSBR) developed at ORNL [16]. Simultaneous pump trips with no active shutdown cooling are within the AHTR design basis envelope and subsequently classified as a design basis event. It is assumed that the shutdown rod drive elements respond actively and the primary loop enters into a flow coastdown mode where decay heat start to be removed passively through the DHX system. The continued operation of one pump presents an interesting problem however will not be discussed in this paper. The LOFC transient can be decomposed into the following three phases which are depicted below in Fig. A.1: (1) pump coastdown phase, (2) quasi-steady natural circulation phase, and (3) steady-state natural circulation phase. The time axis (horizontal) has been normalized with respect to the total time it takes for the core inlet temperature to reach the steady-state value following the pump trip (approximately 20 minutes). The vertical axes have been normalized with respect to the steady-state primary loop mass flowrate and power as well as the maximum flowrate through the DHX system following the reactor scram.

A.1.1 Pump coastdown phase

The transient is initiated by an unexpected pump trip triggering a reactor scram signal to the AHTR reactor protection system prompting the shutdown rods to actively insert. During steady-state operation, the torque acting on the pump due to friction and fluid forces are balanced by the torque from the pump drive motor. Following the trip, the interaction between the pump and the primary fluid is a function of the relative inertias and friction losses where either the remaining rotational kinetic energy of the pump drives the flow or the fluid kinetic energy drives the pump. As the mass flowrate circulating around the forced circulation flow path decelerates, the driving head from the DRACS redirects the flow towards the natural circulation flow path. The performance of the buoyantly-driven shutdown rod system during a LOFC transient without scram increases greatly with a more rapid flow reversal between the two loops (i.e. larger acceleration force on the rod). It is desirable that forced circulation stop rapidly, and thus the AHTR primary pumps do not have flywheels. It is expected that this phase will represent a very short period of time on the order of a few seconds at most.

A.1.2 Quasi-steady natural circulation phase

The beginning of the second phase is defined as the point in time when the mass flowrate in the DHX loop reverses direction and heat is directly removed from the core to the DHX via natural circulation. During this period of time, the power in the core is decaying exponentially following the insertion of the shutdown rods in a similar profile as the ANS reference decay heat curve. For the purpose of this paper, the exact shape of the curve is of second-order importance. The mass flow rate circulating in the primary system drops with the power and eventually reaches steady-state power level of approximately 2% of full power. It is expected that this phase will take, conservatively, on the order of one hour to drop from 7% power to 2% power.

A.1.3 Steady-state natural circulation phase

In the final phase of the LOFC transient, the power level has dropped from 900 MWth to approximately 18 MWth which must be removed from the core. The power level continues to drop at a much smaller rate in this phase and heat removal through the DHX and DRACS system is operating under steady-state conditions. Due to such a gradual decay in heat generation following the initial scram, it is expected that an IET such as CIET should just be capable of simulating this final phase of the transient especially when assessing the performance of the decay heat removal system. Throughout this paper, an emphasis is placed on the steady-state case however scaling arguments are developed in some instances for the transient case.

A.2 System Admittance and Inertia Matrix Development

In this section, the inertia matrix for the PB-AHTR primary system is derived using fundamental linear algebra methods as discussed in Zuber et al. [53]. We will also utilize the nomenclature discussed in the aforementioned work. For a more comprehensive review of the methodology employed, the reader is highly encouraged to review the following work by Wulff [87, 86]. The definition of the global system $N_L \times N_L$ square inertia matrix is defined as,

$$I_{ip} = \Lambda_{ip} - X_{iu}\left(A_r^{-1}\right)_{ut}(B_r)_{ip} \qquad i = 1, ..., N_L \tag{A.1}$$

where Einstein summation convention is used. The first term on the RHS of the equation represents the inertia of the primary loop segments for each phase whereas the second term represents the flow inertia contributions from the secondary flow segments.

The first step in developing the inertia matrix is first creating a system admittance matrix, H, for both the two-loop and three-loop system. Using continuity, the volumetric flow rates at each branch are used to determine the branch exit flow rates. The coefficients for each term make up each individual member of the overall system admittance matrix and are expressed in terms of -1, 0, and 1 (for flow approaching the branch, flow through segment not associated with branch and flow leaving the branch respectively). The matrix consists of N_B rows and $N_L \times N_{L-1}$ columns.

$$H_{pq} = (AB)_{pq} \tag{A.2}$$

The overall system admittance matrices for both phases of the 3-loop systems are given below. It should be noted that the first three columns in matrix $H_{pq,a}$ and $H_{pq,b}$ represent the contributions from the secondary flow segments while the remaining columns represent the contributions from the primary flow segments.

$$H_{pq,a} = \begin{bmatrix} 1 & 0 & 0 & 1 & 0 & -1 \\ 0 & 1 & 0 & -1 & 1 & 0 \\ 0 & -1 & 1 & 0 & -1 & 0 \\ -1 & 0 & -1 & 0 & 0 & 1 \end{bmatrix} \tag{A.3}$$

$$H_{pq,b} = \begin{bmatrix} 0 & 1 & 0 & 1 & 0 & -1 \\ 1 & 0 & 0 & -1 & 1 & 0 \\ -1 & 0 & 1 & 0 & -1 & 0 \\ 0 & -1 & -1 & 0 & 0 & 1 \end{bmatrix} \tag{A.4}$$

The next step is to augment the admittance matrix with the corresponding $N_B \times N_B$ identify matrix yielding the augmented admittance matrix, (H_A):

$$(H_A)_{pq} = (ABI)_{pq} \tag{A.5}$$

Continuing with the process, elementary row reductions are performed on augmented admittance matrix to yield the row-reduced echelon matrix. The fundamental block structure of the row-reduced echelon matrix can then be written in the following form after a little manipulation with MATLAB where the first term in the matrix is the I_r identity matrix.

$$(H_{re}) \sim \left[I_r \left(A_r^{-1}B_r\right) A_r^{-1}\right] \tag{A.6}$$

$$H_{re,a} = \begin{bmatrix} 1 & 0 & 0 & 1 & 0 & -1 & -1 & -1 & -1 \\ 0 & 1 & 0 & -1 & 1 & 0 & 1 & 0 & 0 \\ 0 & 0 & 1 & -1 & 0 & 0 & 1 & 1 & 0 \end{bmatrix} \tag{A.7}$$

.

$$H_{re,b} = \begin{bmatrix} 1 & 0 & 0 & -1 & 0 & 0 & 1 & 0 & 0 \\ 0 & 1 & 0 & 1 & 0 & -1 & -1 & -1 & -1 \\ 0 & 0 & 1 & -1 & 0 & 0 & 1 & 1 & 0 \end{bmatrix} \tag{A.8}$$

In order to construct the final global inertia matrix, the $(N_B - 1) \times N_L$ reduced matrix $(A_r^{-1} B_r)$ and the reduced $(N_B - 1) \times (N_B - 1)$ square matrix A_r^{-1}which are to right of the identity matrix need to be determined. Since the PB-AHTR only operates in single phase throughout the design basis envelope, the dilation vector characterizing the net dilation rate of the flow due to thermal expansion or contraction of the two-phase working fluid is not included. The final global inertia matrix for both phases can now be determined using Equation A.1.

$$\begin{aligned} I_{ip} = \Lambda_{ip} - X_{iu} \left(A_r^{-1}\right)_{ut} (B_r)_{ip} &= \begin{bmatrix} I_1 & 0 & I_5 \\ I_1 & I_3 & I_5 \\ I_1 & 0 & I_5 \end{bmatrix} - \begin{bmatrix} 0 & I_4 & I_6 \\ 0 & 0 & I_6 \\ I_2 & I_4 & 0 \end{bmatrix} \times \begin{bmatrix} 1 & 0 & -1 \\ -1 & 1 & 0 \\ -1 & 0 & 0 \end{bmatrix} \\ &= \begin{bmatrix} I_1 + I_4 + I_6 & -I_4 & I_5 \\ I_1 + I_6 & I_3 & I_5 \\ I_1 - I_2 + I_4 & -I_4 & I_5 + I_2 \end{bmatrix} \end{aligned} \tag{A.9}$$

$$\begin{aligned} I_{ip} = \Lambda_{ip} - X_{iu} \left(A_r^{-1}\right)_{ut} (B_r)_{ip} &= \begin{bmatrix} I_1 & 0 & 0 \\ I_1 & I_3 & I_2 \\ I_1 & 0 & I_2 \end{bmatrix} - \begin{bmatrix} I_4 & I_5 & I_6 \\ 0 & 0 & I_6 \\ I_4 & 0 & I_6 \end{bmatrix} \times \begin{bmatrix} -1 & 0 & 0 \\ 1 & 0 & -1 \\ -1 & 0 & 0 \end{bmatrix} \\ &= \begin{bmatrix} I_1 + I_4 - I_5 + I_6 & 0 & I_5 \\ I_1 + I_6 & I_3 & I_2 \\ I_1 + I_4 + I_6 & 0 & I_2 \end{bmatrix} \end{aligned} \tag{A.10}$$

A.3 Reference Parameters

Reference parameters for both phase categories are presented here. Most values are taken from RELAP5-3D transient simulations or are taken directly from design specifications. For each table, values are provided for each phase type indicated by a and b where appropriate. As discussed in Chapter 2, a simulant working fluid (Dowtherm A) will be used in CIET allowing for reduced operating conditions.

Mass flowrate values at each junction point indicated are tabulated below in Table A.2 where direction (i.e. up, down, etc...) is shown by listing the corresponding segment. As

		Average fluid density ($kg \cdot m^{-3}$)			Average fluid temperature (K)		
		Phase a	Phase b		Phase a	Phase b	
Segment	L/A (m^{-1})	I	II	III	I	II	III
CO	21.5	1939.5	1937.7	1868.2	970.2	973.7	1116.6
PD	28.4	1939.6	1939.2	1872.3	970.1	971.3	1095.8
CR	170.6	1987.0	1962.3	1933.2	872.9	910.4	978.9
LS	3.7	1987.1	1986.1	1949.7	872.9	875.0	950.2
CORE	74.0	1959.9	1914.1	1913.5	928.5	1017.3	1023.4
TS	21.2	1939.5	1923.6	1873.4	975.7	1031.5	1106.6
RS	16.2	1987.7	1986.6	1857.8	871.4	873.8	1100.6
DHX	4.1	1987.4	1986.8	1920.3	872.0	873.4	1009.5
DR	79.6	1987.6	1986.7	1948.8	872.9	873.6	951.1

Table A.1: Numerical values of segment length over area ratios, mixture density values and average fluid temperatures at the start of each phase of the LOFC.

Phase a Mass Flowrates (kg/s)							
Junction A	Flowrate	Junction B	Flowrate	Junction C	Flowrate	Junction D	Flowrate
W_{LS}	1055.9	W_{CS}	1043.7	W_{TS}	1055.9	$W_{CO+PD+CR}$	1067.6
$W_{DR+DS+RS}$	11.7	W_{SR}	12.2	W_{CS}	1043.7	W_{TS}	1055.9
$W_{CO+PD+CR}$	1067.6	W_{LS}	1055.9	W_{SR}	12.2	$W_{RS+DS+DR}$	11.7
Phase b Mass Flowrates (kg/s)							
W_{LS}	152.4	W_{CS}	140.3	W_{TS}	152.4	$W_{CO+PD+CR}$	3.5
$W_{DR+DS+RS}$	11.7	W_{SR}	12.1	W_{CS}	140.3	W_{TS}	152.4
$W_{CO+PD+CR}$	1.3	W_{LS}	152.4	W_{SR}	12.1	$W_{RS+DS+DR}$	161.0

Table A.2: Mass flowrate values at each juntion point by phase.

mentioned, primary mass flowrates are indicated by red arrows and secondary flowrates are indicated by black arrows. These values are used to populate the primary mass flow rate vector (Equations 4.6 and 4.7) and the directed kinetic energy vector (Equations 4.15 and 4.16).

Loop Residence Time (s)		
Loop	Phase a	Phase$b$
PCL	43.2	499.2
SRL	56.3	262.4
DBL	23.9	499.2

Table A.3: Loop residence time by phase during LOFC.

Additional Reference Parameters	
Isobaric thermal expansivity, β, (K^{-1})	2.14E-4
Temperature difference, ΔT_{GR}, (K)	100
Driving head length, ΔH_{GR}, (m)	3.6

Table A.4: Additional reference parameters for LOFC scaling analysis.

	Flow leaving from $(kg \cdot m^{-4})$		
Loop	Junction A	Junction B	Junction D
PCL	1.93E+5	-1.45E+5	4.36E+5
SRL	4.84E+4	2.35E+5	4.36E+5
DBL	-4.61E+4	-1.45E+5	6.34E+5
	Flow leaving from $(kg \cdot m^{-4})$		
Loop	Junction A	Junction B	Junction D
PCL	-2.42E+5	0	2.38E+5
SRL	4.80E+4	2.30E+5	1.98E+5
DBL	1.89E+5	0	1.98E+5

Table A.5: Numerical values of inertia matrices for both Phases a and b where the primary mass flowrates are shown in Figure 4.1 by red arrows.

Appendix B

Additional Subsystem Scaling Discussion

B.1 Modeling Dynamic Response of Buoyantly-Driven Shutdown Rod

In this Appendix, a theoretical first-order model is developed for modeling the dynamic response of the shutdown rod concept and compared with experimental results. Using the scaling arguments described in Section 5.4, a reduced-scale experiment was built and multiple runs were performed for experimental validation. A description of the analytical model and PRISM experiment are given in this Appendix.

B.1.1 Forces acting on the rod

The shutdown rod is modeled as an immersed body being subjected to drag and buoyancy forces. Insertion of the shutdown rods occurs due to buoyancy forces generated by the difference between the density of the control element and the reactor coolant. A simple force balance on the shutdown rod yields the following expression:

$$m_r \frac{d\overrightarrow{u_r}}{dt} = F_D - F_B \tag{B.1}$$

The profile drag force F_D acting on the rod is a sum of the pressure drag associated with the pressure difference between the bottom and top surfaces of the rod and the viscous drag, or skin friction, between the fluid and the rod surface. Due to a large rod L/D ratio of 18.3, the contribution of the viscous drag is expected to dominate. One added element of complexity is the wall effects from the confined space through which the rod travels. As the fluid in the channel approaches the rod, it accelerates through the annular passage between the rod and the channel (see Figure B.1).

Both contributions of drag are strong functions of the dynamic pressure of the fluid integrated over the surface area of the rod. Assuming the walls of the rod behave like the wall of a smooth pipe at comparable Reynolds numbers, the friction drag acting on the rod equals the shear stress integrated across the wall surface area projected normal to the vertical axis. Using the Blasius approximation [21] and rearranging terms, the total drag force acting on the rod can be written as,

$$F_D = \frac{1}{2}\rho_f \overrightarrow{u_r}^2 \left[C_D A_{cs} + \frac{0.316}{4 \cdot N_{Re}^{0.25}} \cdot A_s \right] \tag{B.2}$$

$$\overrightarrow{u_r} = \overrightarrow{u_{ch}} \left(\frac{A_{ch}}{A_{ch} - A_r} \right) \tag{B.3}$$

where, C_D, A_{cs}, A_s, and ρ_f are the drag coefficient, cross-sectional area, corrected surface area and fluid density respectively. In equation B.3, continuity is used to determine the local average velocity of the fluid passing the rod where A_{ch} and A_r are the cross-sectional area of the channel and the rod respectively. It should be noted that in the dynamic model,

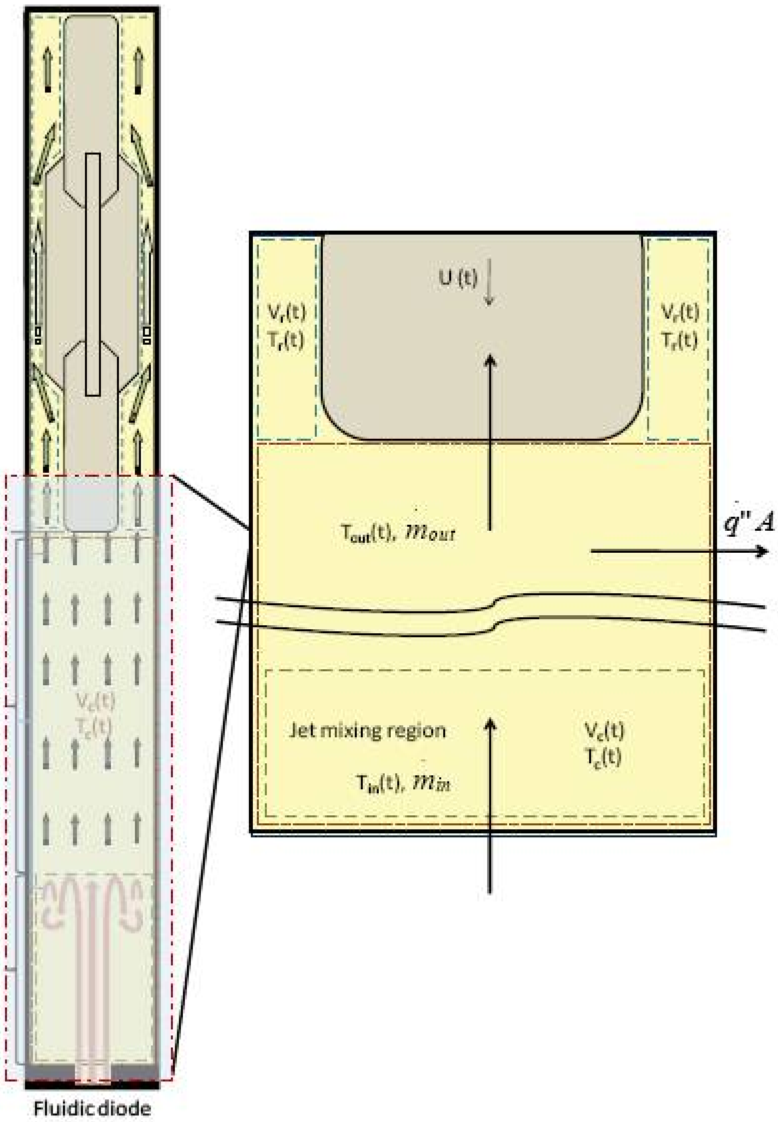

Figure B.1: Schematic (not to scale) of system control volumes and general assumptions

$\overrightarrow{u_r}$ is actually the sum of the approach flow velocity and the downward velocity of the rod. Since the actual AHTR shutdown rod geometry is moderately complex, a simple cylindrical shape of a rod with two streamlined caps was selected for the initial study presented here. Combining equations B.1 and B.2, the momentum balance on the rod can be rewritten as:

$$m_r \frac{d\overrightarrow{u_r}}{dt} = \frac{1}{2}\rho_f \overrightarrow{u_r}^2 \left[C_D A_{cs} + \frac{0.316}{4 \cdot N_{Re}^{0.25}} \cdot A_s \right] - \Delta\rho V_r g \tag{B.4}$$

where $\Delta\rho$ is the density difference between the fluid and the rod. The drag coefficient associated with the pressure drag must be determined experimentally.

B.1.2 First-order Predictive Model

Since the initial key objective of this work is to demonstrate proof-of-principle, the localized thermal-hydraulic modeling of the buoyant jet mixing effects is not considered and will be addressed in future work. Therefore, a simple first-order model was developed to approximate the rod motion as a function of density history. Since the rod inertia term is expected to be small, Equation B.4 can be rewritten based on a balance between buoyancy and drag forces as,

$$\overrightarrow{u_r}(t) = \left(\frac{2 \cdot \Delta\rho(t) V_r g}{\rho_f(t) \left[C_D A_{cs} + \frac{0.316}{4 \cdot N_{Re}^{0.25}} \cdot A_s \right]} \right)^{0.5} \tag{B.5}$$

In validating the code with integral effects test data, the inlet jet density history is measured experimentally and used as a boundary condition at each time step of the simulation. The profile drag coefficient is also measured experimentally where the data is used to determine the appropriate value to use at each time step.

B.2 Passive Rod Insertion Shutdown Model (PRISM) Experiment

B.2.1 Experiment Description

To demonstrate the viability of the passively-driven shutdown rod concept, a proof-of-principle experiment was constructed in the UC Berkeley Nuclear Engineering Thermal Hydraulics Laboratory. Properly scaled experiments maintain geometric, kinematic, and dynamic similarity between the model and the prototype. Demonstration of physically similar phenomena is essential to modeling success. The Passive Rod Insertion Shutdown Model (PRISM) experiment was built using sugar water as a simulant fluid.

In addition to simulating the fluid mechanics, the density change from temperature rise in the primary coolant can be simulated by changing the density, or diluting, sugar water in the loop with dyed pure water over an accelerated time scale. The water loop for the PRISM experiment was assembled using PVC and acrylic piping (Figure B.3). An optics table was used to mount the shutdown rod channel model and provided overall structural support. Flow in the loop was throttled using a simple PVC ball valve and the volumetric flow rate was measured using a rotameter. Using the above length scale, the model volumetric flow rate is 34.5 liters per minute (9.1 gallons per minute), giving an average upward velocity of 0.126 m/s in the test channel, matching the design 0.2 m/s upward flow velocity in the prototypical channel. A simplified cylindrical rod geometry was selected in order to minimize the complexity associated with pre-predicting the drag of the actual PB-AHTR shutdown rod geometry (Figure B.2). The model rod was assembled using PVC piping and two streamlined end caps that were fabricated out of stock PVC material. The rod density was modified by changing the number of washers attached to a threaded rod that also pulled the two end caps into compression. The activation rod that would provide forced insertion was simulated by a stationary rod, which held the rod at its maximum vertical elevation. The rod was held at a location low enough to ensure that the rod was not affected by the cross flow at the top of the channel.

Table B.1 summarizes the shutdown rod and channel dimensions for both the prototype and model. For a submerged cylindrical body to be stable, the body's center of gravity must lie directly below the center of buoyancy. The center of gravity of the rod is located 0.365 m from the bottom tip (center of rod) and 4.5 cm below the center of buoyancy. The center of mass was varied over a range of distances in order to find the optimal position which was determined empirically. The initial position and orientation of the rod is an important factor in ensuring the stability of the rod during the fall. It should be noted that that the channel entrance and exit geometries were also simplified in order to focus on first-order phenomena affecting the rod dynamical response.

B.2.2 Data Acquisition Systems

The two key measurements necessary to validate the first-order model developed are the rod position in the channel and the density of the sugar water entering the channel. By taking rod velocity measurements at different axial locations in the channel, the pre-predicted rod position history can be compared with the experimental results. The

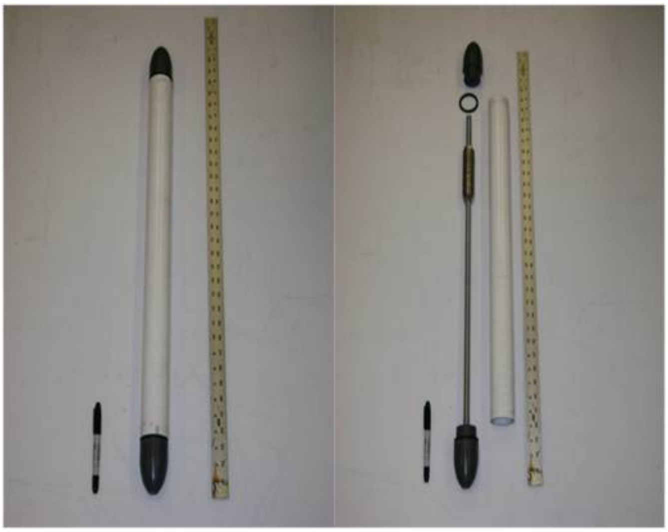

Figure B.2: PRISM model shutdown rod assembled and disassembled (yardstick reference).

Shutdown rod channel dimensions		
Type	PB-AHTR 900 MWth	PRISM
Working fluid	Flibe	Sugar water
Active height (m)	6.2	2.87
Channel diameter (cm)	19.8	9.16
Flow area (m^2)	3.12E-2	6.61E-3
Diameter of jet orifice (cm)	6.26	2.90
Jet-to-channel density ratio	0.97	0.97
Shutdown rod dimensions		
Type	PB-AHTR 900 MWth	PRISM
Effective rod length (m)	3.5	1.62
Effective rod diameter (m)	0.13	4.51E-2
Density of rod material ($g \cdot cm^{-3}$)	1.980	1.023

Table B.1: Shutdown channel and rod dimensions for the PB-AHTR and PRISM.

Figure B.3: PRISM experiment prior to operation.

kinematic motion of the rod was measured using a custom laser sheet photogate system based on work by Ramey [67] and Shlien [70]. A total of four photogate stations were assembled and carefully positioned vertically along the channel. Each station consists of a light source, a photosensor receiver, and appropriate wiring to the computer. A laser sheet is generated by placing a rotating cylindrical lens in front of a 5 mW laser light source. In order to translate interrupted light into an electrical signal, three photosensors were positioned around the perimeter of the surface opposing the light source (see Figure B.4). Each set of photosensors was wired in series in order to ensure the rod would block at least one sensor despite its orientation in the channel. When any of the three photosensors is blocked, the increased resistance in the circuit causes the analog signal into the computer to short to ground. A computer code written in C was used to interpret this signal and record the time that the gate was blocked. By knowing the gate position, rod velocity and acceleration data can be collected. Linux (Fedora v9) was used due to the ease of instituting memory management and priority scheduling. A preliminary accuracy assessment by measuring the time for data collection over several trials indicates system accuracy on the order of 10 µs for the arrival time measurement.

The thermal response of the PB-AHTR shutdown rod channel was simulated by diluting the primary sugar water loop with dyed pure water held in a second tank. In order to measure the density change in the channel as the system was diluted, a simple laser deflection technique was implemented. The index of refraction changes linearly over the considered range of sugar water densities. In order to minimize optical distortion, a rectangular acrylic section was fabricated and inserted into the flow loop 0.71 meters upstream of the shutdown rod channel. A 30-mW helium-neon laser was used as a light source and redirected over 2.1 m to allow for sufficient deflection (for the considered 23 kg/m3 density change, a deflection of 0.31 m was measured). By projecting the light source onto a sheet target, a video camera can be used to measure the time variation of the density. Figure B.5 provides a schematic of the in-situ density measurement setup. By weighing and adding the sugar to the loop in increments, the density of the solution was found to be in agreement with the assumed linear variation of index of refraction.

The transient is initiated by turning the fresh-water bleed flow valve which in turn activates the data acquisition system via a lever switch which is mechanically coupled to the valve. In addition to starting the computer timer for the photogate system, the lever switch activates the laser system for the photogates and an LED in the field of view of the target screen providing a visual cue for the two camera systems. Synchronizing these systems allows for close correlation between the local channel density history and rod position as the transient evolves.

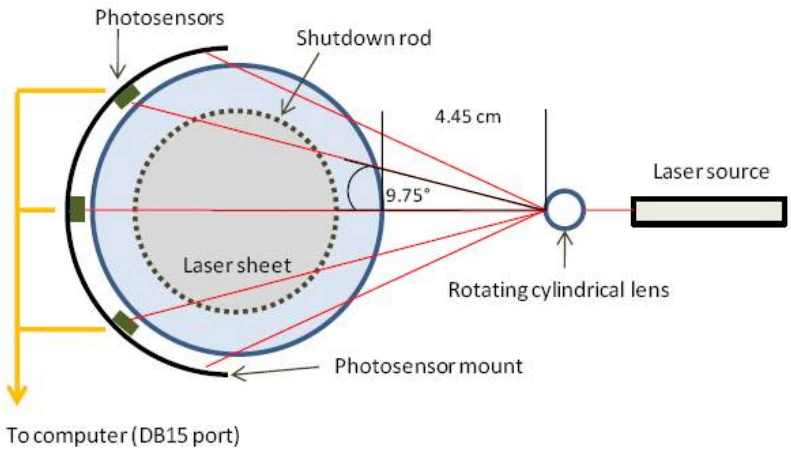

Figure B.4: Schematic of the photogate station used for measuring kinematic motion of shutdown rod (not drawn to scale).

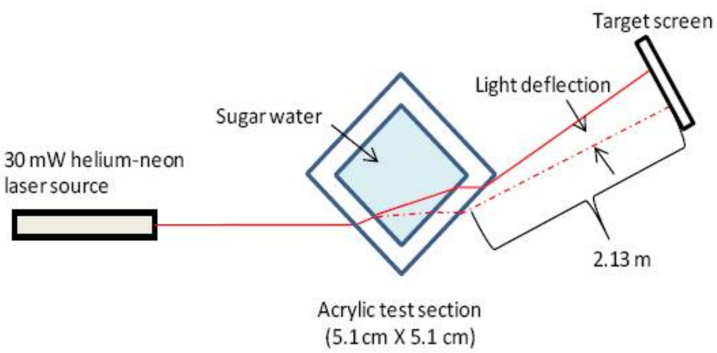

Figure B.5: Schematic of side view of in-situ density measurement setup (not drawn to scale). Flow in the test section is normal to the page.

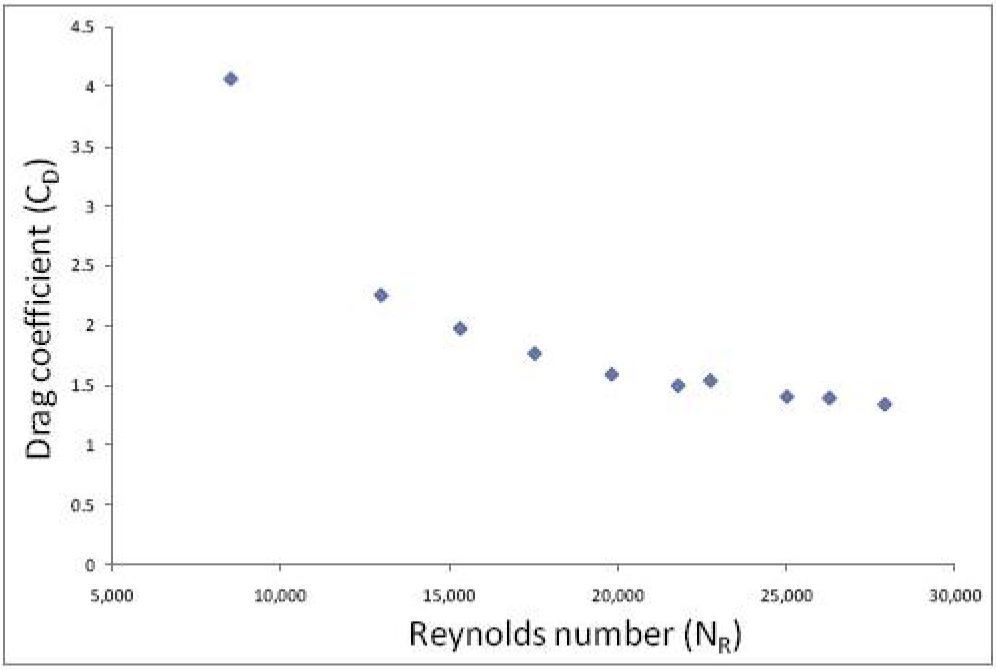

Figure B.6: Measured drag coefficients for the cylindrical rod for counter-flow conditions using local flow conditions.

B.2.3 Shutdown Rod Calibration

In order to calibrate the PRISM experiment, the rod density must be measured. Additionally, the rod drag coefficient as a function of Reynolds number must also be measured in order to validate the rod dynamics model. The shutdown rod is designed to be neutrally buoyant at 615°C under prototypical conditions, which corresponds to a sugar water specific gravity of 1.023. Using a relationship between specific gravity and sugar water concentration (by weight percent) from Greenwood [50], the density of the rod was determined by adding washers to the shutdown rod model until the point of neutral buoyancy was reached.

In order to measure the rod drag coefficient, the terminal velocity of the rod was measured using the photogate system. For the terminal velocity, the acceleration term is zero. Because the buoyancy term depends only on the total density difference between the rod and the surrounding fluid, the buoyancy force (and rod terminal velocity and Reynolds number) was varied by changing the mass of the rod. Measured values for C_D are presented in Figure B.6.

Appendix C

Additional Component Scaling Discussion

C.1 Fluidic Diode Validation Experiment

In order to demonstrate the viability of a fluidic diode in the AHTR, a proof-of-principle experiment was constructed in the UC Berkeley Nuclear Engineering Thermal Hydraulics Laboratory by undergraduate researchers under the guidance of the author. A brief description is given in this section however a more extensive description of the experiment and measurements can be found in [65]. It is important to note that this work is very early in the exploratory phase and is ongoing. As discussed in Chapter 6, scaling at the component level must be performed over a range of boundary conditions that the component will be subjected to. Due to the relative simplicity of the functionality of a fluidic diode, the experimental effort is only concerned with maintaining physical similarity with respect to matching fluid forces acting on it.

C.2 Experiment Description

C.2.1 Vortex Diode Fabrication

Model fluidic diodes were constructed out of ABS plastic using Fused Deposition Modeling (FDM) with varying diameters while the axial ports were made out of PVC plastic and fabricated on a lathe. The purpose of the experimental work was to develop an empirical understanding of the key geometry configurations in order to optimize the diodicity of the fluidic diode. For the purpose of this appendix, only a generic description of the diode is given where detailed information on the geometrical parameters varied can be found in [65].

The vortex chamber was constructed in two pieces and chemically bonded together (Figure C.2). A square piece of ABS plastic was chemically bonded to the top of the diode to increase the amount of material for drilling and tapping a hole for the axial port. One of the unfortunate consequences of using FDM for fabricating the vortex chambers was the material splintering while drilling through it. The FDM fabrication process consists of depositing successive layers of ABS plastic building the part vertically from the bottom up. Therefore, ABS plastic cement was used to smooth out the inner surface and minimize surface roughness. Due to the high pressure in the vortex chamber, a silicone sealant was used around the seam where the two parts were connected and subsequently leak tested.

The axial and tangential ports were fabricated on a lathe out of PVC plastic stock (Figure C.3). The interior of axial port's interior geometry is gradually tapered between the inlet and exit of the port (the smaller diameter is on the side attached to the chamber while the larger diameter is on the side that empties into the tank). The purpose of gradual taper is to diffuse the flow exiting the diode in the reverse direction and to nozzle the flow in the forward direction.The edge of the axial port diameter has been chamfered

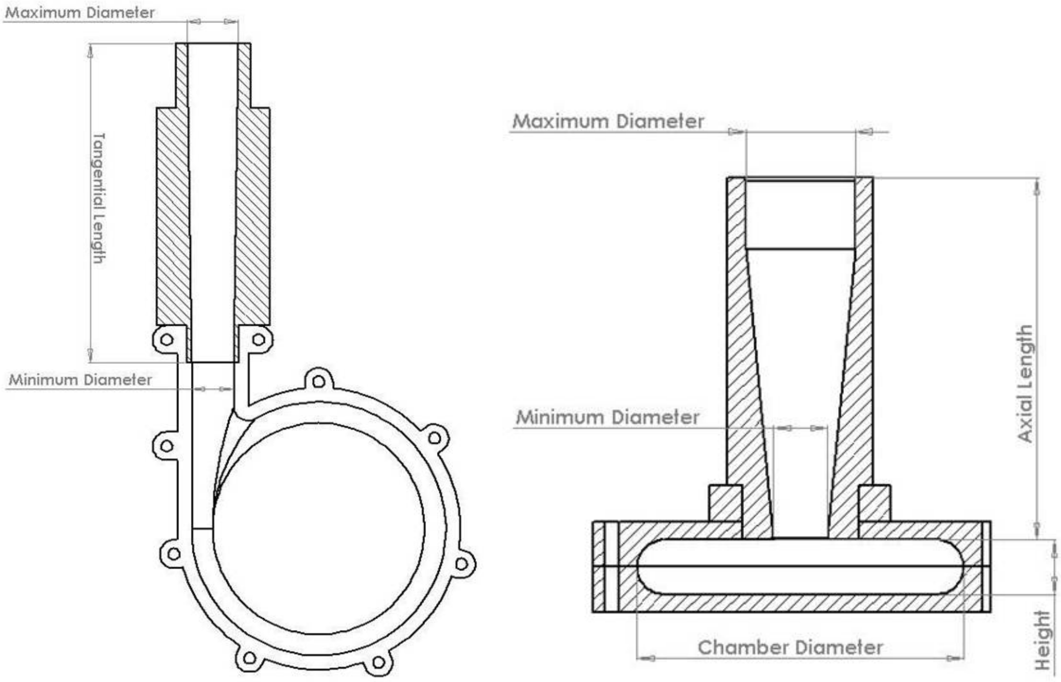

Figure C.1: Schematic of the top and side view of the fluidic diode assembly [65].

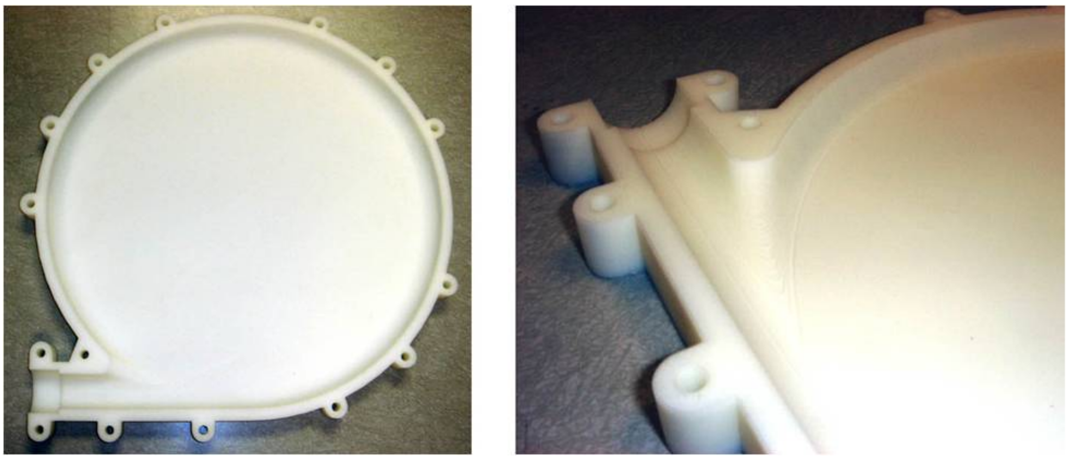

Figure C.2: The two ABS components making up the vortex chamber prior to assembly.

Figure C.3: Axial port comparison for a fixed length where the middle port is the nominal size.

in order to minimize turbulence generation and resultant flow resistance in the forward direction.

C.2.2 System Loop Description

A schematic and picture of the system loop are shown in Figures C.4 and C.5. The fluidic diode was housed inside a plastic tank which was able to accommodate a range of flow conditions in both directions. An acrylic plate was placed at the bottom of the tank to mount each fluidic diode and restrict the torsional motion of the diode in the reverse direction as well as the buoyancy force pushing the diode vertically. Bulkheads and unions were used to allow for installing each of the fluidic diodes in the system loop.

In order to control the flowrate and direction of the flow, ball valves and bypass lines were used where the flow could be throttled. A rotameter was positioned downstream of the throttle valve in order to take reasonable flowrate measurements. When testing each diode in the reverse direction, the system required a nontrivial amount of time to reach equilibrium due to the large volume of the tank. In the reverse direction, flow enters the tangential port and exits the axial port filling the tank until it reaches the upper bulkhead where it then flows out to the drain. To avoid siphoning, drain lines were adjusted to be the same height as the piping coming from the lower bulkhead of the tank.

Direct pressure measurements for both the forward and reverse directions were taken using manometers positioned just before the tangential port inlet and the tank approximately halfway between the upper and lower bulkheads. Since the diodicity is just the ratio of the pressure drops in both directions, relative pressure measurements are satisfactory. Due to practical height restrictions in the lab, a pressure gage replaced the

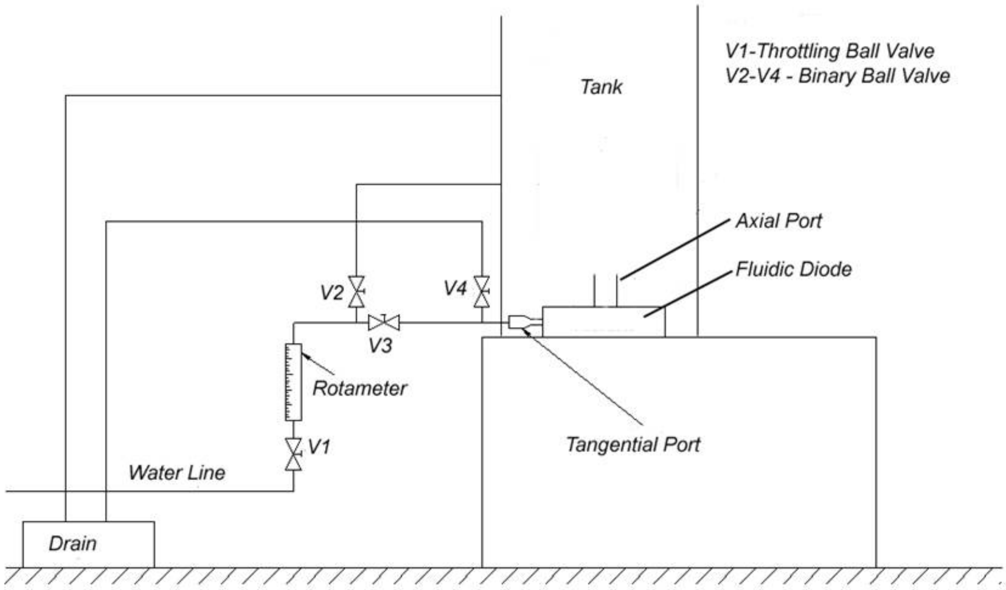

Figure C.4: Loop Schematic for fluidic diode scaled experiment [65].

manometer positioned before the tangential port in order to measure higher pressure readings in the reverse direction (for higher Reynolds numbers). For a more detailed description of the experiment and sources of experimental uncertainty, the reader can refer to [65].

Figure C.5: Experimental loop setup for reverse flow direction prior to operation.